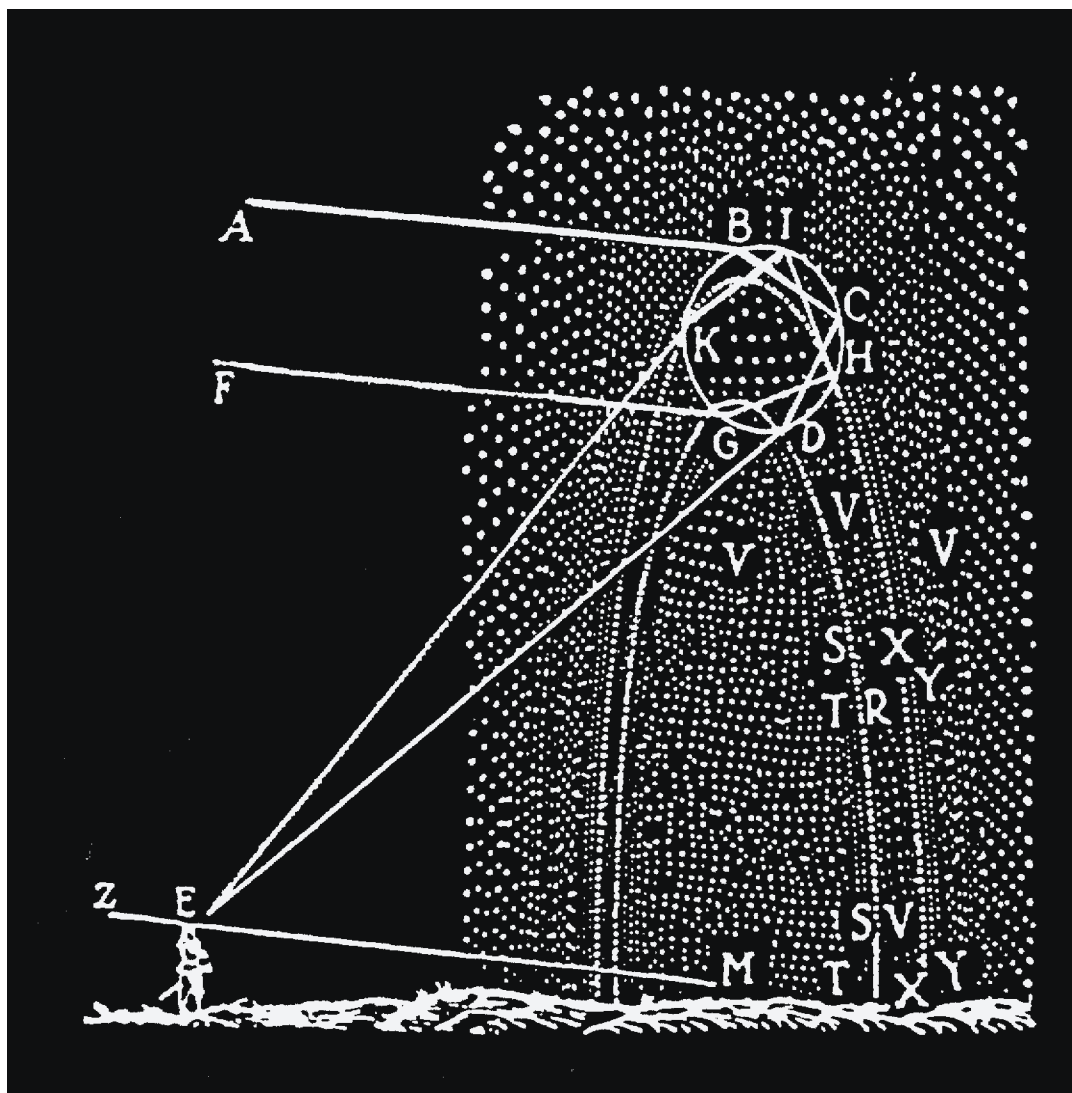


Scattering problems involving electrons, photons, and Dirac fermions



Izak Snyman

Scattering problems involving
electrons, photons,
and Dirac fermions

PROEFSCHRIFT

TER VERKRIJGING VAN
DE GRAAD VAN DOCTOR AAN DE UNIVERSITEIT LEIDEN,
OP GEZAG VAN RECTOR MAGNIFICUS
PROF. MR. P. F. VAN DER HEIJDEN,
VOLGENS BESLUIT VAN HET COLLEGE VOOR PROMOTIES
TE VERDEDIGEN OP DINSDAG 23 SEPTEMBER 2008
TE KLOKKE 13.45 UUR

DOOR

Izak Snyman

GEBOREN TE JOHANNESBURG IN 1980

Promotiecommissie:

Promotores: Prof. dr. C. W. J. Beenakker
Prof. dr. Yu. V. Nazarov (Technische Universiteit Delft)
Referent: Prof. dr. H. T. C. Stoof (Universiteit Utrecht)
Overige leden: Dr. Ya. M. Blanter (Technische Universiteit Delft)
Prof. dr. J. M. van Ruitenbeek
Prof. dr. ir. W. van Saarloos
Dr. J. Tworzydło (Universiteit van Warschau)
Prof. dr. J. Zaanen

Dit werk maakt deel uit van het onderzoekprogramma van het Stichting voor Fundamenteel Onderzoek der Materie (FOM), die financieel wordt gesteund door de Nederlandse Organisatie voor Wetenschappelijk Onderzoek (NWO).

This work is part of the research program of the ‘Stichting voor Fundamenteel Onderzoek der Materie (FOM)’, which is financially supported by the ‘Nederlandse Organisatie voor Wetenschappelijk Onderzoek (NWO)’.

Contents

1	Introduction	1
1.1	Scattering theory of electron transport	2
1.2	The Keldysh technique	5
1.3	Photons	7
1.4	Graphene: Dirac Fermions	11
1.5	Bilayer graphene	17
1.6	This Thesis	19
1.6.1	Chapter 2	19
1.6.2	Chapter 3	20
1.6.3	Chapter 4	21
1.6.4	Chapter 5	21
1.6.5	Chapter 6	21
1.6.6	Chapter 7	22
	Appendix 1.A The Keldysh technique: an example	23
2	The Keldysh action of a time-dependent scatterer	33
2.1	Introduction	33
2.2	Derivation	37
2.2.1	Preliminaries: Definition of the Green function	40
2.2.2	Varying the action	42
2.2.3	Expressing the variation of the action in terms of the Green function	43
2.2.4	Relating g inside the scattering region to g at reser- voirs.	45
2.2.5	Finding the variation of the action in terms of the reservoir Green functions and the scattering matrix	47
2.2.6	Integrating the variation to find the action	48
2.3	Tracing out the Keldysh structure	49

2.4	An example: Full Counting Statistics of transported charge	51
2.5	Tracing out the channel structure	52
2.6	An example: The Fermi Edge Singularity	55
2.7	Conclusion	59
3	Quantum tunneling detection of two-photon and two-electron processes	63
3.1	Introduction	63
3.2	Model	65
3.3	The quadratic part of the action	67
3.4	The non-quadratic part of the action	68
3.5	Conclusion	72
4	Polarization of a charge qubit strongly coupled to a voltage-driven quantum point contact	75
4.1	Introduction	75
4.2	Model	77
4.3	Results	80
4.4	Discussion	82
4.5	Conclusion	83
	Appendix 4.A Numerical method	84
	Appendix 4.B Many channels	87
	Appendix 4.C Choice of scattering matrices	89
	Appendix 4.D Inclusion of spin	92
5	Ballistic transmission through a graphene bilayer	97
5.1	Introduction	97
5.2	Model	98
5.3	Transmission probabilities	101
5.4	Results	102
5.5	Dependence on the potential in the contact region	106
5.6	Conclusion	108
	Appendix 5.A Transmission eigenvalues	109
	Appendix 5.B Four- vs. two-band Hamiltonian	110
6	Valley-isospin dependence of the quantum Hall effect in a graphene p-n junction	115
6.1	Introduction	115
6.2	Analytical theory	116

6.3	Numerical theory	121
6.4	Conclusion	123
7	Calculation of the conductance of a graphene sheet using the Chalker-Coddington network model	127
7.1	Introduction	127
7.2	Formulation of the scattering problem	129
7.2.1	Scattering Matrix	129
7.2.2	Transfer matrix	132
7.2.3	Real-space formulation	133
7.3	Formulation of the network model	134
7.4	Correspondence between scattering matrices of	137
7.5	Numerical Solution	139
7.6	Conclusion	143
	Appendix 7.A Infinite-mass boundary condition for the network model	145
	Appendix 7.B Stable multiplication of transfer matrices	151
	Appendix 7.C Optimal choice of phases in the network model	152
	Samenvatting	157
	Samevatting	161
	List of publications	165
	Curriculum Vitæ	167

Chapter 1

Introduction

The theoretical foundation for the work reported on in this thesis is provided by the scattering theory of electron transport. When a conductor is small enough, electrons can traverse it without undergoing inelastic processes. (Inelastic processes include, among other things, collisions between electrons and interactions with phonons or photons.) Transport is then said to be coherent. Such small conductors (typical lengths are between a few nanometers and a few microns) can be thought of as electron wave guides. At a given energy, transport takes place through a discrete set of channels. Transport properties are characterized by a scattering matrix. This insight is due to Landauer [1].

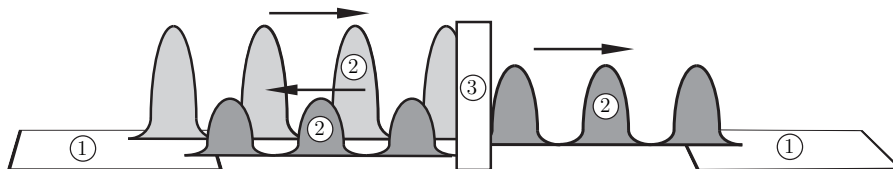


Figure 1.1. A one-dimensional scattering problem: A wave (2) impinges on a scattering center (3). As a result, a fraction T of the incident wave intensity is transmitted and a fraction $R = 1 - T$ is reflected. The conductance G of the scatterer equals $(e^2/h)T$.

In Fig. 1.1 the three main ingredients of a scattering problem are schematically indicated. These are (1) a set of reservoirs that emit and absorb particles, (2) the particles themselves, that propagate as waves between the reservoirs and (3) a scatterer that obstructs the free propagation

of waves.

In this thesis, we consider two classes of problems. The first class results when the physical quantities that characterize the reservoirs or those that characterize the scatterer are not constant in time. The time-dependence can have several causes: (1) An experimentalist pressed a button or turned a knob and changed the value of a system parameter such as the external bias voltage or the magnetic field. (2) The internal dynamics of the reservoirs or scatterer causes them to evolve significantly on time-scales that are of the same order as those associated with the electrons being transported. (3) The state of a reservoir or of the scatterer changes due to interactions with the electrons being transported. Situations of this kind are considered in Chapters 2, 3 and 4. The second class of problems results when wave propagation is described by the Dirac equation rather than the Schrödinger equation. The Dirac equation describes excitations in a recently discovered form of carbon called graphene, and forms the basis of Chapters 5, 6, and 7.

In this introductory chapter we give some background to the main topics and methods of this thesis.

1.1 Scattering theory of electron transport

We start by briefly discussing the scattering theory of electron transport, known as the Landauer-Büttiker formalism [1, 2]. (For a more detailed review, see [3].)

A coherent conductor such as the one in Fig. 1.2 is characterized by a scattering matrix. For the purpose of introducing the scattering matrix, we consider a two terminal device, but note that the theory readily generalizes to more terminals. We denote the two terminals left and right. The scattering matrix $s(E)$ is defined at a given energy E . Without loss of generality we may take the number N of channels for left-incident electrons to be the same as the number of channels for right-incident electrons. Then $s(E)$ is a $2N \times 2N$ matrix with four $N \times N$ sub-blocks

$$s(E) = \begin{pmatrix} r(E) & t'(E) \\ t(E) & r'(E) \end{pmatrix}. \quad (1.1)$$

The entries of these sub-blocks are reflection and transmission amplitudes. An electron with energy E that enters the conductor at the left terminal in channel n has an amplitude $r_{mn}(E)$ to be reflected back into the left

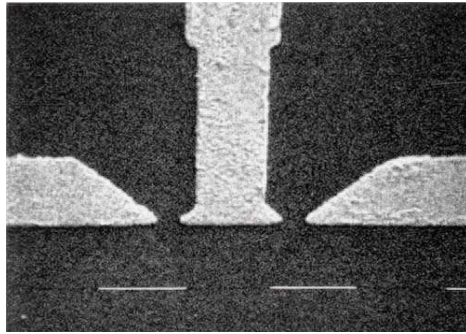


Figure 1.2. One of the very first fabricated coherent conductors. The figure shows a scanning electron micrograph of a double quantum point contact. The bright regions are electrostatic gate electrodes. They sit on top of a GaAs-AlGaAs heterostructure. The heterostructure contains a two dimensional electron gas. The electrodes deplete charge in the regions underneath them, thus defining a barrier with two small openings or quantum point contacts. The white lines at the bottom of the figure denote a length of $1 \mu\text{m}$. (From van Houten et al [4].)

terminal in channel m and an amplitude $t_{mn}(E)$ to be transmitted into the right terminal in channel m . Similarly, an electron that enters at the right terminal in channel n has an amplitude $r'_{mn}(E)$ to be reflected back into the right terminal in channel m and an amplitude $t'_{mn}(E)$ to be transmitted into the left terminal in channel m .

Transport properties are expressed in terms of the eigenvalues $T_n(E)$ of the transmission matrix product

$$T(E) = t(E)t(E)^\dagger. \quad (1.2)$$

(Our choice of using the left to right transmission amplitudes is arbitrary. As a consequence of the unitarity of the scattering matrix, the nonzero eigenvalues of tt^\dagger and $t't'^\dagger$ are identical.) The eigenvalues T_n lie between zero and one.

Suppose now that the conductor is connected to two large reservoirs. In the left (+) and right (-) reservoirs, the electrons are described by Fermi distributions

$$f_\pm(E) = \frac{1}{1 + \exp[(E - E_F \mp eV/2)/k_B T]}, \quad (1.3)$$

where e is the electron charge, V is the voltage bias across the conductor, E_F is the Fermi energy, k_B is Boltzmann's constant and T is the

temperature. Let $I(t)$ be the Heisenberg operator for current through the conductor. The expectation value for the current through the conductor $\bar{I} = \langle I(t) \rangle$ is time-independent since there are no time-dependent external fields. A central result of the scattering theory is the Landauer formula, that relates \bar{I} to T_n . The formula reads

$$I = \frac{e}{2\pi\hbar} \sum_n \int dE T_n(E) [f_+(E) - f_-(E)]. \quad (1.4)$$

Due to the difference between Fermi functions, the integrand is non-zero in an interval of a few times $\max\{eV, k_B T\}$ around the Fermi energy. This has to be compared to the energy scale at which $T_n(E)$ is constant. This is the Thouless energy E_{Th} . The low-temperature, small-voltage regime is defined by $eV, k_B T \ll E_{\text{Th}}$. (It must be noted that often great experimental effort is needed to enter this response regime.) In this regime, we may evaluate $T_n(E)$ at the Fermi energy E_F and take it outside the integral. Using the fact that $\int dE [f_+(E) - f_-(E)] = eV$ independent of temperature, we obtain $I = GV$ with the linear response conductance

$$G = \frac{e^2}{2\pi\hbar} \sum_n T_n. \quad (1.5)$$

Since $T_n \leq 1$, this result means that each transport channel n contributes at most $G_Q = e^2/2\pi\hbar$ to the conductance.

The conductance only contains information about the time averaged current \bar{I} . The current fluctuations contain additional information. The fluctuations are characterized by the Fourier transform of the current-current correlation function, which is known as the power spectrum $P(\omega)$ of the current noise,

$$P(\omega) = 2 \int_{-\infty}^{\infty} dt e^{i\omega t} [\langle I(t)I(0) \rangle - \bar{I}^2]. \quad (1.6)$$

The noise can also be expressed in terms of the transmission eigenvalues T_n . In the regime, $\omega \ll eV, k_B T \ll E_{\text{Th}}$, the general result is

$$P = \frac{e^2}{\pi\hbar} \left[2k_B T \sum_n T_n^2 + eV \coth\left(\frac{eV}{2k_B T}\right) \sum_n T_n(1 - T_n) \right]. \quad (1.7)$$

There are two contributions to this result. The first is thermal, i.e. fluctuations induced by the finite temperature of the system. The second

contribution persists at zero temperature and is known as shot noise. The thermal noise is related to the conductance G by the fluctuation-dissipation theorem and contains no information not already contained in G . Indeed, if we take the limit $eV/k_B T \rightarrow 0$, Eq. (1.7) reduces to

$$P_{\text{thermal}} = 4k_B T G. \quad (1.8)$$

The shot noise is more interesting because it contains information about temporal correlations between electrons that is not contained in G . For a review of this topic see Ref. [5] or for a tutorial see Ref. [6]. An expression for the zero temperature shot noise is obtained from Eq. (1.7) by taking the limit $k_B T/eV \rightarrow 0$ to find

$$P_{\text{shot}} = \frac{e^2}{\pi\hbar} eV \sum_n T_n (1 - T_n). \quad (1.9)$$

The $T_n(1 - T_n)$ structure of this result implies that neither a perfectly reflecting channel ($T_n = 0$) nor a perfectly transmitting channel ($T_n = 1$) contributes to shot noise.

1.2 The Keldysh technique

In this section we introduce a method that is used in Chapters 2, 3 and 4 of this thesis. It is a Green function technique suitable for analyzing many-body systems out of equilibrium. We will use it to investigate time-dependent scattering as well as interaction phenomena. The technique is named after its principal inventor L. V. Keldysh [7]. The work of Keldysh is related to that of Feynman and Vernon [8] and Schwinger [9]. For more details, references, and applications see the comprehensive review [10]. Tutorial derivations of the theory can be found in Refs. [11, 12, 13]. Here we discuss only the most basic concepts of the full theory.

A system is in equilibrium when the Hamiltonian H that governs its dynamics is time-independent and the state of the system is characterized by a density matrix $\rho = Z^{-1} e^{-\beta(H - \mu\mathcal{N})}$, with \mathcal{N} the number of particles, μ the chemical potential, and Z the partition function $Z = \text{tr} e^{-\beta(H - \mu\mathcal{N})}$. For such systems, the equilibrium Green function technique can be used to calculate expectation values of observables [14]. The central object is the so-called retarded Green function and the technique provides a systematic procedure to compute it.

There are many situations that fall beyond the scope of equilibrium theory. For instance, a system can be prepared in a non-equilibrium initial state and its subsequent relaxation studied. An open system can be in contact with an environment that drives it away from equilibrium. This is the case when different reservoirs connected to the same system have different temperatures or chemical potentials. Non-equilibrium states also arise when time-dependent external fields are applied. In these situations it is no longer sufficient to know the retarded Green function only. More information is required in order to evaluate expectation values of observables. This information is contained in an additional Green function, called the Keldysh Green function. The Keldysh technique provides a procedure, formally similar to the one used in equilibrium theory, with which to compute all necessary Green functions.

We will consider electron systems, and therefore make definitions appropriate for fermions. The Keldysh Green function $K_{m,n}(t, t')$ and the retarded Green function $R_{m,n}(t, t')$ are defined as

$$K_{m,n}(t, t') \equiv -i \left\langle \left[a_m(t), a_n^\dagger(t') \right] \right\rangle, \quad (1.10a)$$

$$R_{m,n}(t, t') \equiv -i\theta(t - t') \left\langle \left\{ a_m(t), a_n^\dagger(t') \right\} \right\rangle, \quad (1.10b)$$

where $a_m^\dagger(t)$ is the Heisenberg-picture operator that creates an electron in a single-particle state m . While it does not provide new information, it is useful to define also the advanced Green function $A_{m,n}(t, t') \equiv R_{n,m}(t', t)^*$.

The key result of Keldysh's theory is this: The three Green functions constitute a matrix

$$G_{m,n}(t, t') = \begin{pmatrix} R_{m,n}(t, t') & K_{m,n}(t, t') \\ 0 & A_{m,n}(t, t') \end{pmatrix}, \quad (1.11)$$

that obeys two integro-differential equations that are formally similar to those known from equilibrium theory.

At this point it is usual to introduce the Keldysh time contour and contour ordered Green functions [10]. Since we will simply state rather than derive the integro-differential equations for G , we do not need to discuss contour ordering here. For completeness we only mention that $G_{m,n}(t, t')$ as we have defined it, is related to the contour ordered Green function $\hat{G}_{m,n}(t, t')$ as defined in Ref. [10] by the transformation $\hat{G}_{m,n}(t, t') = \tau_3 L^\dagger G_{m,n}(t, t') L$ where

$$\tau_3 = \begin{pmatrix} 1 & 0 \\ 0 & -1 \end{pmatrix}, \quad L = \frac{1}{\sqrt{2}} \begin{pmatrix} 1 & -1 \\ 1 & 1 \end{pmatrix}. \quad (1.12)$$

In order to find equations that determine G , the system is split up into a single-particle problem that can be solved exactly and a perturbation. In the single-particle basis that diagonalizes the unperturbed system, the equations for G are of the form

$$(i\partial_t - \varepsilon_m)G_{m,n}(t, t') - \sum_l \int d\tilde{t} \Sigma_{m,l}(t, \tilde{t})G_{l,n}(\tilde{t}, t') = \delta(t - t')\delta_{m,n}I_{2 \times 2}, \quad (1.13a)$$

$$(-i\partial_{t'} - \varepsilon_n)G_{m,n}(t, t') - \sum_l \int d\tilde{t} G_{m,l}(t, \tilde{t})\Sigma_{l,n}(\tilde{t}, t') = \delta(t - t')\delta_{m,n}I_{2 \times 2}, \quad (1.13b)$$

where $I_{2 \times 2}$ is the 2×2 unit matrix and ε_m is the energy of level m . The self-energy

$$\Sigma_{m,n}(t, t') = \begin{pmatrix} \Sigma_{m,n}^{(R)}(t, t') & \Sigma_{m,n}^{(K)}(t, t') \\ 0 & \Sigma_{m,n}^{(A)}(t, t') \end{pmatrix} \quad (1.14)$$

takes account of the perturbation. The perturbation may for instance be due to electron-electron interactions, electron-phonon interactions or impurity scattering. (See Ref. [10] for details.) The self-energy can also take into account time dependent external fields. In Chapter 2 we use it to describe the presence of reservoirs. The formalism is able to deal with reservoirs characterized by arbitrary time-dependent distribution functions. As in equilibrium, the self-energy is the sum of all amputated one-particle-irreducible diagrams. (See for example Ref. [15] for a detailed exposition of equilibrium diagrammatics.) The only difference is that now the propagators have an additional 2×2 matrix structure.

In equilibrium, the self-energy determines the effective single-particle spectrum. Outside equilibrium it also dictates how particles are distributed among the single-particle levels. The reader who wants to know more is referred to Appendix 1.A where we work through a simple example that employs the Keldysh technique.

1.3 Photons

In Sec. 1.1 we considered ideal reservoirs. As a result, the voltage across the conductor did not fluctuate. This was an idealization. A more realistic

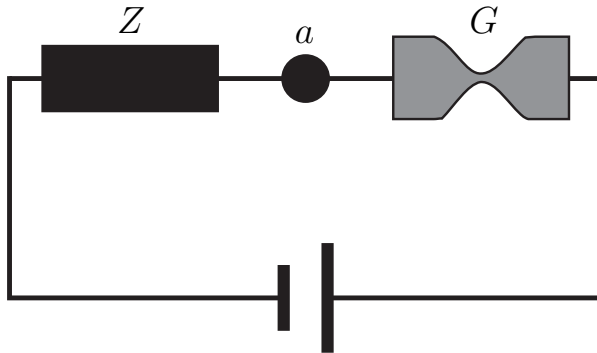


Figure 1.3. Circuit that models fluctuations in the bias voltage across a coherent conductor with conductance G . The voltage fluctuations are produced by current fluctuations in the coherent conductor. The external circuit is represented by an impedance Z . The voltage in node a develops fluctuations when $ZG > 1$.

model results when one connects an impedance Z in series with the coherent conductor with conductance G and then biases the combined structure with an ideal voltage [16, 17]. (See Fig. 1.3). The impedance represents the external circuit to which the coherent conductor is connected. The ideal bias voltage is divided between the impedance and the coherent conductor. This division is not constant. Fluctuations in the current through the coherent conductor are converted into voltage fluctuations in the shared node. The fluctuations become important when $ZG > 1$.

One way to describe these fluctuations is to treat the external circuit as a quantum system [18] in the same way that the coherent conductor is a quantum system. This was first done in the context of ultra small tunnel junctions [19, 20, 21]. Generalization to arbitrary coherent conductors was achieved in Refs. [16, 17, 22]. The construction is based on the theory of Caldeira and Leggett [23, 24] and exploits the fact that any impedance can be represented by means of a quadratic Hamiltonian for a set of bosonic modes. As a result, the description that emerges for a coherent conductor coupled to an external circuit is that of a quantum system in contact with a bosonic bath. The bosonic modes that couple to the coherent conductor are photons [18, 25, 26]. They quantize the energy stored in electromagnetic fields in the neighborhood of the coherent conductor.

Here we briefly discuss this quantization. We define a variable φ such that the potential difference between the node and infinity (or earth) is

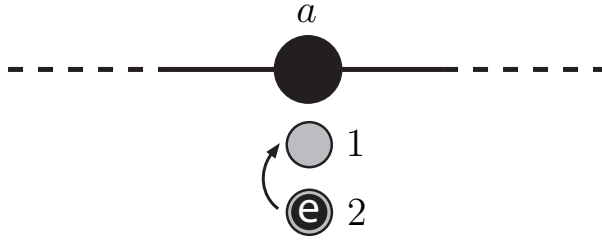


Figure 1.4. A two level system is placed in the vicinity of node a . The two level system consists of an electron that can hop between two localized states 1 and 2. The photons associated with voltage fluctuations in node a interact with the electron.

$V = d\varphi/dt$. This potential difference is related to the charge Q stored on the node by its capacitance $V = Q/C$. The energy stored in the resulting electric field is $H_C = Q^2/2C$ so that

$$\frac{d\varphi}{dt} = \frac{\partial H_C}{\partial Q}. \quad (1.15)$$

This is a Hamilton equation of motion with φ a generalized coordinate and Q its conjugate momentum. Note that H_C is not the full Hamiltonian of the circuit but that we assume it is the only term that contains Q .

Quantization of these degrees of freedom then follows the standard procedure. Q and φ are promoted to operators and the commutation relation

$$[\hat{\varphi}, \hat{Q}] = i\hbar \quad (1.16)$$

is imposed. This allows us to define operators b and b^\dagger through

$$b = \frac{\hat{Q}}{\sqrt{2\hbar C\omega}} - i\sqrt{\frac{C\omega}{2\hbar}}\hat{\varphi}, \quad (1.17)$$

that obey the bosonic commutation relation $[b, b^\dagger] = 1$. The parameter ω is arbitrary at this point, but a natural choice is dictated by the dynamics of the circuit under consideration. The particles associated with b and b^\dagger are photons.

We must next consider the interaction of quantized radiation with other quantum systems. This interaction can be derived from the fundamental $\mathbf{j} \cdot \mathbf{A}$ coupling term of quantum electrodynamics [27]. A simple example

serves to illustrate the general principle. Consider therefore an electron that can hop between two localized, spatially separated states $|1\rangle$ and $|2\rangle$ in the vicinity of the node a . For definiteness, let us say that when the electron is in state $|1\rangle$ it is closer to node a than when it is in state $|2\rangle$. (See Fig. 1.4). What happens when the electron is moved closer to or further from the metallic node a ? The electron induces a charge on the node. (This charge screens the interior of the node from the electric field produced by the electron.) If the electron is far from the node, it produces only a small electric field at the node. In this case the induced charge on the node is also small. When the electron is closer to the node, the electric field it produces at the node is larger and so too is the charge it induces on the node. Thus we see that hopping of the electron between states $|1\rangle$ and $|2\rangle$ is accompanied by a change of the charge on the node a . The charge on node a in turn produces its own electric field to which the electron is sensitive. We now develop a quantum mechanical description of this dynamics.

We start by looking at the electron in the absence of any electromagnetic fields when its Hamiltonian is $H = \gamma |2\rangle \langle 1| + \gamma^* |1\rangle \langle 2|$. Here γ is the hopping amplitude from $|1\rangle$ to $|2\rangle$. How is the Hamiltonian modified in the presence of electromagnetic fields? First, let us consider classical fields. We also restrict ourselves to the regime where the electric field dominates, so that we can neglect the magnetic field by setting $\nabla \times \mathbf{A} = 0$. We choose the gauge in which the scalar potential is zero and the electric field is given in terms of the vector potential as

$$\mathbf{E} = -\frac{\partial \mathbf{A}}{\partial t}. \quad (1.18)$$

In this gauge, the effect of the electric field is to modify the hopping amplitude

$$\gamma \rightarrow \gamma \exp\left(\frac{ie}{\hbar} \int_{1 \rightarrow 2} d\mathbf{l} \cdot \mathbf{A}\right), \quad (1.19)$$

where the line-integral runs along any path from site 1 to site 2.

The next step is to note that a charge Q on node a produces an electric field \mathbf{E} proportional to Q : If we double the charge, we double the electric field everywhere in space. From Eq. (1.18) then follows

$$\frac{\partial}{\partial t} \int_{1 \rightarrow 2} d\mathbf{l} \cdot \mathbf{A} = - \int_{1 \rightarrow 2} d\mathbf{l} \cdot \mathbf{E} \propto Q = CV. \quad (1.20)$$

Since the voltage V in node a is related to the phase φ through $d\varphi/dt = V$, it follows that

$$\int_{1 \rightarrow 2} d\mathbf{l} \cdot \mathbf{A} = \alpha\varphi, \quad (1.21)$$

where α is a dimensionless proportionality constant. This equation allows us to go over to a quantum description. The classical phase φ is replaced by the quantum mechanical operator $\hat{\varphi}$. If H_c is the Hamiltonian for the circuit degrees of freedom, then the total Hamiltonian for the circuit plus electron is $H = H_c + H_e$, where

$$H_e = \gamma e^{i\alpha e \hat{\varphi}/\hbar} |2\rangle \langle 1| + \gamma^* e^{-i\alpha e \hat{\varphi}/\hbar} |1\rangle \langle 2| \quad (1.22)$$

describes the hopping of the electron between sites, in the presence of a quantized electric field.

Note the following: Due to the commutation relation between \hat{Q} and $\hat{\varphi}$ (Eq. 1.16), the operator $\exp(i\alpha e \hat{\varphi}/\hbar)$ shifts the charge on the node a by an amount αe . In other words, if $|q\rangle$ is an eigenstate of \hat{Q} with eigenvalue q , then $|q + \alpha e\rangle \equiv \exp(i\alpha e \hat{\varphi}/\hbar) |q\rangle$ is an eigenstate of \hat{Q} with eigenvalue $q + \alpha e$. Looking again at Eq. (1.22), we see that electron hopping is accompanied by a change in the charge on the node as we anticipated earlier.

Finally, we note that $\hat{\varphi}$ can be expressed in terms of the boson operators b and b^\dagger as $\hat{\varphi} = -i\sqrt{\hbar/2C\omega}(b^\dagger - b)$. Thus, H_e is given by

$$H_e = \gamma e^{\lambda(b^\dagger - b)} |2\rangle \langle 1| + \gamma^* e^{-\lambda(b^\dagger - b)} |1\rangle \langle 2|, \quad (1.23)$$

with $\lambda = \alpha e/\sqrt{2\hbar\omega C}$. This makes it clear that processes occur where the electron absorbs or emits photons while hopping between sites 1 and 2.

In Chapter 3 of this thesis, we use a device similar to the two level system we have considered above to detect photons at a given energy that are produced by a voltage biased quantum point contact.

1.4 Graphene: Dirac Fermions

Graphene is a material consisting of a single atomic layer of carbon atoms. It can be thought of as a single layer of graphite. Over several decades, its unusual band structure has stimulated the interest of theorists [28, 29, 30, 31, 32]. Until recently however, it was not clear whether graphene is simply a theorist's toy or whether it exists in nature. This question was only

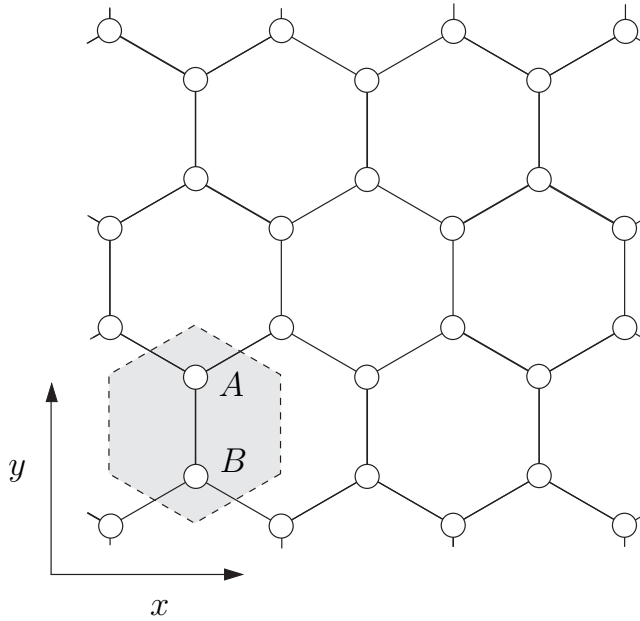


Figure 1.5. The two dimensional honeycomb lattice of graphene. The hexagonal unit cell is indicated by a shaded hexagon. Each unit cell contains two atoms, one belonging to the A sublattice and one to the B sublattice.

answered in 2004 when the group of Andrei Geim in Manchester reported the successful fabrication of graphene devices for electron transport experiments [33]. Subsequent experimental studies, particularly those performed in the quantum Hall regime [34, 35], confirmed the theoretical prediction that low energy excitations are described by a two dimensional Dirac equation. Several tutorials [36, 37, 38, 39, 40] and reviews [41, 42, 43, 44] provide an overview of recent developments. Here we discuss only the very basics.

Graphene has a two dimensional honeycomb lattice. A honeycomb lattice consists of two triangular sublattices denoted A and B . These are arranged such that each A (B) sublattice site is at the centroid of the triangle formed by its nearest neighbor sites. These neighboring sites all belong to the B (A) sublattice. This is illustrated in Fig. 1.5. The distance between nearest neighbors on the lattice is $a \simeq 1.42 \text{ \AA}$.

The Brillouin zone corresponding to this lattice is hexagonal. It is de-

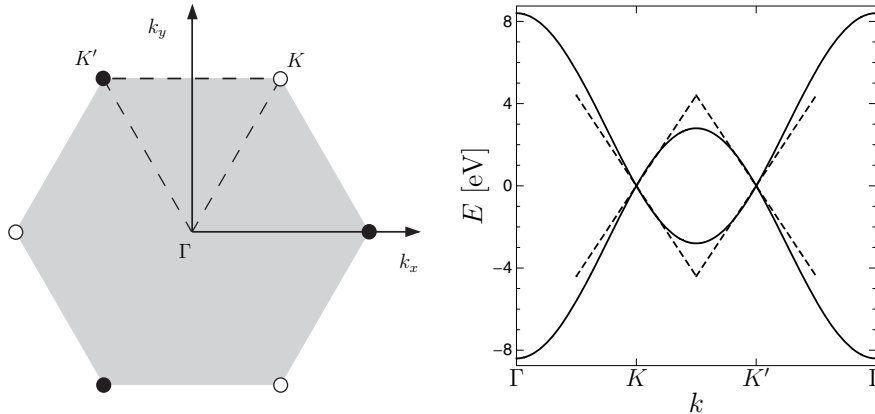


Figure 1.6. Left panel: The Brillouin zone of the graphene lattice. The K and K' points at the corners of the Brillouin zone are indicated by open and filled circles respectively. The three K points are connected by reciprocal lattice vectors and are therefore equivalent. The same holds for the K' points. There is no reciprocal lattice vector connecting K and K' , and these two corners are inequivalent. The center of the Brillouin zone is at the point Γ . The dashed lines indicate the contour along which the dispersion is plotted in the right panel. Right panel: The energy dispersion of graphene along the lines ΓK , $K K'$, and $K' \Gamma$ in the Brillouin zone. At the two inequivalent corners K and K' , the conduction and valence bands touch at energy $E = 0$, the Fermi energy of undoped graphene. These are called Dirac points. Close to the Dirac points the dispersion of both the conduction and valence bands are linear. The associated excitations (particles or holes) are described by the Dirac equation (1.25).

picted in Fig. 1.6. Below we will see that wave vectors in the corners of the Brillouin zone are relevant for describing low-energy excitation. We therefore mention that the six corners of the Brillouin zone can be partitioned into two sets of three, indicated in Fig. 1.6 by black and white dots respectively. Members of the same set are connected by basis vectors of the reciprocal lattice and hence refer to the same physical state. This means that the Brillouin zone has two inequivalent corners. We take these to be

$$\mathbf{K} = \frac{2\pi}{3a} \left(\hat{x} + \frac{1}{\sqrt{3}} \hat{y} \right), \quad \mathbf{K}' = \frac{2\pi}{3a} \left(-\hat{x} + \frac{1}{\sqrt{3}} \hat{y} \right). \quad (1.24)$$

The band structure of the conduction and valence bands is obtained by associating one orbital with each lattice site and constructing a tight

binding Hamiltonian. To good approximation only nearest neighbor hopping has to be taken into account. The nearest neighbor hopping energy is $t \simeq 3 \text{ eV}$. The resulting energy dispersion is shown in Fig. 1.6. It is seen that the conduction and valence bands touch. Touching occurs at so-called Dirac points situated at the corners of the Brillouin zone. The energy at which the bands touch is equal to the Fermi energy of undoped graphene. Like a semi-conductor, undoped graphene therefore has a filled valence band and an empty conduction band. Unlike a semi-conductor though, there is no energy gap between the valence and conduction bands. Graphene is therefore called a semi-metal.

We now examine the dispersion relation close to one of the two inequivalent Dirac points. To be definite, let us consider the Dirac point at \mathbf{K} . We define $\mathbf{p} = \hbar(\mathbf{k} - \mathbf{K})$ as the momentum associated with the wave vector \mathbf{k} and measured from a reference point $\hbar\mathbf{K}$. In the vicinity of $\hbar\mathbf{K}$, the dispersion relation reads $E = \pm v|\mathbf{p}|$ where $v = 3ta/2 \simeq 10^6 \text{ m/s}$ is the Fermi velocity. This describes two cones touching at the Dirac point. The positive sign refers to the conduction band while the negative sign refers to the valence band. Excitations travel at a group velocity $\mathbf{v}_g = \nabla_{\mathbf{p}}E = \pm v\hat{\mathbf{p}}$. The magnitude of the group velocity is equal to the Fermi velocity, independent of energy. Electrons in graphene behave like massless relativistic particles, traveling at the effective speed of light v regardless of their energy.

For excitations close to the Fermi energy of undoped graphene, the tight binding Hamiltonian can be expanded in momentum around either of the Dirac points. We consider here states in the vicinity of the \mathbf{K} point. A continuum description results in which the electron wave function $\Psi(\mathbf{r})$ is defined on the whole x - y plane such that $\exp(i\mathbf{K} \cdot \mathbf{r}) \times \Psi(\mathbf{r})$ interpolates the value of the tight-binding wave function defined on the honeycomb lattice. The continuum wave function Ψ satisfies $E\Psi = H\Psi$ where H is the Dirac Hamiltonian

$$H = v(\mathbf{p} - \boldsymbol{\alpha}) \cdot \boldsymbol{\sigma} + \phi. \quad (1.25)$$

Here $\boldsymbol{\alpha}$ is e times the magnetic vector potential in the x - y plane and ϕ is e times the electric scalar potential. Both of these have to be smooth on the scale of the inter-atomic distance a . In position representation, the momentum is $\mathbf{p} = -i\hbar(\partial_x, \partial_y)$. The vector $\boldsymbol{\sigma} = (\sigma_x, \sigma_y)$ contains the Pauli matrices

$$\sigma_x = \begin{pmatrix} 0 & 1 \\ 1 & 0 \end{pmatrix}, \quad \sigma_y = \begin{pmatrix} 0 & -i \\ i & 0 \end{pmatrix}. \quad (1.26)$$

The Hamiltonian acts on spinors $\Psi = (\psi_A, \psi_B)$, with ψ_A the amplitude to be on the A sublattice and ψ_B the amplitude to be on the B sublattice. This spinor degree of freedom is called pseudospin to distinguish it from the real electron spin, which does not appear in the Eq. (1.25).

The excitations around the Dirac point at \mathbf{K}' are also described by the Dirac Hamiltonian of Eq. (1.25). The fact that excitations around both Dirac points are present in weakly doped graphene results in a two-fold degeneracy of eigenstates. The associated degree of freedom is called the valley index. As long as the spatial variation of α and ϕ is smooth on the scale of the inter-atomic distance a , and we restrict ourselves to energies $E \ll \hbar v/a$, the valleys remain uncoupled in an infinite graphene sheet. At the edges of a finite sheet however, the valleys can be coupled by the boundary [45].

The Dirac equation gives rise to unusual transport properties. This is illustrated by the following example. Consider an electrostatic potential barrier $\phi(\mathbf{r})$ in the region $0 < x < L$. Usually such a potential introduces scattering. A particle incident on ϕ from the left ($x < 0$) is reflected back with probability R and transmitted to the right ($x > L$) with probability $T = 1 - R$. If the energy E of the incident particle is less than the barrier height, transmission through the barrier is strongly suppressed and the reflection probability tends to unity. For energies larger than the barrier height, the probability for transmission becomes finite. However, only in the limit $E \gg \max \phi$ does the transmission probability approach unity.

Dirac excitations in graphene do not conform to this picture. Due to Klein tunneling [46, 47], transmission is no longer strongly suppressed when the barrier height exceeds the energy of the wave function. This is illustrated in Fig. 1.7.

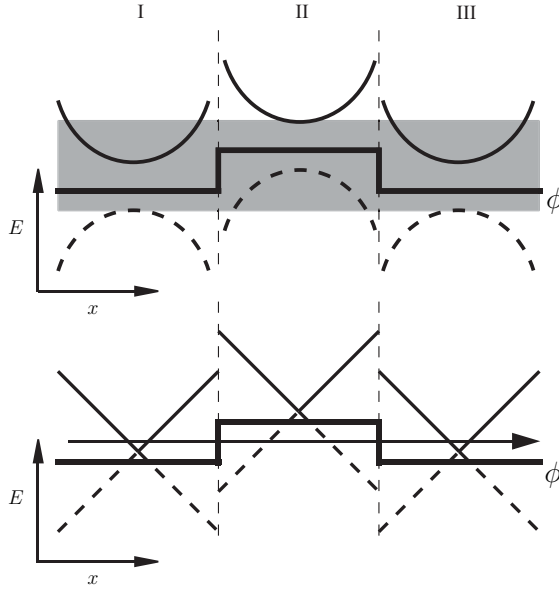


Figure 1.7. Conventional tunneling vs. Klein tunneling. Top panel: A potential barrier $\phi(x)$ in a conventional metal or semi-conductor. The valence band (dashed curve) and the conduction band (solid curve) to the left of the barrier (I), in the barrier region (II) and to the right of the barrier (III) are indicated. The region between the bottom of the conduction band in region (II) and the top of the valence band in regions (I) and (III) is shaded. In this region there are no propagating states connecting regions (I) and (III). To get through the barrier, an electron has to tunnel through the classically forbidden region. The tunneling amplitude falls off exponentially as a function of the barrier length. As a result transport between regions (I) and (III) is strongly suppressed. Bottom panel: A potential barrier $\phi(x)$ in graphene. In each of the regions (I), (II) and (III), the valence band (dashed curve) and conduction band (solid curve) touch. As a result there are propagating states connecting the regions (I) and (III) at all energies. There is no suppression of transport at incident energies below the barrier height. In fact, as Eq. (1.28) indicates, there is perfect transmission at normal incidence.

Furthermore, at normal incidence, transmission is always perfect. To see this, we solve the Dirac equation with $\phi(x)$ that depends only on the x -coordinate. We focus on incident waves that propagate normal to the potential barrier. (Normal incidence means that the wave number in the y -direction is zero, and the wave function only depends on the x coordinate.) In this case, the time-independent Dirac equation for given energy E can be rewritten as

$$\partial_x \Psi(x) = \frac{i}{\hbar v} \sigma_x [E - \phi(x)] \Psi(x), \quad (1.27)$$

and the solution is found by straight-forward integration. Corresponding to any energy E , we find a left-incident (+) and a right-incident (-) solution

$$\Psi_{\pm}(x) = \frac{e^{\pm iEx/\hbar v}}{\sqrt{2}} \begin{pmatrix} 1 \\ \pm 1 \end{pmatrix} \times \begin{cases} 1 & x < 0 \\ \exp\left(\mp i \int_0^x dx' \phi(x')/\hbar v\right) & 0 < x < L \\ \exp\left(\mp i \int_0^L dx' \phi(x')/\hbar v\right) & x > L \end{cases}. \quad (1.28)$$

Remarkably, these wave functions each contain an incident component and a transmitted component but no reflected component. At normal incidence, the transmission probability is always unity. This is particularly striking for incident energies smaller than the height of the potential barrier where one would normally expect almost perfect reflection.

The phenomenon we have just encountered is sometimes referred to as the absence of back-scattering in graphene [48]. It has some surprising consequences. Adding disorder to a graphene sample can enhance the conductivity [49, 50]. Furthermore, disorder that is smooth on the scale of the lattice constant cannot turn graphene into an insulator [51, 52, 53].

1.5 Bilayer graphene

In Chapter 5 of this thesis we consider bilayer graphene, i.e. two layers of carbon atoms one on top of the other. The way the two layers are stacked is illustrated in Fig. 1.8. The A sublattice of the one layer is directly above the B sublattice of the other. Bilayer graphene has a unit cell containing four atoms (two per carbon layer). The Brillouin zone is identical to that of monolayer graphene. Close to the K and K' corners of the Brillouin zone,

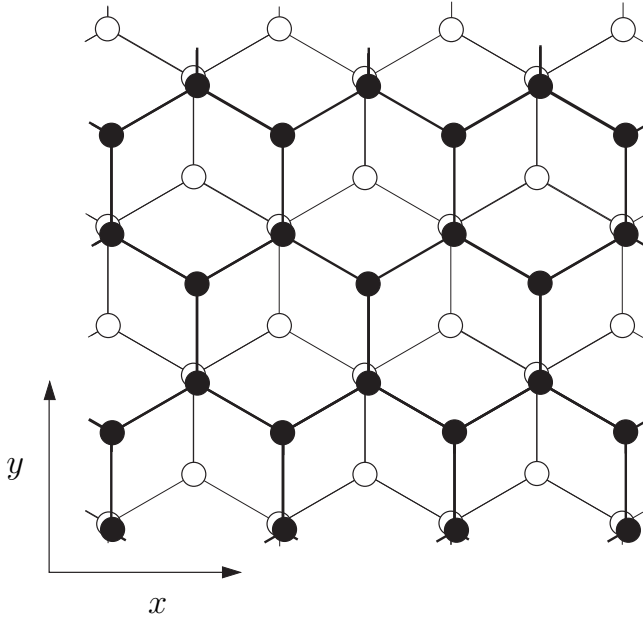


Figure 1.8. A graphene bilayer consists of two monolayers stacked one on top of the other. In order to be able to distinguish the two layers, open circles were used to indicate carbon atoms in the bottom layer while filled circles were used to indicate carbon atoms in the top layer. The B sublattice of the top layer is directly above the A sublattice of the bottom layer.

the bilayer is described by a 4×4 long wavelength Hamiltonian [54, 55, 56]

$$H = \begin{pmatrix} \phi & v(p_x - ip_y) & t_{\perp} & 0 \\ v(p_x + ip_y) & \phi & 0 & v_3(p_x - ip_y) \\ t_{\perp} & 0 & \phi & v(p_x + ip_y) \\ 0 & v_3(p_x + ip_y) & v(p_x - ip_y) & \phi \end{pmatrix}. \quad (1.29)$$

(We only consider the case of zero magnetic field.) The upper left 2×2 block is the Dirac Hamiltonian of Eq. (1.25) and describes the electron dynamics inside one layer. The lower right 2×2 block is obtained by interchanging the A and B sublattices in the Dirac Hamiltonian and describes the electron dynamics in the other layer. The two layers are coupled by matrix elements t_{\perp} and $v_3(p_x \pm ip_y)$. The interlayer coupling parameters have values $t_{\perp} \simeq 0.4 \text{ eV}$ and $v_3 \simeq 10^5 \text{ m/s}$. The term proportional to

v_3 breaks the isotropy of the dispersion relation, introducing a triangular distortion known as “trigonal warping”. In Chapter 5 we ignore this complication and calculate the transport properties of the bilayer for $v_3 = 0$. A complete calculation, including the effects of trigonal warping, has subsequently been published in Refs. [57, 58].

1.6 This Thesis

1.6.1 Chapter 2

In Chapter 2 we present a derivation of the Keldysh action of a general multi-channel time-dependent scatterer in the context of the Landauer-Büttiker approach. This result is then applied in two subsequent chapters.

In general the Keldysh action of a system is defined as $\mathcal{A} = \ln \mathcal{Z}$, where

$$\mathcal{Z} = \text{Tr} \left[\mathcal{T}^+ \exp \left\{ -i \int_{t_0}^{t_1} dt \mathcal{H}^+(t) \right\} \rho_0 \mathcal{T}^- \exp \left\{ i \int_{t_0}^{t_1} dt \mathcal{H}^-(t) \right\} \right]. \quad (1.30)$$

In this expression, ρ_0 is the initial density matrix of the system. This is evolved forwards and backwards in time with two different time-dependent Hamiltonians $\mathcal{H}^\pm(t)$. For the purpose of this introduction we set $\mathcal{H}^\pm = H + \chi_\pm(t)Q$ where H is the actual Hamiltonian of the system, Q is a system coordinate and $\chi_\pm(t)$ are arbitrary functions of time. (Generalization to more fields, each coupling to a different system coordinate, is straight forward.) \mathcal{Z} and \mathcal{A} are functionals of χ_\pm . The ordering symbol \mathcal{T}^+ indicates time-ordering of operators with the largest time-argument to the left, while \mathcal{T}^- time-orders with the largest argument to the right.

Why are we interested in this object? Let us firstly mention its most direct application, namely to evaluate time-ordered correlators of the coordinate Q . This is done by taking functional derivatives with respect to $\chi_+(t)$ and $\chi_-(t)$. We obtain

$$\begin{aligned} & \left\langle \mathcal{T}^- \left(\prod_{j=1}^M Q(t_j) \right) \mathcal{T}^+ \left(\prod_{k=1}^N Q(t'_k) \right) \right\rangle \\ &= \prod_{j=1}^M \left(-i \frac{\delta}{\delta \chi^-(t_j)} \right) \prod_{k=1}^N \left(i \frac{\delta}{\delta \chi^+(t'_k)} \right) \mathcal{Z}[\chi] \Big|_{\chi=0}. \end{aligned} \quad (1.31)$$

A less obvious application is the following. Suppose the coordinate Q of the system for which we know \mathcal{A} (call it system A) is coupled to another system (B). Knowing $\mathcal{A}[\chi_{\pm}]$, we can then calculate the influence that system A has on system B. (For this reason Feynman and Vernon [8] call \mathcal{Z} the influence functional.) In chapters 3 and 4 for instance, we calculate how specific measuring devices respond when coupled to a coherent conductor, starting from an expression for the Keldysh action \mathcal{A} of the conductor.

Previous studies of the Keldysh action focused on weakly interacting disordered electron systems [59, 60]. We consider the Keldysh action of an arbitrary coherent conductor connected to electron reservoirs. For such systems an explicit expression for $\mathcal{A}[\chi]$ was known (see for instance Chapter 3 or Ref. [61]) only in the case where the fields χ_{\pm} couple to electrons in the reservoirs rather than in the scattering region. We wanted to consider a setup where the scattering potential depends on the state of an adjacent quantum system (Chapter 4). In Chapter 2 we therefore generalized the known result for the action \mathcal{A} to the situation where the fields χ_{\pm} couple to electrons inside the scattering region.

1.6.2 Chapter 3

In Chapter 3 we analyze the operation of a quantum tunneling detector coupled to a coherent conductor. Use is made of the theory developed in Chapter 2. The coherent conductor is biased with a voltage V . The circuit that connects the coherent conductor to the voltage biased electron reservoirs has a finite impedance. As a result, current fluctuations in the coherent conductor are converted into voltage fluctuations on top of V . The fluctuations are detected as photons. The detector is capable of frequency-resolved detection. We demonstrate that for frequencies larger than $eV/2\pi\hbar$, the output of the detector is determined by two-photon processes, two-interacting-electron processes and the interference of both processes. Two-photon processes occur when the conductor emits two photons each with energy $< eV$ and both are detected. The second process occurs when the electromagnetic environment mediates an interaction between electrons in the conductor. As a result, a single photon of energy $> eV$ is emitted and picked up by the detector. We show how the individual contributions of these processes can be resolved in experiments.

1.6.3 Chapter 4

In Chapter 4 we study a charge qubit with level splitting ε coupled to a quantum point contact (QPC) driven by a bias voltage V . The charge qubit can be realized by the lowest two eigenstates of an electron trapped in double quantum dot. The qubit Hilbert space is spanned by a state $|1\rangle$ representing the electron localized in one dot, together with a state $|2\rangle$ representing the electron localized in the other dot. Because of the coupling to the qubit, the scattering matrix of the QPC depends on the state of the qubit. We define the qubit polarization as the probability to find the qubit in state $|1\rangle$. For given V , we calculate the the qubit polarization as a function of the qubit level splitting. Use is made of the theory developed in Chapter 2. In the limit of weak coupling, the qubit polarization shows cusps at $\varepsilon = \pm eV$. We show that, for stronger couplings, a plateau occurs for $|\varepsilon| \leq \pm eV/2$. Further increase of the coupling leads to a polarization $p_2 = [1 + \exp(\beta\varepsilon)]^{-1}$ corresponding to an effective temperature $\beta^{-1} \sim eV$.

1.6.4 Chapter 5

Here we calculate the Fermi energy dependence of the (time-averaged) current and shot noise in an impurity-free carbon bilayer (length $L \ll$ width W), and compare with known results for a monolayer [62]. We model the interlayer coupling by means of a hopping element $t_{\perp} = \hbar v/l_{\perp}$ between nearest neighbors in different layers. Here l_{\perp} is the inter-layer hopping length estimated to be on the order of ten times the inter-atomic distance. At the Dirac point of charge neutrality, the bilayer (l_{\perp} finite) transmits as two independent monolayers in parallel (l_{\perp} infinite): Both current and noise are resonant at twice the monolayer value, so that their ratio (the Fano factor) has the same 1/3 value as in a monolayer — and the same value as in a diffusive metal. The range of Fermi energies around the Dirac point within which this pseudo-diffusive result holds is smaller, however, in a bilayer than in a monolayer (by a factor l_{\perp}/L). It was subsequently shown by Moghaddam and Zareyan [58] that this conclusion holds only for lengths less than about 50 nm ($\simeq 30$ times l_{\perp}), because we ignored the effects of trigonal warping mentioned in Sec. 1.5.

1.6.5 Chapter 6

In Chapter 6 we consider a bipolar junction in a graphene nanoribbon in the high-magnetic field regime. In a bipolar junction a potential step

creates two regions, one p -doped and one n -doped. In the p -doped region, the Fermi energy is in the conduction band while in the n -doped region it is in the valence band. We consider the regime where the Hall conductance in both the p -doped and n -doped regions is $2e^2/h$. We calculate the two-terminal conductance G . In the absence of intervalley scattering, the result $G = (e^2/h)(1 - \cos \Phi)$ depends only on the angle Φ between the valley isospins (= Bloch vectors representing the spinor of the valley polarization) at the two opposite edges. This plateau in the conductance versus Fermi energy is insensitive to electrostatic disorder, while it is destabilized by the dispersionless edge state which may exist at a zigzag boundary. A strain-induced vector potential shifts the conductance plateau up or down by rotating the valley isospin.

1.6.6 Chapter 7

The Chalker-Coddington network model [63] (introduced originally as a model for percolation in the quantum Hall effect) is known to map onto the two-dimensional Dirac equation [64]. In Chapter 7 we show how the network model can be used to solve a scattering problem in a weakly doped graphene sheet connected to heavily doped electron reservoirs. We develop a numerical procedure to calculate the scattering matrix with the aid of the network model. For numerical purposes, the advantage of the network model over the honeycomb lattice is that it eliminates intervalley scattering from the outset. We avoid the need to include the heavily doped regions in the network model (which would be computationally expensive), by means of an analytical relation between the transfer matrix through the weakly doped region and the scattering matrix between the electron reservoirs. We test the network algorithm by calculating the conductance of an electrostatically defined quantum point contact and comparing with the tight-binding model of graphene. We further calculate the conductance of a graphene sheet in the presence of disorder in the regime where intervalley scattering is suppressed. We find an increase in conductance that is consistent with previous studies. Unlike the tight-binding model, the network model does not require smooth potentials in order to avoid intervalley scattering.

Appendix 1.A The Keldysh technique: an example

In this appendix we illustrate the use of the Keldysh technique with the following example. A quantum dot is connected to two reservoirs by means of tunnel barriers. One reservoir is grounded and we measure all energies relative to its Fermi energy. For times $t < 0$ the other reservoir is held at zero voltage too, and the dot is neutral and in equilibrium with the reservoirs. Consequently, the dot's chemical potential $\mu(t)$ is zero for $t < 0$. For times $t > 0$, a time-dependent voltage $V(t)$ is applied to one reservoir. We want to calculate the expectation value of the charge on the dot, as a function of time.

The dot can be modeled as a set of independent levels that are connected to reservoirs by tunneling. They are labeled by an integer m . The Green function G is diagonal in this basis, i.e. $G_{m,n}(t, t') = \delta_{m,n} G_m(t, t')$. Note that, since $a_m(t)$ and $a_m^\dagger(t)$ anti-commute to unity at coinciding times, the Keldysh Green function contains information about the occupation probability of levels. More precisely

$$K_m(t, t) = -i [1 - 2n_m(t)], \quad n_m(t) = \langle a_m^\dagger(t) a_m(t) \rangle, \quad (1.32)$$

with $n_m(t)$ the probability that level m is occupied at time t . The total number of electrons $n(t)$ on the dot is the sum of all the occupation probabilities $n(t) = \sum_m n_m(t)$.

The Green function $G_m(t, t')$ obeys the following equations

$$\begin{aligned} i\partial_t G_m(t, t') - [\varepsilon_m + \mu(t)] G_m(t, t') \\ - \int d\tilde{t} \Sigma(t, \tilde{t}) G_m(\tilde{t}, t') = \delta(t - t') I_{2 \times 2}, \end{aligned} \quad (1.33a)$$

$$\begin{aligned} -i\partial_{t'} G_m(t, t') - [\varepsilon_m + \mu(t')] G_m(t, t') \\ - \int d\tilde{t} G'_m(t, \tilde{t}) \Sigma(\tilde{t}, t') = \delta(t - t') I_{2 \times 2}. \end{aligned} \quad (1.33b)$$

A chemical potential $\mu(t)$ takes into account charging effects: When charge on the dot fluctuates so that it is no longer neutral, work has to be done against the electric field of the excess charge $Q(t)$ in order to add more charge to the dot. $\mu(t)$ is proportional to $Q(t)$, the proportionality constant being the capacitance C of the dot:

$$\mu(t) = \frac{1}{C} Q(t). \quad (1.34)$$

Assuming that the dot is neutral at time $t = 0$, $Q(t) = n(t) - n(0)$. The self-energy describes the tunneling of electrons between the dot and the reservoirs. Its components are explicitly

$$\Sigma^{(R)}(t, t') = -iE_{\text{Th}}\delta(t - t'), \quad (1.35a)$$

$$\Sigma^{(A)}(t, t') = iE_{\text{Th}}\delta(t' - t), \quad (1.35b)$$

$$\Sigma^{(K)}(t, t') = -\frac{2E_{\text{Th}}}{\pi} \frac{1}{t - t'} \left\{ \alpha e^{-i[\psi(t) - \psi(t')]} + 1 - \alpha \right\}. \quad (1.35c)$$

In this equation E_{Th} is the Thouless energy, or inverse lifetime of an electron on the dot. It characterizes the time an electron spends on the dot before tunneling through one of the tunnel barriers. The phase $\psi(t)$ is the integral of the reservoir voltage $\psi(t) = \int_0^t dt' V(t')$ and $\alpha \in [0, 1]$ is a parameter that measures the relative coupling to the reservoirs. The value $\alpha = 0.5$ corresponds to equally strong couplings to both reservoirs while $\alpha = 0$ corresponds to the dot completely decoupled from the voltage-biased reservoir and $\alpha = 1$ corresponds to the dot entirely decoupled from the grounded reservoir.

We now solve Eq. (1.33), starting with the retarded component, i.e. the upper-left block, which reads explicitly

$$i\partial_t R_m(t, t') - [\varepsilon_m + \mu(t) - iE_{\text{Th}}] R_m(t, t') = \delta(t - t'), \quad (1.36a)$$

$$-i\partial_{t'} R_m(t, t') - [\varepsilon_m + \mu(t) - iE_{\text{Th}}] R_m(t, t') = \delta(t - t'). \quad (1.36b)$$

The retarded Green function $R_m(t, t')$ is defined as an anti-commutator of a creation and an annihilation operator. Since the creation and annihilation operators anti-commute at coinciding times, it follows that

$$\lim_{t-t' \rightarrow 0^+} R_m(t, t') = -i. \quad (1.37)$$

Furthermore, by definition, $R_m(t, t' > t) = 0$. Imposing these conditions leads to the unique solution

$$R_m(t, t') = -i\theta(t - t') e^{-E_{\text{Th}}(t-t')} e^{-i\varepsilon_m(t-t')} e^{-i[\phi(t) - \phi(t')]}, \quad (1.38)$$

where $\phi(t)$ is the integral of the chemical potential μ ; $\phi(t) = \int_0^t dt' \mu(t')$. We see that $R_m(t, t')$ decays exponentially as a function of $t - t'$ with lifetime E_{Th}^{-1} . To understand why this is, note that the two terms that constitute the retarded Green function have the following interpretation. Term $\langle a_m(t) a_m^\dagger(t') \rangle$ is the amplitude that an electron placed in level m

at time t' will still be there at time t . The term $\langle a_m^\dagger(t')a_m(t) \rangle$ is (the complex conjugate of) the amplitude that, if an electron is removed from level m at time t' , that level will still be empty at time t . When the dot is coupled to reservoirs, these can populate and depopulate the levels, causing the amplitudes represented by $R_m(t, t')$ to decay. Similarly, one finds that the advanced Green function is given by

$$A_m(t, t') = i\theta(t' - t)e^{-E_{\text{Th}}(t' - t)}e^{-i\varepsilon_m(t - t')}e^{-i[\phi(t) - \phi(t')]}.$$
 (1.39)

It remains for us to consider the Keldysh component of Eq. (1.33). We start by taking a brief look at the Keldysh component of the self-energy. It should be thought of as consisting of two contributions.

$$\Sigma^{(K)}(t, t')i = 2iE_{\text{Th}}[\alpha\sigma_V(t, t') + (1 - \alpha)\sigma_0(t, t')],$$
 (1.40a)

$$\sigma_V(t, t') = \frac{i}{\pi} \frac{e^{-i[\psi(t) - \psi(t')]} }{t - t'}.$$
 (1.40b)

The σ_0 contribution accounts for the coupling to the grounded reservoir. Note that it can be written as

$$\sigma_0(t, t') = \int \frac{d\varepsilon}{2\pi} e^{-i\varepsilon(t - t')} [1 - 2f(\varepsilon)],$$
 (1.41)

where $f_0(\varepsilon) = \theta(-\varepsilon)$ is the zero-temperature Fermi distribution of electrons in the grounded reservoir. The σ_V contribution similarly accounts for the presence of the reservoir with fluctuating bias voltage. Suppose for instance that the bias voltage V is constant. Then $\psi(t) = Vt$ and σ_V can be written as

$$\sigma_V(t, t') = \int \frac{d\varepsilon}{2\pi} e^{-i\varepsilon(t - t')} [1 - 2f(\varepsilon - V)].$$
 (1.42)

Again the zero-temperature Fermi distribution appears, this time with the Fermi energy appropriately shifted by V relative to the grounded reservoir.

The fact that the reservoir distribution functions only appear in the Keldysh component of the self-energy illustrates the following general principle. The retarded and advanced functions determine the effective one-body spectrum, while Keldysh functions determine how states are populated.

We now solve for the Keldysh component of the dot Green function. The upper right block of Eq. (1.33a) reads

$$[i\partial_t - \varepsilon_m - \mu(t) + iE_{\text{Th}}] K_m(t, t') = \int d\tilde{t} \Sigma^{(K)}(t, \tilde{t}) A_m(\tilde{t}, t').$$
 (1.43)

We invoke Eq. (1.36) which says that $R_m(t, t')$ is a resolvent for the differential operator appearing on the left of the above equation. Additionally we impose the initial condition that the system was in equilibrium before the time-dependent voltage was switched on. This implies the solution

$$K_m(t, t') = \int dt_1 dt_2 R_m(t, t_1) \Sigma^{(K)}(t_1, t_2) A_m(t_2, t'). \quad (1.44)$$

So, we have found $K_m(t, t')$. Are we done yet? Not quite. We still have to determine the chemical potential $\mu(t)$. In order to do this, we have Eq. (1.34) that relates $\mu(t)$ to the excess charge $Q(t)$ on the dot, which in turn is related to the Keldysh Green function at coinciding times. Putting these together, we have

$$Q(t) = -\frac{i}{2} \sum_m K_m(t, t) - K_m(0, 0). \quad (1.45)$$

We use the solution (Eq. 1.44) for K_m , with the explicit form of R_m and A_m substituted from Eqs. (1.38) and (1.39) to obtain

$$Q(t) = -\frac{i}{2} \sum_m \int_{-\infty}^0 dt_1 dt_2 e^{E_{\text{Th}}(t_1+t_2)} e^{-i\varepsilon_m(t_2-t_1)} \times \underbrace{\left\{ e^{[\phi(t+t_1)-\phi(t+t_2)]} \Sigma^{(K)}(t+t_1, t+t_2) - \Sigma^{(K)}(t_1, t_2) \right\}}_X, \quad (1.46)$$

where we have explicitly used the fact that $\mu(t)$ and hence $\phi(t)$ are zero for $t < 0$.

Let us assume that the mean level spacing $\delta\varepsilon$ is much smaller than the Thouless energy. Then we can replace

$$\sum_m e^{-i\varepsilon_m(t_2-t_1)} \rightarrow \delta(t_2-t_1) \frac{2\pi}{\delta\varepsilon}. \quad (1.47)$$

This is substituted into Eq. (1.46). The delta-function picks out the $t_2 \rightarrow t_1$ limit of the expression marked X . The factor $1/(t_1-t_2)$ in $\Sigma^{(K)}$ results in time-derivatives of ψ and ϕ , so that

$$\lim_{t_2 \rightarrow t_1} X = -\frac{2iE_{\text{Th}}}{\pi} [\mu(t) - \alpha V(t)]. \quad (1.48)$$

Using $\mu(t) = Q(t)/C$, we obtain an integral equation for $\mu(t)$ namely

$$\mu(t) = -\frac{2E_{\text{Th}}}{C\delta\varepsilon} \int_{-\infty}^t dt' e^{-2E_{\text{Th}}(t-t')} [\mu(t') - \alpha V(t')]. \quad (1.49)$$

This is converted into a differential equation by multiplying with $e^{2E_{\text{Th}}t}$ and taking a time-derivative. Finally we obtain

$$\frac{d}{dt}\mu(t) + \gamma\mu(t) = \Gamma V(t), \quad (1.50)$$

with $\Gamma = 2\alpha E_{\text{Th}}/C\delta\varepsilon$ and $\gamma = 2E_{\text{Th}}(1 + 1/C\delta\varepsilon)$. We solve this, and multiply by the capacitance, to obtain the charge on the dot as a function of time

$$Q(t) = \frac{2\alpha E_{\text{Th}}}{\delta\varepsilon} \int_0^t dt' e^{-\gamma(t-t')} V(t'). \quad (1.51)$$

It is instructive to compare this result to conclusions drawn from the following intuitive argument. We suppose that the quantum system we just analyzed is roughly equivalent to the an electric circuit where a central region with capacitance C is connected to leads 1 and 2, by means of resistors R_1 and R_2 respectively. Lead 2 is grounded while a time-dependent voltage $V(t)$ is applied to lead 1. The voltage of the central region is $\mu(t)$. It is related to the excess charge $Q(t)$ on the central region by $\mu(t) = Q(t)/C$. If I_1 is the current flowing from the lead 1 into the central region and I_2 is the current flowing from the central region into lead 2 then, Ohm's law says

$$I_1(t) = [V(t) - \mu(t)]/R_1, \quad I_2(t) = \mu(t)/R_2. \quad (1.52)$$

Charge conservation implies that $dQ(t)/dt = I_1(t) - I_2(t)$. Putting everything together, we obtain a differential equation for $\mu(t)$:

$$\frac{d}{dt}\mu(t) + \gamma_{\text{cl}}\mu(t) = \Gamma_{\text{cl}}V(t), \quad (1.53)$$

where $\gamma_{\text{cl}} = (R_1^{-1} + R_2^{-1})/C$ and $\Gamma_{\text{cl}} = 1/R_1C$.

This has the same form as the differential equation (1.50) that we obtained previously. However, if we compare the relaxation rates γ and γ_{cl} we note an important difference. In the limit $\delta\varepsilon C \gg 1$, the classical relaxation rate γ_{cl} goes to zero, while γ obtained with the Keldysh technique remains finite. There is a good reason for this. γ is the rate at which excess charge

relaxes into the reservoirs. The limit of large capacitance C corresponds to a situation where the Coulomb repulsion between electrons on the dot is weak. Even in this limit, excess charge on the dot should relax into the leads. The reason is that, due to the dynamics of non-interacting electrons on the dot, every once in a while, an electron tunnels into a reservoir. This process does not require that the escaping electron be “pushed off the dot” by the other electrons. The classical argument ignores the dynamics of non-interacting electrons, so that the only method for charge to leak off the dot is through Coulomb repulsion. Hence the classical and quantum results can only be expected to agree in the $\delta\varepsilon \ll C^{-1}$ limit. Beyond this limit, the quantum mechanical analysis, based on the Keldysh technique remains valid, while the classical argument breaks down.

We can relate the resistances R_1 and R_2 of the classical theory to the parameters of the quantum theory in the $\delta\varepsilon \ll C^{-1}$ limit. One obtains

$$R_1^{-1} = 2\alpha \frac{E_{\text{Th}} e^2}{\delta\varepsilon \hbar}, \quad R_2^{-1} = 2(1 - \alpha) \frac{E_{\text{Th}} e^2}{\delta\varepsilon \hbar}, \quad (1.54)$$

where e^2/\hbar reinstates the units that were dropped in the microscopic analysis. The quantity $E_{\text{Th}}/\delta\varepsilon$ is known to characterize the conductance of a coherent conductor, and is called the dimensionless Thouless conductance.

Bibliography

- [1] R. Landauer, IBM J. Res. Dev. **1**, 223 (1957); Philos. Mag. **21**, 863 (1970).
- [2] M. Büttiker, IBM J. Res. Dev. **32**, 63 (1988).
- [3] C. W. J. Beenakker and H. van Houten, Solid State Phys. **44**, 1 (1991).
- [4] H. van Houten, C. W. J. Beenakker, J. G. Williamson, M. E. I. Broekaart, P. H. M. van Loosdrecht, B. J. van Wees, J. E. Mooij, C. T. Foxon and J. J. Harris, Phys. Rev. B **39**, 8556 (1989).
- [5] Ya. M. Blanter and M. Büttiker, Phys. Rep. **336**, 1 (2000).
- [6] C. W. J. Beenakker and C. Schönberger, Phys. Today **56** (5), 37 (2003).
- [7] L. V. Keldysh, Zh. Eksp. Teor. Fiz. **47**, 1515 (1964); [Sov. Phys. JETP **20**, 1018 (1965)].
- [8] R. P. Feynman and F. L. Vernon Jr., Ann. Phys. (N. Y.) **24**, 118 (1963).
- [9] J. Schwinger, J. Math. Phys. **2**, 407 (1961).
- [10] J. Rammer and H. Smith, Rev. Mod. Phys. **58**, 323 (1986).
- [11] E. M. Lifshitz and L. P. Pitaevskii, *Physical Kinetics*, (Pergamon Press, Oxford, 1981).
- [12] A. Kamenev, arXiv:cond-mat/0412296.
- [13] H. Haug and A. -P. Jauho, *Quantum Kinetics in Transport and Optics of Semiconductors*, (Springer Verlag, Berlin, 1998).

-
- [14] A. A. Abrikosov, L. P. Gorkov and I. E. Dzyaloshinski, *Methods of Quantum Field Theory in Statistical Physics*, (Prentice-Hall, New Jersey, 1963).
- [15] J. W. Negele and H. Orland, *Quantum Many-Particle Systems*, (Addison-Wesley, California, 1987).
- [16] M. Kindermann, Yu. V. Nazarov and C. W. J. Beenakker, Phys. Rev. Lett. **90**, 2468051 (2003).
- [17] M. Kindermann, Yu. V. Nazarov and C. W. J. Beenakker, Phys. Rev. B **69**, 035336 (2004).
- [18] G.-L. Ingold and Yu. V. Nazarov, in *Single Charge Tunneling*, edited by H. Grabert and M. H. Devoret, NATO ASI Series B294 (Plenum, New York, 1992).
- [19] G. Schön, Phys. Rev. B **32**, 4469 (1986).
- [20] M. H. Devoret, D. Esteve, H. Grabert, G.-L. Ingold, H. Pothier and C. Urbina, Phys. Rev. Lett. **64**, 1824 (1990).
- [21] S. M. Girvin, L. I. Glazman, M. Jonson, D. R. Penn and M. D. Stiles, Phys. Rev. Lett. **64**, 3183 (1990).
- [22] A. Levy Yeyati, A. Martin-Rodero, D. Esteve and C. Urbina, Phys. Rev. Lett. **87**, 046802 (2001).
- [23] A. O. Caldeira and A. J. Leggett, Phys. Rev. Lett. **46**, 211 (1981).
- [24] A. O. Caldeira and A. J. Leggett, Ann. Phys. (N. Y.) **149**, 374 (1983).
- [25] Yu. V. Nazarov and D. V. Averin, Physica B **162**, 309 (1990).
- [26] Yu. V. Nazarov, Phys. Rev. B **43**, 6220 (1991).
- [27] J. J. Sakurai, *Advanced Quantum Mechanics*, (Addison-Wesley, Massachusetts, 1967).
- [28] P. R. Wallace, Phys. Rev. **71**, 622 (1947).
- [29] J. W. McClure, Phys. Rev. **104**, 666 (1956).
- [30] G. W. Semenoﬀ, Phys. Rev. Lett. **53**, 2449 (1984).

-
- [31] D. P. DiVincenzo and E. J. Mele, *Phys. Rev. B* **29**, 1685 (1984).
- [32] F. D. M. Haldane, *Phys. Rev. Lett.* **61**, 2015 (1988).
- [33] K. S. Novoselov, A. K. Geim, S. V. Morozov, D. Jiang, Y. Zhang, S. V. Dubonos, I. V. Grigorieva and A. A. Firsov, *Science* **306**, 666 (2004).
- [34] K. S. Novoselov, A. K. Geim, S. V. Morozov, D. Jiang, M. I. Katsnelson, I. V. Grigorieva, S. V. Dubonos and A. A. Firsov, *Nature* **438**, 197 (2005).
- [35] Y. Zhang, Y.-W. Tan, H. L. Stormer and P. Kim, *Nature* **438**, 201 (2005).
- [36] A. H. Castro Neto, F. Guinea and N. M. R. Peres, *Phys. World* **19**, 33 (2006).
- [37] A. K. Geim and K. S. Novoselov, *Nature Mat.* **6**, 183 (2007).
- [38] A. K. Geim and A. H. MacDonald, *Phys. Today* **60** (8), 35 (2007).
- [39] M. I. Katsnelson, *Materials Today* **10**, 20 (2007).
- [40] A. K. Geim and P. Kim, *Scientific American* **298** (4), 90 (2008).
- [41] A. H. Castro Neto, F. Guinea, N. M. R. Peres, K. S. Novoselov and A. K. Geim, arXiv:0709.1163 (2007).
- [42] V. P. Gusynin, S. G. Sharapov and J. P. Carbotte, *Int. J. Mod. Phys. B* **21**, 4611 (2007).
- [43] M. I. Katsnelson and K. S. Novoselov, *Solid State Comm.* **143**, 3 (2007).
- [44] C. W. J. Beenakker, arXiv:0710.3848 (2007).
- [45] L. Brey and H. A. Fertig, *Phys. Rev. B* **73**, 195408 (2006).
- [46] V. V. Cheianov and V. I. Fal'ko, *Phys. Rev. B* **74**, 041403(R) (2006).
- [47] M. I. Katsnelson, K. S. Novoselov and A. K. Geim, *Nature Phys.* **2**, 620 (2006).

-
- [48] T. Ando, T. Nakanishi and R. Saito, *J. Phys. Soc. Japan* **67**, 2857 (1998).
- [49] M. Titov, *Europhys. Lett.* **79**, 17004 (2007).
- [50] A. Rycerz, J. Tworzydło and C. W. J. Beenakker, *Europhys. Lett.* **79**, 57003 (2007).
- [51] J. H. Bardarson, J. Tworzydło, P. W. Brouwer and C. W. J. Beenakker, *Phys. Rev. Lett.* **99**, 106801 (2007).
- [52] K. Nomura, M. Koshino and S. Ryu, *Phys. Rev. Lett.* **99**, 146806 (2007).
- [53] P. San-Jose, E. Prada and D. S. Golubev, *Phys. Rev. B* **76**, 195445 (2007).
- [54] E. McCann and V. Fal'ko, *Phys. Rev. Lett.* **96**, 086805 (2006).
- [55] J. Nilsson, A. H. Castro Neto, F. Guinea and N. M. R. Peres, *Phys. Rev. Lett.* **97**, 266801 (2006).
- [56] J. Nilsson, A. H. Castro Neto, F. Guinea and N. M. R. Peres, *Phys. Rev. B* **93**, 214418 (2006).
- [57] J. Cserti, A. Csordás and G. Dávid, *Phys. Rev. Lett.* **99**, 066802 (2007)
- [58] A. G. Moghaddam and M. Zareyan, arXiv:0804.2748 (2008).
- [59] A. Kamenev and A. Andreev, *Phys. Rev. B* **60**, 2218 (1999).
- [60] M. V. Feigel'man, A. I. Larkin and M. A. Skvortsov, *Phys. Rev. B* **61**, 12361 (2000).
- [61] M. Kindermann and Yu. V. Nazarov, *Phys. Rev. Lett.* **91**, 136802 (2003).
- [62] J. Tworzydło, B. Trauzettel, M. Titov, A. Rycerz and C. W. J. Beenakker, *Phys. Rev. Lett.* **96**, 246802 (2006).
- [63] J. T. Chalker and P. D. Coddington, *J. Phys. C* **21**, 2665 (1988).
- [64] C.-M. Ho and J. T. Chalker, *Phys. Rev. B* **54**, 8708 (1996).

Chapter 2

The Keldysh action of a time-dependent scatterer

2.1 Introduction

The pioneering works of Landauer [1] and Büttiker [2] lay the foundations for what is now known as the scattering approach to electron transport. The basic tenet is that a coherent conductor is characterized by its scattering matrix. More precisely the transmission matrix defines a set of transparencies for the various channels or modes in which the electrons propagate through the conductor. As a consequence, conductance is the sum over transmission probabilities. Subsequently, it was discovered that the same transmission probabilities fully determine the current noise, also outside equilibrium, where the fluctuation-dissipation theorem does not hold [3].

Indeed, as the theory of Full Counting Statistics [4, 5] later revealed, the complete probability distribution for outcomes of a current measurement is entirely characterized by the transmission probabilities of the conductor. The fact that the scattering formalism gives such an elegant and complete description inspired some to revisit established results. Thus for instance interacting problems such as the Fermi Edge Singularity [6, 7] were recast in the language of the scattering approach [8, 9, 10, 11]. The scattering approach has further been employed successfully in problems where a coherent conductor interacts with other elements, including, but not restricted to, measuring devices and an electromagnetic environment [12, 13, 14, 15]. It is also widely applied to study transport in mesoscopic

superconductors [16].

Many of these more advanced applications are unified through a method developed by Feynman and Vernon for characterizing the effect of one quantum system on another when they are coupled [17]. The work of Feynman and Vernon dealt with the effect of a bath of oscillators coupled to a quantum system. It introduced the concept of a time-contour describing propagation first forwards then backwards in time. By using the path-integral formalism, it was possible to characterize the bath by an “influence functional” that did not depend on the system that the bath was coupled to. This functional was treated non-perturbatively. A related development was due to Keldysh [18]. While being a perturbative diagrammatic technique, it allowed for the treatment of general systems and shared the idea of a forward and backward time-contour with Feynman and Vernon.

In general, the Feynman-Vernon method expresses the dynamics of a complex system in the form of an integral over a few fields $\chi(t)$. Each part of the system contributes to the integrand by a corresponding influence functional $\mathcal{Z}[\chi]$, or, synonymously, a Keldysh action $\mathcal{A}[\chi] = \ln \mathcal{Z}[\chi]$. Thus the Keldysh action of a general scatterer can be used as a building block. In this way the action of a complicated nanostructure consisting of a network of scatterers can be constructed. As in the case of classical electronics, a simple set of rules, applied at the nodes of the network, suffice to describe the behavior of the whole network [19, 20].

The essential element of the approach is that the fields χ take different values on the forward/backward parts of the time-contour. One writes this as $\chi_{\pm}(t)$, where $+$ ($-$) corresponds to the forward (backward) part of the contour. The Keldysh action for a given sub-system is evaluated as the full non-linear response of the sub-system to the fields $\chi_{\pm}(t)$. (See Eq. 2.6 below for the precise mathematical definition.)

Applications involving the scattering approach require both the notion of the non-perturbative influence functional and the generality of Keldysh’s formalism. Until now, the combination of the Feynman-Vernon method with the scattering approach was done on a case-specific basis: Only those elements relevant to the particular application under consideration were developed. In this paper we unify previous developments by deriving general formulas for the Keldysh action of a general scatterer connected to charge reservoirs.

The time-dependent fields $\chi_+(t)$ and $\chi_-(t)$ parametrize two Hamiltoni-

ans $\mathcal{H}_+(t)$ and $\mathcal{H}_-(t)$ that governs forward and backward evolution in time respectively. Since we are in the framework of the scattering approach, these field-dependent Hamiltonians are not the most natural objects to work with. Rather, depending on where the fields couple to the system, it is natural to incorporate their effect either in the scattering matrix of the conductor, or in the Green functions of the electrons in the reservoirs: The fields affecting the scattering potential inside the scatterer are incorporated in a time-dependent scattering matrix. Since the fields χ_{\pm} for forward and backward evolution are different, the scattering matrices for forward and backward evolution differ. The effect of the fields perturbing the electrons far from the scatterer is incorporated in the time-dependent Green functions of the electrons in distant reservoirs. A bias voltage applied across a conductor can conveniently be ascribed to either Green functions of the reservoirs or to a phase factor of the scattering matrix. The same holds for the counting fields encountered in the theory of full counting statistics. There are however situations where our hand is forced. For instance, in the example of the Fermi-edge singularity, that we discuss in Sec. 2.6, the time-dependent fields have to be incorporated in the scattering matrices.

Previous studies of the Keldysh action concentrated on situations where the fields χ_{\pm} could be incorporated in the reservoir Green functions. These studies therefore assumed stationary, contour-independent scattering matrices while allowing for a time-dependence and/or time-contour dependence of the electron Green functions. Early works (Refs. [21] and [22]) used an action of this type to analyze Coulomb blockade phenomena. Later, the same action was understood in the wider context of arbitrary Green's functions [19, 23]. In this form it has been used to treat problems involving for example interactions and superconductivity. The action employed in these studies corresponds to Eq. 2.4 and can readily be derived in the context of non-linear sigma-model of disordered metals [24].

The main innovation of the present work is to generalize the action to contour- and time-dependent scattering matrices. The only assumption we make is that scattering is instantaneous: We do not treat the delay time an electron spends inside the scattering region realistically.

The resulting scattering matrices associated with forward and backward evolution are combined into one big matrix \hat{s} . It has a kernel $s(\alpha; c, c'; t)\delta_{\alpha, \alpha'}\delta(t - t')$ where the Keldysh indices $\alpha, \alpha' \in \{+, -\}$ refer to the forward and backward part of the time contour, c and c' are integers that refer to channel space, and t, t' are time indices that lie on

the real line. The forward (backward) scattering matrix $\hat{s}_{+(-)}$ with kernel $s(\alpha = +(-); c, c'; t)$ obeys the usual unitarity condition $\hat{s}_{\pm}^{\dagger} \hat{s}_{\pm} = 1$.

With the aide of these preliminary definitions, our main result is summarized by a formula for the Keldysh action.

$$\mathcal{A}[\hat{s}] = \text{Tr} \ln \left[\frac{1 + \hat{G}}{2} + \hat{s} \frac{1 - \hat{G}}{2} \right] - \text{Tr} \ln \hat{s}_-. \quad (2.1)$$

In this formula, \hat{G} is the Keldysh Green function characterizing the reservoirs connected to the scatterer [25]. It is to be viewed as an operator with kernel $G(\alpha, \alpha'; c, t, t') \delta_{c,c'}$ where indices carry the same meaning as in the definition of \hat{s} . This formula is completely general.

1. It holds for time dependent scattering matrices that differ on the forward and backward time contour.
2. It holds for multi-terminal devices with more than two reservoirs.
3. It holds for devices such as Hall bars where particles in a single chiral channel enter and leave the conductor at different reservoirs.
4. It holds when reservoirs cannot be characterized by stationary filling factors. Reservoirs may be superconducting, or contain ‘‘counting fields’’ coupling them to a dynamical electromagnetic environment or a measuring device.

When the reservoirs can indeed be characterized by filling factors $\hat{f}(\varepsilon)$, the Keldysh structure can explicitly be traced out to yield

$$\mathcal{A}[\hat{s}_+, \hat{s}_-] = \text{Tr} \ln \left[\hat{s}_- (1 - \hat{f}) + \hat{s}_+ \hat{f} \right] - \text{Tr} \ln \hat{s}_-. \quad (2.2)$$

In this expression operators retain channel structure and time structure. In ‘‘time’’ representation, \hat{f} is the Fourier transform to time of the reservoir filling factors, and as such has a kernel $f(c; t, t') \delta_{c,c'}$ diagonal in channel space and depending on two times. In stationary limit, this formula immediately reduces to the Levitov formula for low-frequency Full Counting Statistics (FCS) [5].

Another formula that can be derived from Eq. (2.1) is valid for two terminal devices and a stationary, time-contour-independent scattering matrix but allows for arbitrary Green functions in the two terminals. Each

terminal may still be connected to the scatterer by an arbitrary number of channels. We denote the two terminals left (L) and right (R). In this case the reservoir Green function has the form

$$\hat{G} = \begin{pmatrix} \check{G}_L & 0 \\ 0 & \check{G}_R \end{pmatrix}_{\text{channel space}}, \quad (2.3)$$

where $\check{G}_{L(R)}$ have no further channel space structure. Matrix structure in Keldysh and time indices (indicated by a check sign) is now retained in the trace, but the channel structure is traced out. Thus is obtained

$$\mathcal{A}[\chi_{\pm}] = \frac{1}{2} \sum_n \text{Tr} \ln \left[1 + T_n \frac{\{\check{G}_L[\chi_{\pm}], \check{G}_R[\chi_{\pm}]\} - 2}{4} \right]. \quad (2.4)$$

In this expression, the field dependence χ_{\pm} is shifted entirely to the Keldysh Green functions \check{G}_L and \check{G}_R of the left and right reservoirs. This formula makes it explicit that the conductor is completely characterized by its transmission eigenvalues T_n .

The structure of the chapter is as follows. After making the necessary definitions, we derive Eq. (2.1) from a model Hamiltonian. The derivation makes use of contour ordered Green functions and the Keldysh technique. Subsequently, we derive the special cases of Eq. (2.2) and Eq. (2.4).

We conclude by applying the formulas to several generic set-ups, and verify that results agree with the existing literature. Particularly, we explain in detail how the present work is connected to the theory of Full Counting Statistics and to the scattering theory of the Fermi Edge Singularity.

2.2 Derivation

We consider a general scatterer connecting a set of charge reservoirs. We allow the scatterer to be time-dependent. A sufficient theoretical description is provided by a set of transport channels interrupted by a potential that causes inter-channel scattering. We consider the regime where the scattering matrix is energy-independent in the transport energy window. Since transport is purely determined by the scattering matrix, all models that produce the same scattering matrix give identical results. Regardless of actual microscopic detail, we may therefore conveniently take the

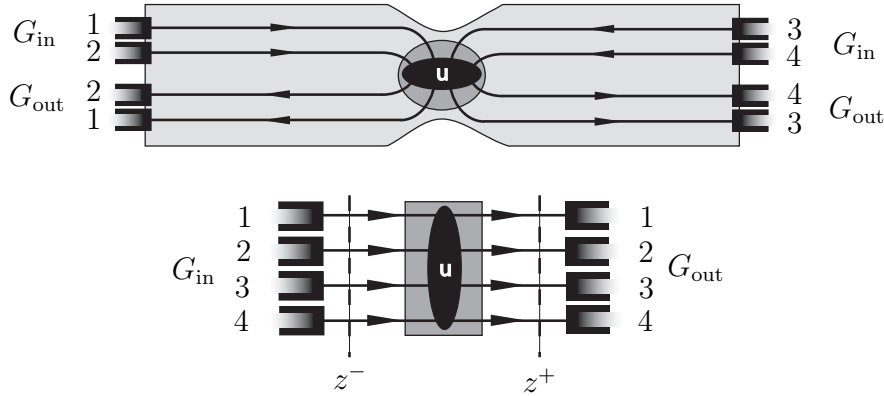


Figure 2.1. We consider a general scatterer connected to reservoirs. The top figure is a diagram of one possible physical realization of a scatterer. Channels carry electrons towards and away from a scattering region (shaded dark gray) where inter-channel scattering takes place. Reservoirs are characterized by Keldysh Green functions $G_{\text{in(out)}}$. These Green functions also carry a channel index, in order to account for, among other things, voltage biasing. In setups such as the Quantum Hall experiment where there is a Hall voltage, G_{in} will differ from G_{out} , while in an ordinary QPC, the two will be identical. The bottom figure shows how the physical setup is represented in our model. Channels are unfolded so that all electrons enter at z^- and leave at z^+ .

Hamiltonian of the scatterer to be

$$\mathcal{H} = v_F \sum_{m,n} \int dz \psi_m^\dagger(z) \{-i\delta_{m,n}\partial_z + u_{m,n}(z)\} \psi_n(z) + \mathcal{H}_{\text{res}} + \mathcal{H}_{\text{T}}, \quad (2.5)$$

where \mathcal{H}_{res} represents the reservoirs, and \mathcal{H}_{T} takes account of tunneling between the conductor and the reservoirs. The scattering region and the reservoirs are spatially separated. This means that the scattering potential $u_{mn}(z)$ is non-zero only in a region $z^- < z < z^+$ while tunneling between the reservoirs and the conductor only takes place outside this region. Note that in our model, scattering channels have been “unfolded”, so that instead of working with a channel that confines particles in the interval $(-\infty, 0]$ and allowing for propagation both in the positive and negative directions, we equivalently work with channels in which particles propagate along $(-\infty, \infty)$, but only in the positive direction. Hence, to make contact with most physical setups, we consider $-z$ and z to refer to the same physical position in a channel, but opposite propagation directions.

We consider the generating functional

$$\begin{aligned} \mathcal{Z} &= e^{\mathcal{A}} \\ &= \text{Tr} \left[\mathcal{T}^+ \exp \left\{ -i \int_{t_0}^{t_1} dt \mathcal{H}^+(t) \right\} \rho_0 \mathcal{T}^- \exp \left\{ i \int_{t_0}^{t_1} dt \mathcal{H}^-(t) \right\} \right], \end{aligned} \quad (2.6)$$

in which \mathcal{H}^\pm is obtained from \mathcal{H} by replacing $u_{mn}(z)$ with arbitrary time-dependent functions $u_{mn}^\pm(z, t)$. In this expression \mathcal{T}^+ exp and \mathcal{T}^- exp respectively refer to time-ordered (i.e. largest time to the left) and anti-time-ordered (i.e. largest time to the right) exponentials. In the language of Feynman and Vernon [17] this is known as the influence functional. It gives a complete characterization of the effect that the electrons in the scatterer have on any quantum system that they interact with. Furthermore, the functional \mathcal{Z} generates expectation values of time-ordered products of operators as follows. Let Q be an operator

$$Q = \sum_{mn} \int_{z^-}^{z^+} dz \psi_m^\dagger(z) q_{mn}(z) \psi_n(z). \quad (2.7)$$

Choose $u_{mn}^\pm(z, t) = u_{mn}(z) + \chi_\pm(t) q_{mn}(z)$. Then

$$\begin{aligned} &\left\langle \mathcal{T}^- \left(\prod_{j=1}^M Q(t_j) \right) \mathcal{T}^+ \left(\prod_{k=1}^N Q(t'_k) \right) \right\rangle \\ &= \prod_{j=1}^M \left(-i \frac{\delta}{\delta \chi^-(t_j)} \right) \prod_{k=1}^N \left(i \frac{\delta}{\delta \chi^+(t'_k)} \right) \mathcal{Z}[\chi] \Big|_{\chi=0}. \end{aligned} \quad (2.8)$$

By merging the power of the Keldysh formalism of contour-ordered Green functions with that of the Landauer scattering formalism for quantum transport, we obtain an expression for \mathcal{Z} in terms of the Keldysh Green functions in the reservoirs and the time dependent scattering matrices associated with $\hat{u}^\pm(z, t)$.

The argument will proceed in the following steps:

1. Firstly we introduce the key object that enables a systematic analysis of \mathcal{Z} , namely the single particle Green function g of the conductor. We state the equations of motion that g obeys.
2. We define the Keldysh action $\mathcal{A} = \ln \mathcal{Z}$, and consider its variation $\delta \mathcal{A}$. We discover that $\delta \mathcal{A}$ can be expressed in terms of g .

3. We therefore determine g inside the scattering region in terms of the scattering matrix of the conductor and its value at the edges of the scattering region, where the reservoirs impose boundary conditions.
4. This allows us to express the variation of the action in terms of the reservoir Green functions $G_{\text{in(out)}}$ and the scattering matrix s of the conductor.
5. The variation $\delta\mathcal{A}$ is then integrated to find the action \mathcal{A} and the generating functional \mathcal{Z} .

2.2.1 Preliminaries: Definition of the Green function

The first step is to move from the Schrödinger picture to the Heisenberg picture. To shorten notation we define two time-evolution operators:

$$\mathcal{U}_{\pm}(t_f, t_i) = \mathcal{T}^{\pm} \exp \left\{ -i \int_{t_i}^{t_f} dt' \mathcal{H}^{\pm}(t') \right\}. \quad (2.9)$$

Associated with every Schrödinger picture operator we define two Heisenberg operators, one corresponding to evolution with each of the two Hamiltonians \mathcal{H}^{\pm} .

$$Q_{\pm}(t) = \mathcal{U}_{\pm}(t_f, t_i)^{\dagger} Q \mathcal{U}_{\pm}(t_f, t_i). \quad (2.10)$$

In order to have the tools of the Keldysh formalism at our disposal, we need to define four Green functions

$$\begin{aligned} g_{m,n}^{++}(z, t; z', t') &= -e^{\mathcal{A}} \text{Tr} \left[\mathcal{U}^+(t_1, t_0) \mathcal{T}^+ \left(\psi_{n+}^{\dagger}(z', t') \psi_{m+}(z, t) \right) \rho_0 \left(\mathcal{U}^-(t_1, t_0) \right)^{\dagger} \right], \\ g_{m,n}^{+-}(z, t; z', t') &= e^{\mathcal{A}} \text{Tr} \left[\mathcal{U}^+(t_1, t_0) \psi_{m+}(z, t) \rho_0 \psi_{n-}^{\dagger}(z', t') \left(\mathcal{U}^-(t_1, t_0) \right)^{\dagger} \right], \\ g_{m,n}^{-+}(z, t; z', t') &= e^{\mathcal{A}} \text{Tr} \left[\mathcal{U}^+(t_1, t_0) \psi_{n+}^{\dagger}(z', t') \rho_0 \psi_{m-}(z, t) \left(\mathcal{U}^-(t_1, t_0) \right)^{\dagger} \right], \\ g_{m,n}^{--}(z, t; z', t') &= e^{\mathcal{A}} \text{Tr} \left[\mathcal{U}^+(t_1, t_0) \rho_0 \mathcal{T}^- \left(\psi_{n-}^{\dagger}(z', t') \psi_{m-}(z, t) \right) \left(\mathcal{U}^-(t_1, t_0) \right)^{\dagger} \right]. \end{aligned} \quad (2.11)$$

Here the symbol \mathcal{T}^+ orders operators with larger time arguments to the left. If permutation is required to obtain the time-ordered form, the product is multiplied with $(-1)^n$ where n is the parity of the permutation. Similarly, \mathcal{T}^- anti-time-orders with the same permutation parity convention.

The Green functions can be grouped into a matrix in Keldysh space

$$g_{m,n}(z, t; z', t') = \begin{pmatrix} g_{m,n}^{++}(z, t; z', t') & g_{m,n}^{+-}(z, t; z', t') \\ g_{m,n}^{-+}(z, t; z', t') & g_{m,n}^{--}(z, t; z', t') \end{pmatrix}. \quad (2.12)$$

Notation can be further shortened by incorporating channel-indices into the matrix structure of the Green function, thereby defining an object $\bar{g}(z, t; z', t')$. The element of \bar{g} that is located on row m and column n , is the 2×2 matrix $g_{m,n}$.

The Green function satisfies the equation of motion

$$\begin{aligned} & \{i\partial_t + v_F i\partial_z - v_F \bar{u}(z, t)\} \bar{g}(z, t; z', t') \\ & - \int dt'' \Sigma(z; t - t'') \bar{g}(z, t''; z', t') = \delta(t - t') \delta(z - z') \bar{1}. \end{aligned} \quad (2.13)$$

The delta-functions on the right of Eq. (2.13) encode the fact that due to time-ordering g_{mn}^{++} and g_{mn}^{--} have a step-structure

$$\frac{1}{v_F} \theta(z - z') \delta(t - t' - \frac{z - z'}{v_F}) \delta_{mn} + F(z, t; z', t'), \quad (2.14)$$

where F is continuous in all its arguments. The self-energy

$$\Sigma(z; \tau) = -i \frac{\bar{G}_{\text{in}}(\tau)}{2\tau_c} \theta(z^- - z) - i \frac{\bar{G}_{\text{out}}(\tau)}{2\tau_c} \theta(z - z^+) \quad (2.15)$$

results from the reservoirs and determines how the scattering channels are filled. It is a matrix in Keldysh space. The time τ_c is the characteristic time correlations survive in the region of the conductor that is connected to the reservoirs, before the reservoirs scramble them. $\bar{G}_{\text{in(out)}}(\tau)$ is the reservoir Green functions where electrons enter (leave) the scattering region, summed over reservoir levels and normalized to be dimensionless. This form of the self-energy can be derived from the following model for the reservoirs: We imagine every point z in a channel m outside (z^-, z^+) to exchange electrons with an independent Fermion bath with a constant

density of states ν . The terms \mathcal{H}_{res} and \mathcal{H}_{T} are explicitly

$$\begin{aligned}\mathcal{H}_{\text{res}} &= \sum_m \int dE \nu \int_{\mathcal{I}} dz E a_m^\dagger(E, z) a_m(E, z), \\ \mathcal{H}_{\text{T}} &= \sum_m c_m \int dE \nu \int_{\mathcal{I}} dz \psi_m^\dagger(z) a_m(E, z) + a_m^\dagger(E, z) \psi_m(z),\end{aligned}\tag{2.16}$$

where the tunneling amplitude c_m characterizes the coupling between the reservoir and channel m . The interval $\mathcal{I} = (-\infty, z_-) \cup (z_+, \infty)$ of integration excludes the scattering region. More general reservoir models need not be considered, since, as we shall see shortly, the effect of the reservoirs is contained entirely in a boundary conditions on the Green function \bar{g} inside the scatterer. This boundary condition does not depend on microscopic detail, but only on the reservoir Green functions $\bar{G}_{\text{in(out)}}$.

We do not need to know the explicit form of the reservoir Green functions yet. Rather the argument below relies exclusively on the property of $\bar{G}_{\text{in(out)}}$ that it squares to unity [25]:

$$\int dt'' \bar{G}(t - t'')_{\text{in(out)}} \bar{G}(t'' - t')_{\text{in(out)}} = \delta(t - t') \bar{1}.\tag{2.17}$$

A differential equation similar to Eq. (2.13) holds for \bar{g}^\dagger .

2.2.2 Varying the action

We are now ready to attack the generating functional \mathcal{Z} . For our purposes, it is most convenient to consider $\mathcal{A} = \ln \mathcal{Z}$. We will call this object the action. Our strategy is as follows: We will obtain an expression for the variation $\delta\mathcal{A}$ resulting from a variation $\hat{u}(z, t) \rightarrow \hat{u}(z, t) + \delta\hat{u}(z, t)$ of the scattering potentials. This expression will be in terms of the reservoir filling factors \hat{f} and the scattering matrices associated with $\hat{u}(z, t)$. We then integrate to find \mathcal{A} .

We start by writing

$$\begin{aligned}\delta\mathcal{A} &= -iv_F e^{\mathcal{A}} \sum_{m,n} \int_{t_0}^{t_1} dt \int dz \left(\delta u_{n,m}^+(z, t) \left\langle \psi_m^\dagger(z) \psi_n(z) \right\rangle_+(t) \right. \\ &\quad \left. - \delta u_{n,m}^-(z, t) \left\langle \psi_m^\dagger(z) \psi_n(z) \right\rangle_-(t) \right),\end{aligned}\tag{2.18}$$

where

$$\begin{aligned}
\left\langle \psi_m^\dagger(z) \psi_n(z) \right\rangle_+ (t) &= \text{Tr} \left[\mathcal{T}^+ \exp \left\{ -i \int_t^{t_1} dt' \mathcal{H}^+(t') \right\} \psi_m^\dagger(z) \psi_n(z) \right. \\
&\times \mathcal{T}^+ \exp \left\{ -i \int_{t_0}^t dt' \mathcal{H}^+(t') \right\} \rho_0 \mathcal{T}^- \exp \left\{ i \int_{t_0}^{t_1} dt' \mathcal{H}^-(t') \right\} \left. \right], \\
\left\langle \psi_m^\dagger(z) \psi_n(z) \right\rangle_- (t) &= \text{Tr} \left[\mathcal{T}^+ \exp \left\{ -i \int_{t_0}^{t_1} dt' \mathcal{H}^+(t') \right\} \rho_0 \right. \\
&\times \mathcal{T}^- \exp \left\{ i \int_{t_0}^t dt' \mathcal{H}^-(t') \right\} \psi_m^\dagger(z) \psi_n(z) \mathcal{T}^- \exp \left\{ -i \int_t^{t_1} dt' \mathcal{H}^-(t') \right\} \left. \right].
\end{aligned} \tag{2.19}$$

2.2.3 Expressing the variation of the action in terms of the Green function

In terms of the defined Green functions, the variation $\delta\mathcal{A}$ becomes

$$\begin{aligned}
\delta\mathcal{A} &= iv_F \sum_{m,n} \int_{t_0}^{t_1} dt \int dz \left(\delta u_{n,m}^+(z,t) g_{m,n}^{++}(z, t - 0^+; z, t) \right. \\
&\quad \left. + \delta u_{n,m}^-(z,t) g_{m,n}^{--}(z, t + 0^+; z, t) \right) \\
&= iv_F \int_{t_0}^{t_1} dt \int dz \text{Tr} \left[\delta \bar{u}(z,t) \bar{g}(z, t + 0^k; z, t) \right].
\end{aligned} \tag{2.20}$$

The object $\delta \bar{u}$ is constructed by combining the channel and Keldysh indices of the variation of the potential. The trace is over both Keldysh and channel indices. The symbol 0^k refers to the regularization explicitly indicated in the first line, i.e. the first time argument of $g^{++}(z, t - 0^+; z, t)$ is evaluated an infinitesimal time $0^+ > 0$ *before* the second argument, while in $g^{--}(z, t + 0^-; z, t)$, the first time argument is evaluated an infinitesimal time 0^+ *after* the second. This is done so that the time ordering (anti-time ordering) operations give the order of creation and annihilation operators required in Eq. (2.18).

It proves very inconvenient to deal with the 0^k regularization of Eq. (2.20). It is preferable to have the first time arguments of both g^{++} and g^{--} evaluated an infinitesimal time 0^+ *before* the second. Taking into

account the step-structure of \hat{g}^{++} we have

$$\bar{g}(z, t+0^k; z' t') = \bar{g}(z, t-0^+; z', t') + \frac{1}{v_F} \delta(t-t' - \frac{z-z'}{v_F}) \hat{1} \left(\frac{1-\check{\tau}_3}{2} \right). \quad (2.21)$$

Here $\check{\tau}_3$ is the third Pauli matrix $\begin{pmatrix} 1 & 0 \\ 0 & -1 \end{pmatrix}$ acting in Keldysh space. The equations of motion allow us to relate $\bar{g}(z, t-0^+; z', t')$ for points z and z' inside the scattering region where \bar{u} is non-zero, to the value of \bar{g} at z^- where electrons enter the scatterer. For $z \leq z'$ and $t \leq t'$, the equations of motion give

$$\begin{aligned} & \bar{g}(z, t + \frac{z-z^-}{v_F} - 0^+; z', t + \frac{z'-z^-}{v_F}) \\ &= \bar{s}(z, t) \bar{g}(z^-, t-0^+; z'^-, t') \bar{s}^\dagger(z', t'), \end{aligned} \quad (2.22)$$

where

$$\bar{s}(z, t) = \mathcal{Z} \exp \left\{ -i \int_{z^-}^z dz'' \bar{u}(z'', t + \frac{z''-z^-}{v_F}) \right\}. \quad (2.23)$$

The symbol \mathcal{Z} indicates that the exponent is ordered along the z -axis, with the largest co-ordinate in the integrand to the left. Note that the potential \bar{u} at position z is evaluated at the time instant $t + (z-z^-)/v_F$ that an electron entering the scattering region at time t reaches z . Often the time-dependence of the potential is slow on the time-scale $(z^+ - z^-)/v_F$ representing the time a transported electron spends in the scattering region and $\bar{u}(z, t + \frac{z-z^-}{v_F})$ can be replaced with $\bar{u}(z, t)$. This is however not required for the analysis that follows to be valid.

Substitution into Eq. (2.24) yields

$$\begin{aligned} \delta A = v_F \int dt \text{Tr} [\bar{w}(t) g(z^-, t-0^+; z^-, t)] \\ - \int dt \lim_{t' \rightarrow t} \delta(t-t') \text{Tr} \left[\bar{w}(t) \hat{1} \left(\frac{1-\check{\tau}_3}{2} \right) \right]. \end{aligned} \quad (2.24)$$

with

$$\begin{aligned} \bar{w}(t) &= -i \int_{z^-}^{z^+} dz \bar{s}^\dagger(z, t) \delta \bar{u}(z, t + \frac{z-z^-}{v_F}) \bar{s}(z, t) \\ &= \bar{s}^\dagger(t) \delta \bar{s}(t). \end{aligned} \quad (2.25)$$

In this equation z^+ is located where electrons leave the scatterer. Importantly, here Tr still denotes a trace over channel and Keldysh indices. We will later on redefine the symbol to include also a trace over the (continuous) time index, at which point the second term in Eq. (2.24) will (perhaps deceptively) look less offensive, but not yet. In the last line of Eq. (2.25), $\bar{s}(t) = \bar{s}(z^+, t)$ is the (time-dependent) scattering matrix. We sent the boundaries t_0 and t_1 over which we integrate in the definition of the action, to $-\infty$ and ∞ respectively, which will allow us to Fourier transform to frequency in a moment. The action remains well-defined as long as the potentials u^+ and u^- only differ for a finite time.

2.2.4 Relating g inside the scattering region to g at reservoirs.

Our task is now to find $\bar{g}(z^-, t - 0^+; z^-, t)$. Because of the $t - t'$ dependence of the self-energy, it is convenient to transform to Fourier space, where

$$\begin{aligned}\bar{g}(z, \varepsilon; z^-, \varepsilon') &= \int dt dt' e^{i\varepsilon t} \bar{g}(z, t; z^-, t') e^{-i\varepsilon' t'}, \\ \bar{G}_{\text{in(out)}}(\varepsilon) &= \int dt e^{i\varepsilon t} \bar{G}(t)_{\text{in(out)}}.\end{aligned}\quad (2.26)$$

In frequency domain, the property that $\bar{G}_{\text{in(out)}}$ squares to unity is expressed as $\bar{G}_{\text{in(out)}}(\varepsilon)^2 = \bar{1}$. (Due to the standard conventions for Fourier transforms, the matrix elements of the identity operator in energy domain is $2\pi\delta(\varepsilon - \varepsilon')$.) The equation of motion for $z < z^-$ reads

$$\left\{ -i\varepsilon + v_F \partial_z + \frac{\bar{G}_{\text{in}}(\varepsilon)}{2\tau_c} \right\} \bar{g}(z, \varepsilon; z^-, \varepsilon') = 0. \quad (2.27)$$

There is no inhomogeneous term on the right-hand side, because we restrict z to be less than z^- . We thus find

$$\bar{g}(z^- - 0^+, \varepsilon; z^-, \varepsilon') = e^{i\varepsilon \Delta z / v_F} \exp \left[-\frac{\bar{G}_{\text{in}}(\varepsilon)}{2l_c} \Delta z \right] \bar{g}(z^- - \Delta z, \varepsilon; z^-, \varepsilon'). \quad (2.28)$$

Here the correlation length l_c is the correlation time τ_c multiplied by the Fermi velocity v_F . Using the fact that $\bar{G}(\varepsilon)_{\text{in}}$ squares to unity, it is easy to verify that

$$\exp \left\{ -\frac{\bar{G}_{\text{in}}(\varepsilon)}{2l_c} \Delta z \right\} = \frac{1 + \bar{G}_{\text{in}}(\varepsilon)}{2} \exp \left(-\frac{\Delta z}{2l_c} \right) + \frac{1 - \bar{G}_{\text{in}}(\varepsilon)}{2} \exp \left(\frac{\Delta z}{2l_c} \right). \quad (2.29)$$

Since spacial correlations decay beyond z^- , $\bar{g}(z^- - \Delta z, \varepsilon; z^-, \varepsilon')$ does not blow up as we make Δz larger. From this we derive the condition

$$[1 + \bar{G}_{\text{in}}(\varepsilon)] \bar{g}(z^- - 0^+, \varepsilon; z^-, \varepsilon') = 0. \quad (2.30)$$

Transformed back to the time-domain this reads

$$\int dt'' [\delta(t - t'') + \bar{G}_{\text{in}}(t - t'')] \bar{g}(z^- - 0^+, t''; z^-, t') = 0. \quad (2.31)$$

We can play the same game at z^+ where particles leave the scatterer. The equation of motion reads

$$\left\{ -i\varepsilon + v_F \partial_z + \theta(z - z^+) \frac{\bar{G}_{\text{out}}(\varepsilon)}{2\tau_c} \right\} \bar{g}(z, \varepsilon; z^+, \varepsilon') = 2\pi \delta(z - z') \delta(\varepsilon - \varepsilon'). \quad (2.32)$$

This has the general solution

$$\begin{aligned} & \bar{g}(z, \varepsilon; z', \varepsilon') \\ &= \exp \left\{ i\varepsilon \frac{z - z'}{v_F} - \left[(z - z^+) \theta(z - z^+) \right. \right. \\ & \quad \left. \left. - (z' - z^+) \theta(z' - z^+) \right] \frac{\bar{G}_{\text{out}}(\varepsilon)}{2l_c} \right\} \\ & \quad \times \left[\bar{g}(z' - 0^+, \varepsilon'; z', \varepsilon') + \frac{2\pi}{v_F} \theta(z - z') \delta(\varepsilon - \varepsilon') \right]. \end{aligned} \quad (2.33)$$

We will need to relate the Green function evaluated at $z < z^+$ to the Green function evaluated at $z > z^+$, and so we explicitly show the inhomogeneous term. The same kind of argument employed at z^- then yields the condition

$$[1 - \bar{G}_{\text{out}}(\varepsilon)] \left[\bar{g}(z^+ - 0^+, \varepsilon; z^+, \varepsilon') + \frac{2\pi}{v_F} \delta(\varepsilon - \varepsilon') \right] = 0, \quad (2.34)$$

where the inhomogeneous term in the equation of motion is responsible for the delta-function. In time-domain this reads

$$\begin{aligned} & \int dt'' [\delta(t - t'') - \bar{G}_{\text{out}}(t - t'')] \left[\bar{g}(z^+ - 0^+, t''; z^+, t') \right. \\ & \quad \left. + \frac{1}{v_F} \delta(t'' - t') \right] = 0. \end{aligned} \quad (2.35)$$

It remains for us to relate $\bar{g}(z^+ - 0^+, t + \frac{z^+ - z^-}{v_F}; z^+, t' + \frac{z^+ - z^-}{v_F})$ to $\bar{g}(z^- - 0^+, t; z^-, t')$. This is done with the help of Eq. (2.22), from which follows

$$\bar{g}(z^+ - 0^+, t + \frac{z^+ - z^-}{v_F}; z^+, t' + \frac{z^+ - z^-}{v_F}) = \bar{s}(t)\bar{g}(z^- - 0^+, t; z^-, t')\bar{s}^\dagger(t'). \quad (2.36)$$

We substitute this into Eq. (2.35), multiply from the right with $\bar{s}(t')$ and from the left with $\bar{s}^\dagger(t)$. If we define $\bar{G}'_{\text{out}}(t, t') = \bar{s}^\dagger(t)\bar{G}_{\text{out}}(t - t')\bar{s}(t')$ the resulting boundary condition is

$$\int dt'' [\delta(t - t'') - \bar{G}'_{\text{out}}(t - t'')] [\bar{g}(z^- - 0^+, t''; z^-, t') + \frac{1}{v_F}\delta(t'' - t')] = 0. \quad (2.37)$$

2.2.5 Finding the variation of the action in terms of the reservoir Green functions and the scattering matrix

At this point, it is convenient to incorporate time into the matrix-structure of the objects \bar{G}_{in} , \bar{G}'_{out} and \bar{g} . The resulting matrices will be written without overbars. Thus for instance s will denote a matrix diagonal in time-indices, whose entry (t, t') is $\delta(t - t')\bar{s}(t)$. Similarly the (t, t') entry of $G_{\text{in}(\text{out})}$ is $\bar{G}_{\text{in}(\text{out})}(t - t')$. Also let g^- be the matrix whose (t, t') entry is $\bar{g}(z^- - 0^+, t; z^-, t')$. In this notation $G_{\text{in}}^2 = G_{\text{out}}'^2 = I$ and Eq. (2.31) and Eq. (2.37) read

$$\begin{aligned} (I + G_{\text{in}})g^- &= 0, \\ (I - G'_{\text{out}})(g^- + 1/v_F) &= 0. \end{aligned} \quad (2.38)$$

These two equations determine g^- uniquely as follows: From the first of the two equations we have

$$\begin{aligned} 0 &= G'_{\text{out}}(I + G_{\text{in}})g^- \\ &= -(I - G'_{\text{out}})g^- + (I + G'_{\text{out}}G_{\text{in}})g^-. \end{aligned} \quad (2.39)$$

In the first term we can make the substitution $-(I - G'_{\text{out}})g^- = (I - G'_{\text{out}})/v_F$ which follows from Eq. (2.38). Thus we find

$$\begin{aligned} g^- &= -\frac{1}{v_F} \frac{1}{I + G'_{\text{out}} G_{\text{in}}} (I - G'_{\text{out}}) \\ &= \frac{1}{v_F} (1 - G_{\text{in}}) \frac{1}{G'_{\text{out}} + G_{\text{in}}}, \end{aligned} \quad (2.40)$$

and the last line follows from the fact that $G_{\text{in}}^2 = G'_{\text{out}}{}^2 = I$. We have taken special care here to allow for different reservoir Green functions at z^- where particles enter the conductor and z^+ where they leave the conductor. In order to proceed we must now absorb the difference between the two Green functions in the scattering matrix. We define Λ through the equation

$$\bar{G}_{\text{out}} = \Lambda^{-1} G_{\text{in}} \Lambda, \quad (2.41)$$

and drop subscripts on the Green functions by setting $G \equiv G_{\text{in}}$. Substituted back into Eq. (2.24) for the variation of the action yields

$$\delta\mathcal{A} = \text{Tr} \left[\delta s' (1 - G) \frac{1}{G s' + s' G} \right] - \text{Tr} \left[\delta \hat{s}_- (\hat{s}_-)^{\dagger} \right], \quad (2.42)$$

where the trace is over time, channel and, in the first term, Keldysh indices. The operator s' is related to the scattering matrix s through $s' = \Lambda s$.

2.2.6 Integrating the variation to find the action

We now have to integrate $\delta\mathcal{A}$ to find \mathcal{A} . This is most conveniently done by working in a basis where G is diagonal. Since $G^2 = 1$, every eigenvalue of G is ± 1 . Therefore, there is a basis in which

$$G = \begin{pmatrix} I & 0 \\ 0 & -I \end{pmatrix}. \quad (2.43)$$

In this representation s' can be written as

$$s' = \begin{pmatrix} s'_{11} & s'_{12} \\ s'_{21} & s'_{22} \end{pmatrix}. \quad (2.44)$$

Here the two indices of the subscript has the following meaning: The first refers to a left eigenspace of G , the second to a right eigenspace. A subscript 1 denotes the subspace of eigenstates of G with eigenvalue 1. A

subscript 2 refers to the subspace of eigenstates of G with eigenvalue -1 . In this representation,

$$(1 - G) \frac{1}{Gs' + s'G} = \begin{pmatrix} 0 & 0 \\ 0 & (s'_{22})^{-1} \end{pmatrix}, \quad (2.45)$$

so that

$$\delta\mathcal{A} = \text{Tr} [\delta s'_{22} (s'_{22})^{-1}] - \text{Tr} [\delta \hat{s}_- (\hat{s}_-)^{\dagger}], \quad (2.46)$$

and thus

$$\begin{aligned} \mathcal{A} &= \text{Tr} \ln s'_{22} - \text{Tr} \ln s_-, \\ e^{\mathcal{A}} &= (\text{Det } s_-)^{-1} \text{Det } s'_{22}. \end{aligned} \quad (2.47)$$

In these equations, s_- is the scattering matrix associated with \mathcal{H}^- as defined previously. Its time structure is to be included in the operations of taking the trace and determinant.

Note that in the representation where G is diagonal, it holds that

$$\frac{1+G}{2} + s' \frac{1-G}{2} = \begin{pmatrix} I & s'_{12} \\ 0 & s'_{22} \end{pmatrix}. \quad (2.48)$$

Due to the upper-(block)-triangular structure it holds that $\text{Det } s'_{22} = \text{Det} [\frac{1+G}{2} + s' \frac{1-G}{2}]$ leading to our main result

$$\mathcal{A} = \text{Tr} \ln \left[\frac{1+G}{2} + s' \frac{1-G}{2} \right] - \text{Tr} \ln s_-. \quad (2.49)$$

where it has to be noted that many matrices have the same determinant as the above. Some obvious examples include

$$\begin{aligned} \begin{pmatrix} I & 0 \\ 0 & s'_{22} \end{pmatrix} &= (1+G)/2 + (1-G)s'(1-G)/4, \\ \begin{pmatrix} I & 0 \\ s'_{21} & s'_{22} \end{pmatrix} &= (1+G)/2 + (1-G)s'/2. \end{aligned} \quad (2.50)$$

2.3 Tracing out the Keldysh structure

Up to this point the only property of G that we relied on was the fact that it squares to identity. Hence the result (Eq. 2.49) holds in a setting that is more general than that of a scatterer connected to reservoirs characterized

by filling factors. (The reservoirs may for instance be superconducting). In the specific case of reservoirs characterized by filling factors it holds that

$$\bar{G}(\tau) = \int \frac{d\varepsilon}{2\pi} e^{-i\varepsilon\tau} \begin{pmatrix} 1 - 2\hat{f}(\varepsilon) & 2\hat{f}(\varepsilon) \\ 2 - 2\hat{f}(\varepsilon) & -1 + 2\hat{f}(\varepsilon) \end{pmatrix}. \quad (2.51)$$

Here $\hat{f}(\varepsilon)$ is diagonal in channel indices, and $f_m(\varepsilon)$ is the filling factor in the reservoir connected to channel m . We will also assume that electrons enter and leave a channel from the same reservoir, so that $G_{\text{in}} = G_{\text{out}}$ and hence $s' = s$. We recall as well as that the Keldysh structure of the scattering matrix is

$$s = \begin{pmatrix} \hat{s}_+ & 0 \\ 0 & \hat{s}_- \end{pmatrix}. \quad (2.52)$$

Here \hat{s}_\pm have channel and time (or equivalently energy) indices. \hat{s}_\pm is diagonal in time-indices, with the entries on the time-diagonal the time-dependent scattering matrices corresponding to evolution with the Hamiltonians \mathcal{H}_\pm .

With this structure in Keldysh space, we find

$$\begin{aligned} e^{\mathcal{A}} = & \text{Det} \begin{pmatrix} 1 + (\hat{s}_+ - 1)\hat{f} & -(\hat{s}_+ - 1)\hat{f} \\ (\hat{s}_- - 1)(\hat{f} - 1) & \hat{s}_-(1 - \hat{f}) + \hat{f} \end{pmatrix} \\ & \times \text{Det} \begin{pmatrix} 1 & \\ & \hat{s}_-^{-1} \end{pmatrix}. \end{aligned} \quad (2.53)$$

We can remove the Keldysh structure from the determinant with the aide of the general formula

$$\begin{aligned} \text{Det} \begin{pmatrix} A & B \\ C & D \end{pmatrix} &= \text{Det}(AD - ACA^{-1}B) \\ &= \text{Det}(DA - CA^{-1}BA). \end{aligned} \quad (2.54)$$

Noting that in our case the matrices B and A commute, so that $CA^{-1}BA = CB$, we have

$$\begin{aligned} e^{\mathcal{A}} &= \text{Det} \left[\left(\hat{s}_-(1 - \hat{f}) + \hat{f} \right) \left(1 + (\hat{s}_- - 1)\hat{f} \right) \right. \\ &\quad \left. - \left(\hat{s}_-(1 - \hat{f}) + \hat{f} - 1 \right) (\hat{s}_+ - 1)\hat{f} \right] \text{Det} (\hat{s}_-^{-1}) \\ &= \text{Det} \left[\hat{s}_-(1 - \hat{f}) + \hat{s}_+\hat{f} \right] \text{Det} (\hat{s}_-^{-1}). \end{aligned} \quad (2.55)$$

2.4 An example: Full Counting Statistics of transported charge

A determinant formula of this type appears in the literature of Full Counting Statistics [5] of transported charge. This formula can be stated as follows: the generating function for transported charge through a conductor characterized by a time-independent scattering matrix \hat{s} is

$$\mathcal{Z}(\chi) = \text{Det} \left[1 + (\hat{s}_{-\chi}^\dagger \hat{s}_\chi - 1) \hat{f} \right], \quad (2.56)$$

where \hat{s}_χ is a scattering matrix, modified to depend on the counting field χ that, in this case, is time-independent. (The precise definition may be found below.)

As a consistency check of our results, we apply our analysis to re-derive this formula. We will consider the most general setup, where every scattering channel is connected to a distinct voltage-biased terminal. To address the situation where leads connect several channels to the same terminal, the voltages and “counting fields” associated with channels in the same lead are set equal.

The full counting statistics of charge transported through a scatterer in a time-interval t is defined as

$$\mathcal{Z}(\chi, t) = \langle e^{i\mathcal{H}_\chi t} e^{-i\mathcal{H}_{-\chi} t} \rangle. \quad (2.57)$$

In this equation, the Hamiltonian \mathcal{H}_χ is given by

$$\mathcal{H}_\chi = v_f \sum_{m,n} \int dz \psi_m^\dagger(z) \{-i\partial_z \delta_{m,n} + u_{m,n}(z)\} \psi_n(z) + \sum_m \chi_m I_m(z_0), \quad (2.58)$$

where $I_m(z_0)$ is the current in channel m at the point z_0 which is taken to lie outside the scattering region. The full counting statistics is thus generated by coupling counting field χ_m to the current operator in a channel m .

Explicitly the current operator in channel m is given by

$$I_m(z_0) = v_F \left(\psi_m^\dagger(z_0) \psi_m(z_0) - \psi_m^\dagger(-z_0) \psi_m(-z_0) \right). \quad (2.59)$$

To understand this equation, recall that the co-ordinates z_0 and $-z_0$ in channel m refer to the same point in space, but opposite propagation directions.

The presence of current operators in Eq. (2.58) can be incorporated in the potential by defining a transformed potential

$$u_{m,n}^{(\chi)}(z) = u_{m,n}(z) + \delta_{m,n} \frac{\chi_m}{2} (\delta(z - z_0) - \delta(z + z_0)). \quad (2.60)$$

Introducing counting fields that transform $\mathcal{H}_0 \rightarrow \mathcal{H}_\chi$ is thus achieved by transforming $u \rightarrow u^{(\chi)}$.

The calculation of the full counting statistics has now been cast into the form of the trace of a density matrix after forward and backward time evolution controlled by different scattering potentials. Our result, Eq. (2.55), is therefore applicable, with

$$\begin{aligned} \hat{s}_\pm &= \mathcal{Z} \exp \left(-i \int_{z_-}^{z_+} dz \hat{u}^{(\pm\chi)}(z) \right) \\ &= e^{\mp i \hat{\chi}/2} s_0 e^{\pm i \hat{\chi}/2} = s_{\pm\chi}. \end{aligned} \quad (2.61)$$

In this equation, $\hat{\chi}$ is a diagonal matrix in channel space, with entries $\delta_{m,n} \chi_m$. Substitution into Eq. (2.55) gives

$$\mathcal{Z}(\chi) = \text{Det} \left[1 + (\hat{s}_{-\chi}^\dagger \hat{s}_\chi - 1) \hat{f} \right], \quad (2.62)$$

in agreement with the existing literature [5].

2.5 Tracing out the channel structure

A large class of experiments and devices in the field of quantum transport is based on two terminal setups. In such a setup the channel space of the scatterer is naturally partitioned into a left and right set, each connected to its own reservoir. We are generally interested in transport between left and right as opposed to internal dynamics on the left- or right-hand sides. The scattering matrices have the general structure

$$\hat{s}_\pm = X \begin{pmatrix} r & t' \\ t & r' \end{pmatrix} X^{-1}, \quad X = \begin{pmatrix} X_L^\pm & \\ & X_R^\pm \end{pmatrix}. \quad (2.63)$$

Here r (r') describes left (right) to left (right) reflection, while t (t') describes left (right) to right (left) transmission (t is not to be confused with time). These matrices have no time or Keldysh structure but still have matrix structure in the space of left or right channel indices. The

operators $X_L^\pm(\tau)$ and $X_R^\pm(\tau)$ have diagonal Keldysh structure (denoted by the superscript \pm) and diagonal time structure (here indicated by τ to avoid confusion with the transmission matrix t). They do not have internal channel structure and as a result the Keldysh action is insensitive to the internal dynamics on the left- or right-hand sides. Our shorthand for the Keldysh scattering matrix will be XsX^{-1} where we remember that s has no Keldysh structure.

We now consider the square of the generating functional \mathcal{Z} and employ the first expression we obtained for it (Eq. 2.49) which retains Keldysh structure in the determinant.

$$\mathcal{Z}^2 = \text{Det} \left[\frac{1+G}{2} + XsX^{-1} \frac{1-G}{2} \right]^2 \text{Det} s^\dagger. \quad (2.64)$$

Here we exploited the fact that \hat{s}_- acts on half of Keldysh space together with the fact that $\hat{s}_+ = \hat{s}_-$, i.e. s has no Keldysh structure, to write $\exp 2\text{Tr} \ln \hat{s}_- = \text{Det} s$. We now shift X to act on G and define

$$\check{G} = X^{-1}GX, \quad P = \frac{1+\check{G}}{2}, \quad Q = \frac{1-\check{G}}{2}. \quad (2.65)$$

The operators P and Q are complementary projection operators i.e. $P^2 = P$, $Q^2 = Q$, $PQ = QP = 0$ and $P + Q = I$. Because of this, it holds that $\text{Det}(P + sQ) = \text{Det}(P + Qs)$. Thus we find

$$\mathcal{Z}^2 = e^{2\mathcal{A}} = \text{Det}(Ps^\dagger + sQ). \quad (2.66)$$

The left channels are all connected to a single reservoir while the right channels are all connected to a different reservoir. This means that the reservoir Green function has channel space structure

$$\check{G} = \begin{pmatrix} \check{G}_L & \\ & \check{G}_R \end{pmatrix}, \quad (2.67)$$

where G_L and G_R have no further channel space structure. At this point it is worth explicitly stating the structure of operators carefully. In general, an operator carries Keldysh indices, indices corresponding to left and right, channel indices within the left or right sets of channels, and time indices. However P , Q and s are diagonal or even structureless, i.e. proportional to identity in some of these indices. Let us denote Keldysh indices with $k, k' \in \{+, -\}$, left and right with $\alpha, \alpha' \in \{L, R\}$, channel indices within

the left or right sets with $c, c' \in Z$ and time $t, t' \in R$. Then P has the explicit form

$$P(k, k'; \alpha, \alpha'; c, c'; t, t') = P(k, k'; \alpha; t, t') \delta_{\alpha, \alpha'} \delta_{c, c'}. \quad (2.68)$$

The projection operator Q has the same structure. The scattering matrix s has the structure

$$s(k, k'; \alpha, \alpha'; c, c'; t, t') = s(\alpha, \alpha'; c, c') \delta_{k, k'} \delta(t - t'). \quad (2.69)$$

We now use the formula $\text{Det} \begin{pmatrix} A & B \\ C & D \end{pmatrix} = \text{Det}(A) \text{Det}(D - CA^{-1}B)$ to eliminate left-right structure from the determinant.

$$\begin{aligned} \mathcal{Z}^2 &= \begin{pmatrix} P_L r^\dagger + Q_L r & P_L t^\dagger + Q_R t' \\ P_R t'^\dagger + Q_L t & P_R r'^\dagger + Q_R r' \end{pmatrix} \\ &= \text{Det} \left(P_L r^\dagger + Q_L r \right) \text{Det} \left[P_R r'^\dagger + Q_R r' \right. \\ &\quad \left. - \left(P_R t'^\dagger + Q_L t \right) \left(P_L r^\dagger + Q_L r \right)^{-1} \left(P_L t^\dagger + Q_R t' \right) \right] \\ &= a \times b, \end{aligned} \quad (2.70)$$

where $a = \text{Det}(P_L r^\dagger + Q_L r)$ and

$$\begin{aligned} b &= \text{Det} \left[P_R (r'^\dagger - P_L t'^\dagger r^{\dagger -1} t^\dagger) + (r' - Q_L t r^{-1} t') Q_R \right. \\ &\quad \left. - P_R (P_L t'^\dagger r^{\dagger -1} t' + Q_L t'^\dagger r^{-1} t') Q_R \right]. \end{aligned} \quad (2.71)$$

Here it is important to recognize that the reflection and transmission matrices commute with the projection operators $P_{L,R}$ and $Q_{L,R}$. Furthermore, notice that, in term b , the projection operator P_R always appears on the left of any product involving other projectors, while Q_R always appears on the right. This means that in the basis where

$$P_R = \begin{pmatrix} I & 0 \\ 0 & 0 \end{pmatrix}, \quad Q_R = \begin{pmatrix} 0 & 0 \\ 0 & I \end{pmatrix}, \quad (2.72)$$

term b is the determinant of an upper block-diagonal matrix. As such, it only depends on the diagonal blocks, so that the term $P_R(\dots)Q_R$ may be omitted. Hence

$$b = \text{Det} \left[P_R (r'^\dagger - P_L t'^\dagger r^{\dagger -1} t^\dagger) + (r' - Q_L t r^{-1} t') Q_R \right]. \quad (2.73)$$

Now we invoke the so-called polar decomposition of the scattering matrix [26]

$$\begin{aligned} r &= u\sqrt{1-T}u', & t' &= iu\sqrt{T}v, \\ t &= iv'\sqrt{T}u', & r' &= v'\sqrt{1-T}v, \end{aligned} \quad (2.74)$$

where u, u', v and v' are unitary matrices and T is a diagonal matrix with the transmission probabilities T_n on the diagonal. We evaluate term a in the basis where P_L and Q_L are diagonal to find

$$\begin{aligned} a &= \text{Det} \begin{pmatrix} u'^{\dagger}\sqrt{1-T}u^{\dagger} & 0 \\ 0 & u\sqrt{1-T}u' \end{pmatrix} \\ &= \text{Det} \left(I\sqrt{1-T} \right), \end{aligned} \quad (2.75)$$

where $I = P_L + Q_L = P_R + Q_L$ is the identity operator $I(k, k'; c, c'; t, t') = \delta_{k, k'}\delta_{c, c'}\delta(t - t')$ in Keldysh, channel and time indices. For term b we find

$$\begin{aligned} b &= \text{Det} \left[P_R \left(\sqrt{1-T} + P_L \frac{T}{\sqrt{1-T}} \right) \right. \\ &\quad \left. + \left(\sqrt{1-T} + Q_L \frac{T}{\sqrt{1-T}} \right) Q_R \right]. \end{aligned} \quad (2.76)$$

Combining the expressions for a and b we find

$$\mathcal{Z}^2 = e^{2\mathcal{A}} = \text{Det} [1 - T(P_R Q_L + P_L Q_R)]. \quad (2.77)$$

Using the fact that $P_{L(R)} = (1 + \check{G}_{L(R)})/2$ and $Q_{L(R)} = (1 - \check{G}_{L(R)})/2$ and taking the logarithm we finally obtain the remarkable result

$$\mathcal{A} = \frac{1}{2} \sum_n \text{Tr} \ln \left[1 + \frac{T_n}{4} (\{\check{G}_L, \check{G}_R\} - 2) \right]. \quad (2.78)$$

This formula was used in Ref. [12] to study the effects on transport of electromagnetic interactions among electrons. In Ref. [14] the same formula was employed to study the output of a two-level measuring device coupled to the radiation emitted by a QPC.

2.6 An example: The Fermi Edge Singularity

In this section we show how our formulas apply to a phenomenon known as the Fermi Edge Singularity. The system under consideration is one of the

most elementary examples of an interacting electron system. The initial analysis [6, 7] relied on diagrammatic techniques rather than the scattering approach or the Keldysh technique, and was confined to equilibrium situations. Several decades later the problem was revisited in the context of the scattering approach [10, 11]. An intuitive derivation of a determinant formula was given. Here we apply our approach to confirm the validity of this previous work. We find exact agreement. This highlights the fact that the determinant formulation of the FES problem is also valid for multi-channel devices out of equilibrium, an issue not explicitly addressed in the existing literature.

The original problem [6, 7] was formulated for conduction electrons with a small effective mass and valence electrons with a large effective mass, bombarded by x-rays. The x-rays knock one electron out of the valence band leaving behind an essentially stationary hole. Until the hole is refilled, it interacts through the coulomb interaction with the conduction electrons. The x-ray absorption rate is studied. Abanin and Levitov reformulated the problem in the context of quantum transport where an electron tunnels into or out of a small quantum dot that is side-coupled to a set of transport channels.

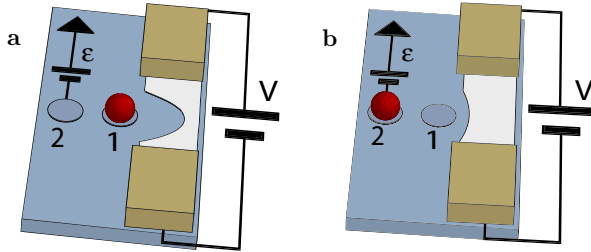


Figure 2.2. A schematic picture of the system considered. It consists of a charge qubit coupled to a QPC. The shape of the QPC constriction, and hence its scattering matrix, depends on the state of the qubit. A gate voltage controls the qubit level splitting ε . There is a small tunneling rate γ between qubit states.

We prefer to consider a slightly simpler setup that exhibits the same physics. The setup is illustrated in Fig. (2.2). A Quantum Point Contact (QPC) interacts with a charge qubit. The shape of the QPC constriction depends on the state of the qubit. We will consider the same system again

in Chapter 4 of this thesis. The Hamiltonian for the system is

$$\mathcal{H} = \mathcal{H}_1 |1\rangle\langle 1| + (\mathcal{H}_2 + \varepsilon) |2\rangle\langle 2| + \gamma(|1\rangle\langle 2| + |2\rangle\langle 1|). \quad (2.79)$$

The operators \mathcal{H}_1 (\mathcal{H}_2) describe the QPC electrons when the qubit is in state $|1\rangle$, ($|2\rangle$). They differ by a potential energy term, describing the pinching off of the QPC constriction depending on the state of the qubit. We may take both Hamiltonians to be of the form (Eq. 2.5) that we wrote down for a general scatterer. The energy ε is the qubit level splitting, an experimentally tunable parameter. The QPC may be driven by a voltage bias V .

QPC electrons do not interact directly with each other but rather with the qubit. This interaction is the only qubit relaxation mechanism included in our model. We work in the limit $\gamma \rightarrow 0$ where the inelastic transition rates $\Gamma_{12,21}$ between qubit states are small compared to the energies eV and ε . In this case, the qubit switching events can be regarded as independent and incoherent.

Now consider the qubit transition rate Γ_{21} , from state $|1\rangle$ to $|2\rangle$ as a function of the qubit level splitting ε . To lowest order in the tunneling amplitude γ it is given by

$$\begin{aligned} \Gamma_{21} &= 2\gamma^2 \text{Re} \int_{-\infty}^0 d\tau e^{i\varepsilon\tau} \lim_{t_0 \rightarrow -\infty} \exp \mathcal{A}(\tau), \\ \exp \mathcal{A}(\tau) &= \text{tr} \left[e^{i\hat{H}_2\tau} e^{-i\hat{H}_1(\tau-t_0)} \rho_0 e^{-i\hat{H}_1 t_0} \right]. \end{aligned} \quad (2.80)$$

This is the usual Fermi Golden Rule. The time τ over which we integrate can be interpreted as the time when the qubit switches from $|1\rangle$ to $|2\rangle$. The trace is over QPC states, and ρ_0 is the initial QPC density matrix. We see that the expression for Γ_{21} contains an instance of the Keldysh action \mathcal{A} that we have calculated. The correspondence requires us to set

$$\begin{aligned} \mathcal{H}^+(t) &= \mathcal{H}_1 + (\mathcal{H}_2 - \mathcal{H}_1)\theta(t - \tau)\theta(-t), \\ \mathcal{H}^-(t) &= \mathcal{H}_1. \end{aligned} \quad (2.81)$$

In order to conform to the conventions of the existing literature, we write \mathcal{Z} in the form where the Keldysh structure has been removed (Eq. 2.4):

$$\mathcal{A}(\tau) = \text{tr} \ln \left[\hat{s}_-(1 - \hat{f}) + \hat{s}_+(\tau)\hat{f} \right] - \text{tr} \ln \hat{s}_-. \quad (2.82)$$

In this formula, \hat{s}_- is the scattering matrix corresponding to $\mathcal{H}^- = \mathcal{H}_1$ when the qubit is in state $|1\rangle$. It is proportional to identity in time-indices.

The scattering matrix $\hat{s}_+(\tau)$ corresponds to \mathcal{H}^+ . It is still diagonal in time-indices but the diagonal elements $\hat{s}_+(\tau)_t$ are time-dependent. If we take the time it takes an electron to traverse the conductor to be much shorter than other time-scales such as the inverse of the attempt rate of charge transfers, then

$$\hat{s}_+(\tau)_t = \hat{s}_1 + (\hat{s}_2 - \hat{s}_1)\theta(t - \tau)\theta(-t), \quad (2.83)$$

where \hat{s}_2 is the scattering matrix associated with \mathcal{H}_2 when the qubit is in state $|2\rangle$. This expression first appeared in Ref. [10]. In the language of the original diagrammatic treatment of the FES problem [6, 7], it represents the total closed loop contribution.

We may also write this closed loop contribution as

$$e^{\mathcal{A}(\tau)} = \text{Det} \left[1 + (\hat{s}_1^\dagger \hat{s}_2 - 1) \hat{\Pi}(\tau) \hat{f} \right], \quad (2.84)$$

where $\hat{\Pi}$ is a diagonal operator in time-domain with a kernel that is a double step function

$$\Pi(\tau)_{t,t'} = \theta(-t)\theta(t - \tau). \quad (2.85)$$

and the scattering matrices \hat{s}_1 and \hat{s}_2 no longer have time-structure. We may work in the channel space basis where $\hat{s}_1^\dagger \hat{s}_2$ is diagonal. Its eigenvalues are $e^{i\lambda_k}$. Suppose we are in zero-temperature equilibrium, then the filling factor f is the same in every channel. In the fourier transformed energy basis f is simply a step function:

$$f_{\varepsilon,\varepsilon'} = \delta(\varepsilon - \varepsilon')\theta(-\varepsilon). \quad (2.86)$$

Thus one finds

$$e^{\mathcal{A}} = \prod_k \text{Det} \left[1 + (e^{i\lambda_k} - 1) \hat{\Pi}(\tau) \hat{f} \right]. \quad (2.87)$$

This determinant contains no channel structure any more. Operators only have one set of indices (time, or after Fourier transform, energy). $\hat{\Pi}$ is a projection operator, diagonal in time-domain while \hat{f} is a projection operator in energy domain. Such a determinant is known as a Fredholm determinant.

The resulting transition rate is [6, 7, 10]

$$\Gamma_{21}(\varepsilon) = \theta(-\varepsilon) \frac{1}{|\varepsilon|} \left(\frac{|\varepsilon|}{E_{c.o}} \right)^\alpha, \quad (2.88)$$

where $E_{c.o}$ is a cut-off energy of the order of the Fermi energy measured from the bottom of the conduction band. The exponent α is known as the orthogonality exponent. It may be calculated by evaluating the Fredholm determinant analytically with the Wiener-Hopf method. It is given in terms of the scattering matrices as [9, 10]

$$\alpha = \frac{1}{4\pi^2} \left| \text{tr} \ln^2 \left(s_1^\dagger s_2 \right) \right|, \quad (2.89)$$

with the trace being over channel indices. Inspired by the work of Abanin and Levitov [10, 11] we considered the case where the QPC is driven by a voltage bias. The results of our study may be found in Chapter 4 of this thesis.

2.7 Conclusion

In this paper we have derived several expressions for the Keldysh action \mathcal{A} for a general multi-terminal, time-dependent scatterer. This object is defined as the (logarithm of the) trace of the density matrix of the scatterer after evolution forwards and backwards in time with different Hamiltonians:

$$e^{\mathcal{A}} = \text{Tr} \left[\mathcal{T}^+ \exp \left\{ -i \int_{t_0}^{t_1} dt \mathcal{H}^+(t) \right\} \rho_0 \mathcal{T}^- \exp \left\{ i \int_{t_0}^{t_1} dt \mathcal{H}^-(t) \right\} \right]. \quad (2.90)$$

Our main result is a compact formula for the action in terms of reservoir Green functions and the scattering matrix of the scatterer (Eq. 2.1). We have shown how to perform the trace over Keldysh indices explicitly when reservoirs are characterized by filling factors. Thus we obtained a formula (Eq. 2.2) generalizing the Levitov counting statistics formula. We have also explicitly performed the trace over channel indices for a two terminal scatterer (Eq. 2.4). In this case we demonstrated that the Keldysh action only depends on the scattering matrix through the eigenvalues of the transmission matrix. To illustrate the utility of the Keldysh action, and confirm the correctness of our results, we considered Full Counting statistics and the Fermi Edge singularity. We found that our results agree with the existing literature.

Bibliography

- [1] R. Landauer, IBM J. Res. Dev. **1**, 223 (1957); Philos. Mag. **21**, 863 (1970).
- [2] M. Büttiker, IBM J. Res. Dev. **32**, 63 (1988).
- [3] G. B. Lesovik , JETP Lett, **49**, 592 (1989).
- [4] L. S. Levitov and G. B. Lesovik, JETP Lett. **58**, 230 (1993).
- [5] L. S. Levitov, H.-W. Lee and G. B. Lesovik, J. Math. Phys. **37**, 10 (1996).
- [6] G. D. Mahan, Phys. Rev. **163**, 612 (1967).
- [7] P. Nozières and C. T. De Dominicis, Phys. Rev. **178**, 1097 (1969).
- [8] K. A. Matveev and A. I. Larkin, Phys. Rev. B **46**, 15337 (1992).
- [9] K. Yamada and K. Yosida, Prog. Th. Phys. **68**, 1504 (1982).
- [10] D. A. Abanin and L. S. Levitov, Phys. Rev. Lett. **93**, 126802 (2004).
- [11] D. A. Abanin and L. S. Levitov, Phys. Rev. Lett. **94**, 186803 (2005).
- [12] M. Kindermann and Yu. V. Nazarov, Phys. Rev. Lett. **91**, 136802 (2003).
- [13] M. Kindermann, Yu. V. Nazarov and C.W.J. Beenakker, Phys. Rev. B **69**, 035336 (2004).
- [14] J. Tobiska, J. Danon, I. Snyman and Yu. V. Nazarov, Phys. Rev. Lett. **96**, 096801 (2006); This thesis, Chapter 3.

-
- [15] I. Snyman and Yu. V. Nazarov, Phys. Rev. Lett. **99**, 096802 (2007); This thesis, Chapter 4.
- [16] C. W. J. Beenakker, in *Transport Phenomena in Mesoscopic Systems*, edited by H. Fukuyama and T. Ando, (Springer, New York, 1992).
- [17] R. P. Feynman and F. L. Vernon jr., Ann. Phys. (N.Y.) **24**, 118 (1963).
- [18] L. V. Keldysh, Zh. Eksp. Teor. Phys. **47**, 1515 (1964). [Sov. Phys. JETP **20**, 198 (1965).]
- [19] Yu. V. Nazarov, Superlattices Microstruct. **25**, 1221 (1999).
- [20] Yu. V. Nazarov, Phys. Rev. Lett. **73**, 1420 (1994).
- [21] G. Schön and A. D. Zaikin, Phys. Rep. **198**, 237 (1990).
- [22] Yu. V. Nazarov, Phys. Rev. Lett. **82**, 1245 (1999).
- [23] Yu. V. Nazarov, in: *Handbook of Theoretical and Computational Nanotechnology*, edited by M. Rieth and W. Schommers, (American Scientific Publishers, Stevenson Ranch, CA, 2006).
- [24] K. B. Efetov, in *Supersymmetry in Disorder and Chaos*, (Cambridge University Press, Cambridge, 1999); M. V. Feigel'man, A. I. Larkin and M. A. Skvortsov, Phys. Rev. B **61**, 12361 (2000).
- [25] J. Rammer and H. Smith, Rev. Mod. Phys. **58**, 323 (1986).
- [26] H. U. Baranger and P. A. Mello, Phys. Rev. Lett. **73**, 142 (1994).

Chapter 3

Quantum tunneling detection of two-photon and two-electron processes

3.1 Introduction

The quantum nature of electron transfer in coherent conductors is seldom explicitly manifested in averaged current-voltage curves. To reveal it one should measure current noise and/or the higher-order correlations of current comprising the Full Counting Statistics that arise from the transfer [1]. Such measurements not only reveal the discrete nature of the charges transferred, they also quantify quantum many-body effects in electron transport and may be used for the detection of pairwise entanglement of transferred particles [2, 3, 4, 5]. If the noise is measured at frequencies in the quantum range, $\hbar\omega \gg k_B T$, the measurement amounts to the detection of photons produced by the current fluctuations. This aspect is important in view of attempts to transfer quantum information from electrons to photons and back [6].

It was demonstrated in Ref. [7] that one needs a quantum detector to measure quantum noise. Indeed, any classical measurement of a fluctuating quantity would give a noise spectrum symmetric in frequency, $S(\omega) = S(-\omega)$. A *quantum tunneling detector* is generally a quantum two-level system with a level separation $\varepsilon > 0$. The result of detection are two transition rates: Γ_{up} from the lower to the higher level and Γ_{down} for the reverse direction. The most probable transitions are accompanied by

either absorption or emission of a photon of matching energy $\hbar\omega = \varepsilon$. One can define the noise spectrum in such a way that it is proportional to the transition rates $S(\pm\varepsilon/\hbar) \propto \Gamma_{\text{up,down}}(\varepsilon)$. Differences between $\Gamma_{\text{up,down}}$ thus manifest the quantum nature of noise. If the source of noise is a coherent conductor biased by a voltage V , detector signals in the range $\varepsilon < eV$ are readily interpreted in terms of single electron transfers through the conductor. The maximum energy gain available for electrons in the course of such transfer is eV . Consequently this value also limits the energy of the emitted photon. The previous research has not addressed the energy range $\varepsilon > eV$. It remained unclear if the detector detects anything and — if it does — what it detects.

A first proposal for the experimental realization of a quantum tunneling detector included transitions between two localized electron states in a double quantum dot [8]. However it does not matter much if the tunneling occurs between localized or delocalized electron states and if all tunnel events are accompanied by the same energy transfer ε . In most practical cases the energy dependence of the rates $\Gamma_{\text{up,down}}$ can be readily extracted from the measurement results. This is why quantum tunneling detection has been experimentally realized in a superconducting tunnel junction [9] and in a single quantum dot [10].

In this Chapter we study quantum tunneling detection in the range $eV < \varepsilon < 2eV$ assuming $\varepsilon, eV \gg k_B T$. The motivation is that for these energies the detector is not sensitive to single-electron one-photon processes described above and its output — the transition rate Γ_{up} — is determined by much more interesting two-particle processes. It is clear from plain energy considerations that transitions may originate from *two-photon* processes. Such two-photon absorption can occur given any non-equilibrium photon distribution bounded by eV , not necessarily produced by a coherent conductor. Less obvious and specific for a coherent conductor is a cooperative *two-electron* process. Indeed, if two electrons team up in crossing the conductor they can emit a single photon with an energy up to $2eV$. Essential for this cooperation are electron-electron interactions. It is known [11] that the most important electron-electron interaction in this energy range is due to the electromagnetic environment of the conductor, the same environment in which the non-equilibrium photons dwell.

We quantify the signals due to two-photon and two-electron events and find them to be of the same order of magnitude. We also show that part of the signal is due to quantum interference of these two processes: We

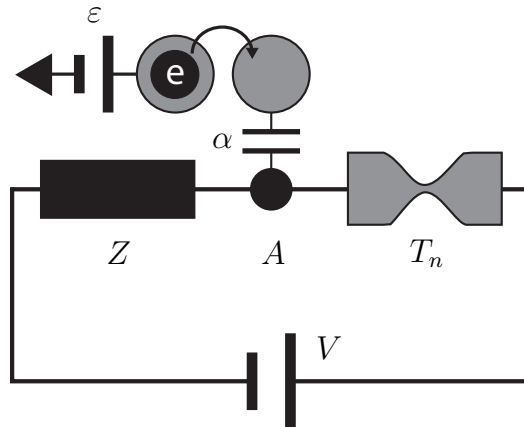


Figure 3.1. Model circuit: A coherent conductor with transmission eigenvalues T_n is connected in series with an external impedance Z . This structure is biased with a voltage V . The shared node A is capacitively coupled to a quantum tunneling detector. The coupling constant is α . The tunneling detector consists of an electron that can tunnel between the lowest two states of a double quantum dot. The level splitting ε of this two level system can be tuned by a gate voltage.

demonstrate how different contributions can be separated in experiments thereby facilitating the direct observation of two-particle processes in the context of quantum transport.

3.2 Model

We concentrate on a model circuit consisting of four elements as given in Fig. 3.1. A voltage biased coherent conductor characterized by a set of transmission eigenvalues T_n is embedded in an electromagnetic environment with impedance Z_ω . The environment transforms the current fluctuations in the conductor to voltage fluctuations in node A which are conveniently expressed in terms of a phase $\varphi = \frac{e}{\hbar} \int dt V(t)$. The most general model including the detector and the coherent conductor would be a four-pole circuit studied in Ref. [12] that couples two poles of the detector with two poles of the conductor. We use a simplified set-up in which a single pole of the detector is coupled to a single pole of the conductor. Here, we concentrate on the experimentally relevant case of capacitive coupling.

The detector senses a fraction $0 < \alpha < 1$ of the voltage fluctuations in node A. We will see that changing the “visibility” parameter α enables the separation of two-electron and two-photon processes in experiments. The relevant impedance is made up of an environmental impedance combined with that of node A and the coherent conductor. We measure this impedance z_ω in units of $R_K \equiv 2\pi\hbar/e^2$ and assume the low-impedance limit $z_\omega \ll 1$; this provides us with a physically justified small parameter.

The detector consists of two localized charge states connected by a tunnel amplitude \mathcal{T} . In the presence of voltage fluctuations in the node A, the amplitude is modified as follows: $\mathcal{T}(t) \rightarrow \mathcal{T}e^{i\alpha\varphi(t)}$. In perturbation theory, the inelastic tunneling rate between two states separated by ε is given by correlators of $\alpha\varphi(t)$ [11]

$$\Gamma(\varepsilon) = \frac{|\mathcal{T}|^2}{2\pi\hbar^2} \int dt \langle e^{i\alpha\varphi(t)} e^{-i\alpha\varphi(0)} \rangle e^{\frac{i}{\hbar}\varepsilon t}. \quad (3.1)$$

The rate $\Gamma(\varepsilon)$ is therefore the Fourier transform of the correlation function $\langle e^{i\alpha\varphi(t)} e^{-i\alpha\varphi(0)} \rangle$, $\alpha\varphi(t)$ being the phase fluctuations over the detector. From now on we take $\hbar = e = k_B = 1$.

Eq. (3.1) tells us that the inelastic tunneling rates in the detector are completely determined by the voltage fluctuations over the junction. Therefore measuring the inelastic current through the dots we are sensitive to the noise spectrum of the environment.

To evaluate $\langle e^{i\alpha\varphi(t)} e^{-i\alpha\varphi(0)} \rangle$ we construct a path integral representation of this quantity using a non-equilibrium Keldysh technique [13] for quantum-circuits [14]

$$\begin{aligned} & \langle e^{i\alpha\varphi(t)} e^{-i\alpha\varphi(0)} \rangle \\ &= \int \mathcal{D}[\varphi] \exp\{-iS_{\text{env}}[\varphi] - iS_{\text{cond}}[\varphi] + i\alpha[-\varphi^+(0) + \varphi^-(t)]\}. \end{aligned} \quad (3.2)$$

The integration goes over the time-dependent fluctuating fields $\varphi^\pm(t)$ in node A, \pm corresponding to the forward (backward) part of the Keldysh contour. S_{env} and S_{cond} are the contributions to the Keldysh action originating from the environment and the coherent conductor respectively.

Since the environment is linear, its action is quadratic in the fields and at zero temperature reads (cf. [15])

$$S_{\text{env}} = \int d\omega \phi_{-\omega}^T A(\omega) \phi_\omega, \quad (3.3)$$

with

$$A(\omega) = -\frac{i}{2} \begin{pmatrix} 0 & -\frac{\omega}{z-\omega} \\ \frac{\omega}{z_\omega} & |\omega| \operatorname{Re}\{\frac{1}{z_\omega}\} \end{pmatrix},$$

z_ω being the corresponding impedance. We use Fourier transformed fields $\phi_\omega = (\phi_\omega, \chi_\omega)^T$ defined with $\varphi^\pm = \phi \pm \frac{1}{2}\chi$.

All non-quadratic contributions to the action originate from the coherent conductor. The action S_{cond} can be expressed in terms of Keldysh Green functions $\check{G}_{L,R}$ of electrons in the reservoirs left and right of the conductor [15]

$$S_{\text{cond}} = \frac{i}{2} \sum_n \operatorname{Tr} \ln \left[1 + \frac{T_n}{4} (\{\check{G}_L(\phi), \check{G}_R\} - 2) \right]. \quad (3.4)$$

The fields ϕ enter in this action via the gauge transform of \check{G}_L [15].

3.3 The quadratic part of the action

To understand the physics involved, let us first disregard any non-quadratic parts and take only the quadratic part of S_{cond} . In this case the path integral is Gaussian, and can be evaluated exactly. We recover the well known result from $P(E)$ -theory (cf. [8, 11]): $\langle e^{i\alpha\varphi(t)} e^{-i\alpha\varphi(0)} \rangle = \exp[J(t)]$ with

$$J(t) = \langle \alpha\varphi(t)\alpha\varphi(0) \rangle = \alpha^2 \int d\omega \frac{|z_\omega|^2}{\omega^2} K(\omega) [e^{-i\omega t} - 1]. \quad (3.5)$$

The impedance includes the dimensionless conductance $g_c \equiv \sum_n T_n$ of the conductor.

In the limit of $T = 0$ we find in agreement with results of Ref. [7, 8]

$$K(\omega) = g_c \{ FD(\omega + V) + (2 - 2F)D(\omega) + FD(\omega - V) \} + 2\operatorname{Re}\left\{\frac{1}{z_\omega}\right\} D(\omega), \quad (3.6)$$

with $D(\omega) \equiv -\omega\theta(-\omega)$ and the Fano factor $F \equiv \sum_n T_n(1 - T_n) / \sum_n T_n$. The first term in $K(\omega)$ ($\propto g_c$) represents the non-equilibrium current noise spectrum of the coherent conductor that vanishes for $\omega > V$. In physical terms this means that the highest energy ω an electron can emit traversing the conductor is exactly V . The second part represents the spectrum of

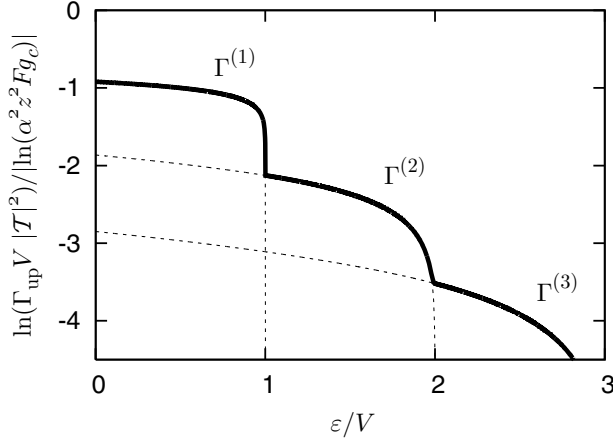


Figure 3.2. n -photon contributions (dashed) to the detector output. Each contribution dominates in the energy interval $(n - 1)V < \varepsilon < nV$. Subsequent contributions are suppressed by a factor $\approx \alpha^2 z^2 g_c F$. This is seen as a staircase structure in the log plot. The sum of all contributions is given by the solid line. To produce this plot, we took $z_\omega/\omega = z/V$, $z = 0.01$, $g_c F = 1.75$, $\alpha = 1$.

the environment. It is zero for $\omega > 0$, since the environment can only absorb energy at $T = 0$.

The time-dependent part of $J(t)$ is the Fourier transform of $K(\omega)|z_\omega|^2/\omega^2$ and $\Gamma(\varepsilon)$ is in turn the Fourier transform of $\exp[J(t)]$. If we expand $\exp[J(t)]$ in terms of $J(t)$, the n -th term presents the contribution of a process involving absorption of n photons in the detector. Such an n -photon process dominates in the interval $(n - 1)V < \varepsilon < nV$ and its contribution is proportional to α^{2n} .

The one-photon contribution gives $\Gamma_{\text{up}}^{(1)}/\Gamma_{\text{down}} \simeq z g_c F$. Each extra photon brings in a small factor, such that $\Gamma^{(n+1)}/\Gamma^{(n)} \simeq \alpha^2 z^2 g_c F$. This is seen as a staircase in the log plot presented in Fig. 3.2.

3.4 The non-quadratic part of the action

There is in general no justification for approximating $e^{-iS_{\text{cond}}}$ by a Gaussian. Indeed the non-quadratic part of the action describes interesting many-electron processes and are — as we show below — of the same order of magnitude. Since the path integral in (3.2) cannot be evaluated in

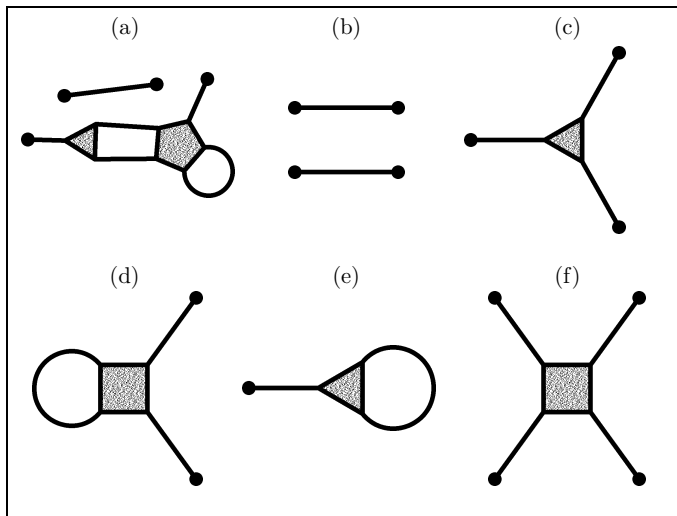


Figure 3.3. Typical Feynman diagrams appearing in the expansion of the path integral representation of the tunneling rate.

general, we proceed by perturbative expansion.

Indeed, since $|z| \ll 1$, the Gaussian part of the action, being proportional to z^{-1} , suppresses fluctuations in the path integral and we can treat the remaining part perturbatively. First we expand $-iS_{\text{cond}}[\phi]$ around $\phi = 0$. As mentioned previously (see the discussion below Eq. (3.5)), the first and second order terms just renormalize the impedance. The exponential of the remaining higher order terms is then again expanded in ϕ around $\phi = 0$. This expansion may be represented in terms of diagrams such as those in Fig. 3.3. Diagram (a) represents a high order term, from which the general structure becomes clear: Diagrams consist of lines, polygons and external vertices. The expansion contains not only connected diagrams, but all disconnected diagrams as well. A polygon with n vertices is associated with the symmetrized n -th order coefficient in the Taylor expansion of $-iS_{\text{cond}}[\phi]$ multiplied by a factor g_c . Lines represent propagators of ϕ corresponding to the Gaussian action with renormalized impedance. They are of order z making n -line diagrams z^n in leading order. External vertices (indicated by dots in the figure) are associated with the time-dependent linear term $i\alpha[-\varphi^+(0) + \varphi^-(t)]$ in Eq. (3.2). Thus a diagram with s external vertices gives a correction proportional to α^s .

Furthermore, diagrams without external vertices are time-independent and according to Eq. (3.1) contribute only to elastic tunneling processes. Diagrams (b) to (f) represent some of the lowest order terms in the expansion.

We consider transitions in the detector where energies between V and $2V$ are absorbed. In this interval, the detector output is given by diagrams (b), (c) and (d), which are proportional to α^4 , α^3 and α^2 respectively.

From the results presented in Fig. 3.2 we have learned that n -photon processes come with a coefficient α^{2n} . Hence the α^3 contribution has to arise from the interference term between a one- and a two-photon process: We disregard diagram (e) which only contributes to elastic processes. In the energy interval considered, the combined z^3 contribution of the included diagrams is zero and we obtain a tunneling rate that goes as $g_c^2 z^4$. Since a diagram like (f) has four lines, it could potentially contribute to the current with the same order in z . However, its contribution can only be proportional to g_c and is disregarded.

The expansion of S_{cond} up to fourth order terms and subsequent evaluation of the diagrams is straightforward but requires rather involved and lengthy calculations. Fortunately in the interval of interest the three contributions can be combined in a compact expression

$$\Gamma_{\text{up}} = 2|\mathcal{T}|^2 g_c^2 F^2 \int_{\varepsilon-V}^V d\omega (V - \omega)(\varepsilon - V - \omega) \frac{|z_\omega|^2}{\omega^2} \left| \frac{\alpha^2}{2} \frac{z_{\varepsilon-\omega}}{\varepsilon - \omega} + \alpha \frac{z_\varepsilon}{\varepsilon} \right|^2, \quad (3.7)$$

which is the main result of our work. The rate is proportional to the square of the zero-frequency current noise $S_{\text{cond}}(0) = \frac{2}{\pi} g_c F$.

The part proportional to α^4 (diagram b) represents a two-photon process originating from the quadratic part of S_{cond} and was already present in Fig. 3.2. We have thus shown that there are contributions of the same order resulting from non-linearities in the conductor. The α^2 term (diagram d) is the result of the two-electron and one-photon process expected from general reasoning presented in the introduction. We see that the α^3 term comes from the cross-term in the modulus square. This unambiguously identifies diagram (c) as the result of quantum interference of the two-electron process and the two-photon processes.

To understand this interference, we note that the photon modes involved are delocalized across the whole circuit. A photon in each mode can be absorbed in the detector as well as in the environment or the conductor. An elementary process is such that the final state differs from the initial state by two photons absorbed in two given modes. The final state can be

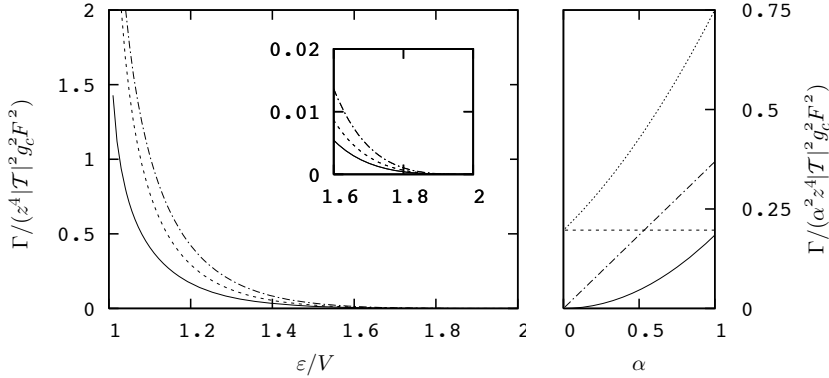


Figure 3.4. Left: Contributions to the detector output due to two-photon (solid), two-electron (dashed) processes and their interference (dash-dotted) at $\alpha = 0.8$ versus detector level splitting. The inset presents a zoom at $\varepsilon \rightarrow 2V$. Right: Different dependence on the coupling strength α enables experimental identification of these three contributions. The contributions and their sum (dotted) are plotted for $\varepsilon = 1.3V$.

reached by two routes: one with both photons absorbed in the detector and one with a photon absorbed in the detector and a photon absorbed in the environment. While the squares of these amplitudes represent the probabilities of two-photon and two-electron processes respectively, their cross-term gives rise to an interference contribution $\propto \alpha^3$.

The simplest concrete model is that of a frequency-independent impedance, $z_\omega = z$ at $\omega \simeq V$. The integration in Eq. 3.7 yields for the three distinct contributions ($i = 1, 2, 3$) ($\tilde{\varepsilon} = \varepsilon/V$, $1 < \tilde{\varepsilon} < 2$)

$$\frac{\Gamma_i}{z^4 |\mathcal{T}|^2 g_c^2 F^2} = \begin{cases} \alpha^4 \left[-\frac{2-2\tilde{\varepsilon}+\tilde{\varepsilon}^2}{\tilde{\varepsilon}^3} \ln(\tilde{\varepsilon}-1) - \frac{2-\tilde{\varepsilon}}{\tilde{\varepsilon}^2} \right] \\ 2\alpha^3 \left[-\frac{2-2\tilde{\varepsilon}+\tilde{\varepsilon}^2}{\tilde{\varepsilon}^3} \ln(\tilde{\varepsilon}-1) - \frac{2-\tilde{\varepsilon}}{\tilde{\varepsilon}^2} \right] \\ \alpha^2 \left[-\frac{2}{\tilde{\varepsilon}} \ln(\tilde{\varepsilon}-1) - \frac{4(2-\tilde{\varepsilon})}{\tilde{\varepsilon}^2} \right] \end{cases} \quad (3.8)$$

All contributions scale as $(\varepsilon - 2V)^3$ at the two-photon threshold and logarithmically diverge at the one-photon threshold $\tilde{\varepsilon} \sim 1$ (see Fig. 3.4). Eventually this divergence is cut-off in the close vicinity of $\varepsilon = eV$ at an energy scale gz^2eV where two-particle and one-photon rates become comparable.

Here, we have quantified the contributions for a very specific non-linear quantum noise source: a coherent conductor. However in the case of any unknown source of this kind the α -dependence of the contributions allows one to separate and identify them experimentally (right pane of Fig. 3.4). One would measure the detector output changing the coupling to the detector. Formally, three measurements at three different α are sufficient to determine the relative strength of all three contributions. In any case, in the limit of small coupling $\alpha \rightarrow 0$ the detector output is dominated by two-electron events. Further characterization may be achieved by engineering of a frequency-dependent impedance. For instance, setting $z(\omega = \epsilon)$ to 0 kills both the interference and the two-electron contribution.

3.5 Conclusion

To conclude, we have shown that the quantum tunneling detector in the energy interval specified is selectively sensitive to two-particle processes. The detector output is generally determined by three contributions: two-photon processes, two-electron processes and the interference of the two. These three sources can be distinguished experimentally by measuring at different couplings α to the detector. Our results thus facilitate the direct observation of many-particle events in the context of quantum transport.

Bibliography

- [1] Ya. M. Blanter and M. Büttiker, Phys. Rep. **336**, 1 (2000).
- [2] Yu. V. Nazarov (ed.), *Quantum Noise in Mesoscopic Physics*, NATO Science Series II: Vol 97, (Kluwer, Dordrecht, 2003).
- [3] A. D. Lorenzo and Yu. V. Nazarov, Phys. Rev. Lett. **94**, 210601 (2005).
- [4] C. W. J. Beenakker and M. Kindermann, Phys. Rev. Lett. **92**, 056801 (2004).
- [5] P. Samuelsson, E. V. Sukhorukov and M. Büttiker, Phys. Rev. Lett. **92**, 026805 (2004).
- [6] V. Cerletti, O. Gywat and D. Loss, Phys. Rev. B **72**, 115316 (2004).
- [7] U. Gavish, Y. Levinson and Y. Imry, Phys. Rev. B **62**, R10637 (2000).
- [8] R. Aguado and L. P. Kouwenhoven, Phys. Rev. Lett. **84**, 1986 (2000).
- [9] R. Deblock, E. Onac, L. Gurevich and L. P. Kouwenhoven, Science **301**, 203 (2003).
- [10] E. Onac, F. Balestro, L. H. W. Hartmann, Yu. V. Nazarov and L. P. Kouwenhoven, Phys. Rev. Lett. **96**, 176601 (2006).
- [11] G.-L. Ingold and Yu. V. Nazarov, in *Single Charge Tunneling*, edited by H. Grabert and M. Devoret, NATO ASI Series B294, (Plenum Press, New York, 1992).
- [12] M. Kindermann, Yu. V. Nazarov and C. W. J. Beenakker, Phys. Rev. B **69**, 035336 (2004).

- [13] J. Rammer and H. Smith, *Rev. Mod. Phys.* **58**, 323 (1986).
- [14] M. Kindermann, Yu. V. Nazarov and C. W. J. Beenakker, *Phys. Rev. Lett.* **90**, 2468051 (2003).
- [15] M. Kindermann and Yu. V. Nazarov, *Phys. Rev. Lett.* **91**, 136802 (2003).

Chapter 4

Polarization of a charge qubit strongly coupled to a voltage-driven quantum point contact

4.1 Introduction

The quantum point contact [1] has become a basic concept in the field of Quantum Transport owing to its simplicity. Its common experimental realization is a narrow constriction that connects two metallic reservoirs. An adequate theoretical description for this setup is a non-interacting one-dimensional electron gas interrupted by a potential barrier. The barrier is completely characterized by its scattering matrix. This enables the scattering approach to Quantum Transport [2].

Despite the correctness of the non-interacting electron description, truly many-body quantum correlations in a QPC do exist and are observable. These manifest themselves in the Full Counting Statistics (FCS) of electron transfers [3] and allow for detection of two-particle entanglement [4] through the measurement of non-local current correlations. This suggests that the observation of many-body effects in a QPC crucially relies on a proper detection scheme.

In this chapter, we probe a QPC with a charge qubit. Such a device has already been realized using single and double quantum dots. Previously, the QPC has been used as a detector of the qubit state [5, 6]. We propose

a scheme in which these roles are reversed. Provided the qubit and QPC are coupled strongly, switching between the qubit states is accompanied by severe Fermi-Sea shake-up in the QPC. The ratio of switching rates determines the qubit polarization. The d.c. current in the QPC reads the qubit polarization. Thereby we obtain information about the Fermi-Sea shake-up in the QPC.

For our results to apply, the qubit transition rate induced by the QPC should therefore dominate the rate due to coupling with other environmental modes. We estimate this requirement to be fulfilled already in the weak coupling regime.

Before analyzing the system in detail, the following qualitative conclusions can be drawn. The qubit owes its detection capabilities to the following fact: In order to be excited it has to absorb a quantum ε of energy from the QPC. Here ε is the qubit level splitting, a parameter that can be tuned easily in an experiment by means of a gate voltage. The QPC supplies the energy by transferring charge from the high voltage reservoir to the low voltage reservoir. The transfer of charge q allows qubit transitions for level splittings $\varepsilon < qV$, V being the bias voltage applied. Thus, the creation of excitations in the QPC is correlated with qubit switching.

We can assume that successive switchings of the qubit between its states $|1\rangle$ and $|2\rangle$ are rare and uncorrelated. The qubit dynamics are then characterized by the rates Γ_{21} to switch from state $|1\rangle$ to state $|2\rangle$ and Γ_{12} from $|2\rangle$ to $|1\rangle$. The stationary probability to find the qubit in state $|2\rangle$, or polarization for short, is determined by detailed balance to be $p_2 = \Gamma_{21}/(\Gamma_{12} + \Gamma_{21})$. The polarization can be observed experimentally by measuring the current in the QPC. The current displays random telegraph noise, switching between two values I_1 and I_2 . These correspond to the qubit being in the state $|1\rangle$ or $|2\rangle$ respectively. The d.c current I gives the average over many switches and is thus related to the stationary probability by $I = (1 - p_2)I_1 + p_2I_2$. The values of I_1 , I_2 and I are determined through measurement and p_2 is inferred.

When the QPC and qubit are weakly coupled [7, 8], a single electron is transferred [9]. This liberates at most energy eV , implying that the rate Γ_{21} is zero when $\varepsilon > eV$ and the rate Γ_{12} is zero when $\varepsilon < -eV$. The resulting p_2 changes from 1 to 0 upon increasing ε within the interval $-eV < \varepsilon < eV$. Cusps at $\varepsilon = \pm eV$ signify that the charge e is transferred. [See Fig. (2a)]

Guided by our understanding of weak coupling we can speculate as fol-

lows about what happens at stronger couplings. Apart from single electron transfers, we also expect the coordinated transfers of groups of electrons. A group of n electrons can provide up to neV of energy to the qubit. Therefore, peculiarities in p_2 should appear at the corresponding level splittings $\varepsilon = \pm neV$, $n = 1, 2, 3, \dots$ [10] However, it is not a priori obvious that these peculiarities are pronounced enough to be observed. The reason is the decoherence of the qubit states induced by electrons passing through the QPC. This smooths out peculiarities at the energy scale that is the inverse of the decoherence time. In the strong coupling regime, especially when the qubit couples to many QPC channels, the decoherence time is estimated to be short so that smoothing is severe. As a result, it is not clear whether peculiarities at neV are the dominant feature at strong coupling.

Therefore, strong coupling of the QPC and the qubit requires quantitative analysis. We have reduced the problem to the evaluation of a determinant of an infinite-dimensional Wiener-Hopf operator. We calculated the determinant numerically for a single channel QPC and found that peculiarities at multiples of eV are minute. Their contribution to p_2 does not exceed 10^{-4} and is seen only at logarithmic scale and at moderate couplings. Instead, far more prominent features occur at $\varepsilon = \frac{1}{2}eV$. General reasoning does not predict this. Straight-forward energy balance arguments suggest that a charge $e/2$ has been transferred between the QPC reservoirs. We are tempted to view this as a fractionally charged excitation generated by the qubit. However, the setup under consideration does not support an independent determination of the excitation charge. If we further increase the coupling, by adding channels to the QPC, we find a pseudo-Boltzmann distribution $p_2 = (1 + \exp(\lambda\varepsilon/k_B T^*))^{-1}$, with the effective temperature $k_B T^*$ of the order eV . All peculiarities disappear due to decoherence.

4.2 Model

Let us now turn to the details of our analysis. The system is illustrated in Fig. (4.1). The Hamiltonian for the system is

$$\hat{H} = \hat{T} + \hat{U}_1 |1\rangle \langle 1| + (\hat{U}_2 + \varepsilon) |2\rangle \langle 2| + \gamma(|1\rangle \langle 2| + |2\rangle \langle 1|). \quad (4.1)$$

The operator \hat{T} represents the kinetic energy of QPC electrons. The operator \hat{U}_k describes the potential barrier seen by QPC electrons when the qubit is in state $k = 1, 2$ and corresponds to a scattering matrix \hat{s}_k in

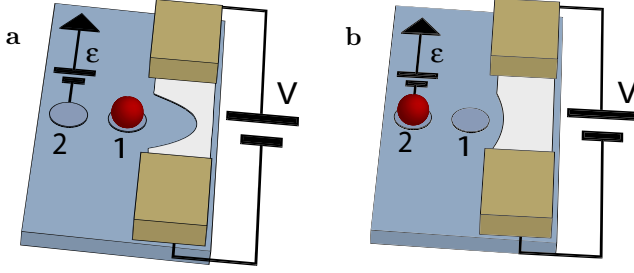


Figure 4.1. A schematic picture of the system considered. It consists of a charge qubit coupled to a QPC. The shape of the QPC constriction, and hence its scattering matrix, depends on the state of the qubit. The QPC is biased at voltage V . A gate voltage controls the qubit level splitting ε . There is a small tunneling rate γ between qubit states.

the scattering approach. QPC electrons do not interact directly with each other but rather with the qubit. This interaction is the only qubit relaxation mechanism included in our model. We work in the limit $\gamma \rightarrow 0$ where the inelastic transition rates $\Gamma_{12,21}$ between qubit states are small compared to the energies eV and ε . In this case, the qubit switching events can be regarded as independent and incoherent.

Now consider the qubit transition rate Γ_{21} . To lowest order in the tunneling amplitude γ it is given by

$$\Gamma_{21} = 2\gamma^2 \text{Re} \int_{-\infty}^0 d\tau e^{i\varepsilon\tau} \times \lim_{t_0 \rightarrow -\infty} \text{tr} \left[e^{i\hat{H}_2\tau} e^{-i\hat{H}_1(\tau-t_0)} \rho_0 e^{i\hat{H}_1(\tau-t_0)} \right]. \quad (4.2)$$

This is the usual Fermi Golden Rule. The Hamiltonians \hat{H}_1 and \hat{H}_2 are given by $\hat{H}_k = \hat{T} + \hat{U}_k$ and represent QPC dynamics when the qubit is held fixed in state $|k\rangle$. The trace is over QPC states, and ρ_0 is the initial QPC density matrix.

The evaluation of the integrand is a special case of a general problem in the extended Keldysh formalism [12]. The task is to evaluate the trace of a density matrix after “bra’s” have evolved with a time-dependent Hamiltonian $\hat{H}_-(t)$ and “kets” with a different Hamiltonian $\hat{H}_+(t)$.

$$e^{\mathcal{A}} = \text{tr} \left[\mathcal{T}^+ e^{-i \int_{-\infty}^{\infty} dt \hat{H}_+(t)} \rho_0 \mathcal{T}^- e^{i \int_{-\infty}^{\infty} dt \hat{H}_-(t)} \right]. \quad (4.3)$$

We implemented the scattering approach to obtain the general formula

$$\mathcal{A} = \text{tr} \ln \left[\hat{s}_- (1 - \hat{f}) + \hat{s}_+ \hat{f} \right] - \text{tr} \ln \hat{s}_-. \quad (4.4)$$

The operators \hat{s}_\pm and \hat{f} have both continuous and discrete indices. The continuous indices refer to energy, or in the Fourier transformed representation, to time. The discrete indices refer to transport channel space. The operators $\hat{s}_\pm = \hat{s}_\pm(t)\delta(t - t')$ are diagonal in time. The time-dependent scattering matrices $\hat{s}_\pm(t)$ describe scattering by the Hamiltonians $\hat{H}_\pm(t)$ at instant t . (It is the hall-mark of the scattering approach to express quantities in terms of scattering matrices rather than Hamiltonians.) The operator $\hat{f} = \hat{f}(E)\delta(E - E')$ is diagonal in the energy representation. The matrix $\hat{f}(E)$ is diagonal in channel space, representing the individual electron filling factors in the different channels. A derivation of Eq. (4.4) is given in Chapter 2 of this thesis. It generalizes similar relations published in Refs. [13, 14].

In order to apply the general result to Eq. (4.2), the time-dependent scattering matrices $\hat{s}_\pm(t)$ are chosen as $\hat{s}_+(t) = \hat{s}_1 + \theta(t - \tau)\theta(-t)(\hat{s}_2 - \hat{s}_1)$ and $\hat{s}_- = \hat{s}_1$. The QPC scattering matrices $\hat{s}_1(\hat{s}_2)$ with the qubit in the state 1(2) are the most important parameters of our approach.

Without a bias-voltage applied, the QPC-qubit setup exhibits the physics of the Anderson orthogonality catastrophe [15]. For the equilibrium QPC, the problem can be mapped [13] onto the classic Fermi Edge singularity (FES) problem [16, 17, 18]. In effect the authors of Ref. [13] computed \mathcal{A} in equilibrium. Our setup is simpler than the generic FES problem since there is no tunneling from the qubit to the QPC. As a result, out of all processes considered in Ref. [13], we only need the so-called closed loop diagrams. The relevant part of the FES result for our setup is an anomalous power law $\Gamma_{21}^{(0)}(\varepsilon) = \theta(-\varepsilon) \frac{1}{|\varepsilon|} \left(\frac{|\varepsilon|}{E_{\text{c.o.}}} \right)^\alpha$ for the equilibrium rate. Here $E_{\text{c.o.}}$ is an upper cutoff energy. The anomalous exponent α is determined by the eigenvalues of $\hat{s}_2^\dagger \hat{s}_1$ [19] as $\alpha = \frac{1}{4\pi^2} \left| \text{Tr} \ln^2(\hat{s}_f^\dagger \hat{s}_i) \right|$. The logarithm is defined on the branch $(-\pi, \pi]$. For a one or two channel point contact, $0 < \alpha < 1$.

4.3 Results

We now give the details of our calculation for the rates *out of equilibrium*. From Eq. (4.2) and Eq. (4.4) it follows that

$$\Gamma_{21}(\varepsilon) = |\gamma^2| \int_{-\infty}^{\infty} d\tau e^{-i\varepsilon\tau} \text{Det } \hat{Q}^{(V)}(\tau). \quad (4.5)$$

For positive times τ , the operator $\hat{Q}^{(V)}(\tau)$ is defined as [13]

$$\hat{Q}^{(V)}(\tau) = 1 + (\hat{s}_2^{-1} \hat{s}_1 - 1) \hat{\Pi}(\tau) \hat{f}^{(V)}, \quad (4.6)$$

while for negative τ , $\hat{Q}^{(V)}(\tau) = \hat{Q}^{(V)}(-\tau)^\dagger$. The time-interval operator $\hat{\Pi}(\tau) = \delta(t - t') \theta(t) \theta(\tau - t)$ is diagonal in time and acts as the identity operator in channel space for times $t = t' \in [0, \tau]$ and as the zero-operator outside this time-interval.

For the purpose of numerical calculation of the determinant we have to regularize $\hat{Q}^{(V)}(\tau)$. This is done by multiplying with the inverse of the zero-bias operator to define a new operator $\tilde{Q}(\tau) = \hat{Q}^{(0)}(\tau)^{-1} \hat{Q}^{(V)}(\tau)$. Its determinant is evaluated numerically. The rate $\Gamma_{21}(\varepsilon)$ at bias voltage V is then expressed as the convolution $\Gamma_{21}(\varepsilon) = \int \frac{d\varepsilon'}{2\pi} \Gamma_{21}^{\text{eq}}(\varepsilon - \varepsilon') \tilde{P}(\varepsilon')$ of the equilibrium rate and the Fourier transform of $\tilde{P}(\tau) = \text{Det } \tilde{Q}^{(V)}(\tau)$, that contains all effects of the bias voltage V .

We implemented this calculation numerically, and computed the probability p_2 to find the qubit in state $|2\rangle$. Details about the numerics can be found in Appendix 4.A Our main results are presented in Fig. (2). We used 2×2 scattering matrices parametrized by $\hat{s}_2^{-1} \hat{s}_1 = \exp(i\phi\sigma_x)$ and repeated the calculation for several $\phi \in [0, \pi]$. Small ϕ corresponds to weak coupling. The curve at $\phi = \pi/16$ is almost indistinguishable from the perturbative weak coupling limit discussed in the introduction. Cusps at $\pm eV$ indicate that qubit switching is accompanied by the transfer of single electrons in the QPC.

The increasing decoherence smooths the cusps for the curve at $\phi = \pi/4$ (2b). When the coupling is increased beyond $\phi = \pi/2$ steps appear at $\pm eV/2$ (c). Further increase of the coupling results in a sharpening of the steps (d).

Let us now briefly consider the limit of strong coupling where the qubit significantly affects the scattering in many QPC-channels. In this case, $\tilde{P}(\varepsilon)$ is approximately a Gaussian, $\tilde{P}(\varepsilon) \propto \exp\left(-\frac{\varepsilon^2}{2\beta(eV)^2}\right)$ with β a large

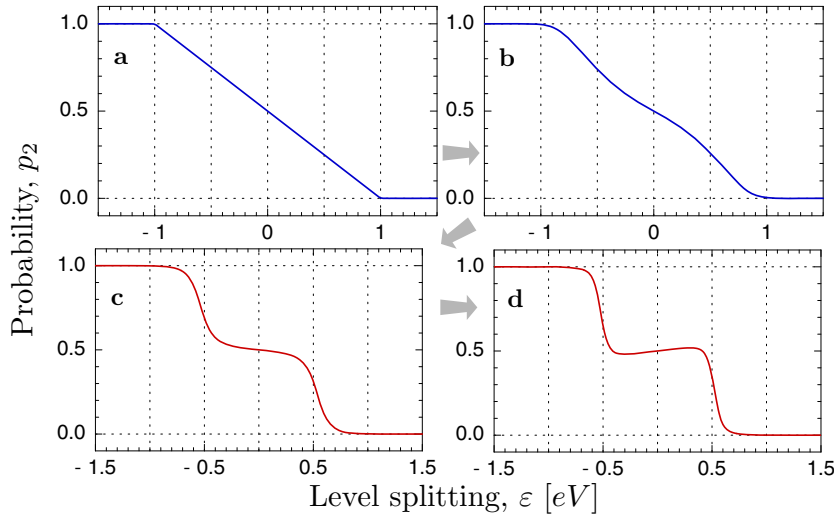


Figure 4.2. The probability p_2 that the qubit is in state $|2\rangle$ vs. level splitting ε . At weak coupling between the QPC and qubit, (Fig. **a**, **b**) the transfer of a single electron gives rise to cusps in p_2 at $\pm eV$. Peculiarities at $\pm eV/2$ (Fig. **c**, **d**) dominate the signal at strong coupling. Scattering matrices were parametrized as stated in the text. Fig. **a**, **b**, **c** and **d** respectively correspond to $\phi = \pi/16$, $\pi/4$, $7\pi/10$ and $4\pi/5$.

dimensionless number proportional to the number of channels. The interpretation of this is that electron fluctuations in the QPC affect the qubit level splitting. The typical fluctuation induced is $\delta\varepsilon \sim eV\sqrt{\beta}$. The frequency scale of the fluctuations is eV which is small compared to $\delta\varepsilon$. The fluctuations are therefore quasi-stationary. Their distribution are Gaussian by virtue of the central limit theorem. This leads to a pseudo-thermal polarization $p_2 = 1/(1 + \exp(\varepsilon/k_B T^*))$ where the effective temperature $k_B T^* = 2\sqrt{\beta/\alpha}eV$ is of the order of eV . The constant β is evaluated from numerics. For example, for $N \gg 1$ identical channels with scattering matrices $\exp(i\phi\sigma_x)$ and $\phi = 3\pi/4$ we find $\beta \approx N/7$ and effective temperature $\approx 0.36eV$. The added decoherence inherent in a many-channel QPC smooths out all peculiarities. Details of the calculation are presented in Appendix 4.B.

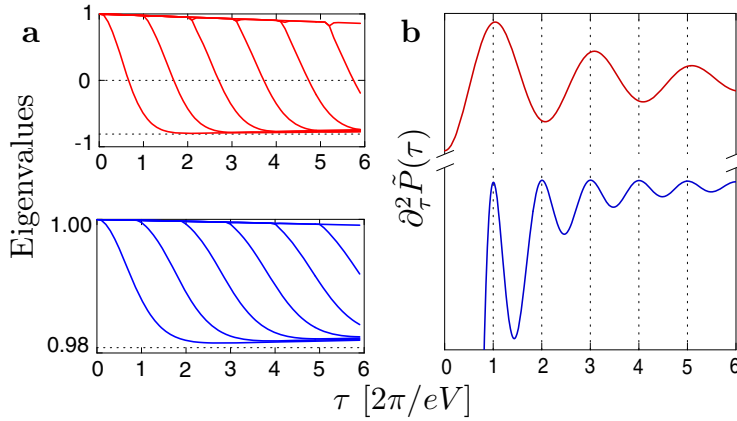


Figure 4.3. The behavior of eigenvalues (a) and the determinant $\tilde{P}(\tau)$ (b) at weak and strong QPC-qubit coupling respectively. The parameter ϕ in equals $4\pi/5$ (top) and $\pi/16$ (bottom) representing the strong and weak coupling limits respectively. Deviations from the correct asymptotics are due to finite size effects. Figure (b) contains the second derivative of $\tilde{P}(\tau) = \text{Det } \hat{Q}^{(0)}(\tau)^{-1} \hat{Q}^{(V)}(\tau)$. (The second derivative is taken to remove an average slope and curvature.)

4.4 Discussion

Let us speculate about the origin of the $\varepsilon = eV/2$ peculiarities. It would have been easy to explain peculiarities at $\varepsilon = neV$, $n = 2, 3, 4, \dots$ in $p_2(\varepsilon)$ as resulting from the transfer of multiple electrons. But for fractional peculiarities we have to turn to an indirect analogy with the model of interacting particles on a ring threaded by a magnetic flux [11]. There, one expects that the energy eigenvalues are periodic in flux with period of one flux quantum. However, the exact Bethe-Ansatz solution [11] reveals a *double* period of eigenvalues with adiabatically varying flux.

For our non-equilibrium setup, energy eigenvalues are not particularly useful. The natural eigenvalues to describe the phenomenon are those of the operator $\tilde{Q}^{(V)}(\tau)$. They depend on the parameter $eV\tau$ which is an analogue of flux. The product of the eigenvalues, i.e. the determinant $\tilde{P}(\tau)$ is not precisely periodic in τ since it decays at large τ owing to decoherence. Still, it oscillates and the period of these oscillations doubles as we go from weak to strong coupling (Fig. 3b). The doubling can be understood in terms of the transfer of the eigenvalues of $\tilde{Q}^{(V)}(\tau)$ upon increasing τ

(Fig. 3a) assuming the parametrization $\hat{s}_2^{-1}\hat{s}_1 = \exp(i\phi\sigma_x)$: In the large τ limit, energy-time uncertainty can be neglected in a “quasi-classical” approximation: The operator $\hat{\Pi}(\tau)$ projects onto a very long time interval, and is replaced by the identity operator. $\tilde{Q}^{(V)}$ becomes diagonal in energy. All eigenvalues that are not equal to 1 are concentrated in the transport energy window $0 < E < eV$ where the filling factors in the QPC reservoirs are not the same. For $\hat{s}_2^{-1}\hat{s}_1$ parametrized as above, these eigenvalues equal $\cos(\phi)$. There are $eV\tau/2\pi$ of them. In other words, the number of eigenvalues equal to $\cos\phi$ grows linearly with τ . Numerical diagonalization of $\tilde{Q}^{(V)}(\tau)$ (Fig. 3a) shows that one eigenvalue is transferred from 1 to $\cos(\phi)$ during time $2\pi/eV$. If $\cos(\phi) > 0$ as in the weak coupling case (bottom of Fig. 3b), this gives rise to $P(\tau)$ oscillations with frequency $eV/2\pi$ manifesting integer charges. However $\cos\phi$ becomes negative at stronger couplings, so that $P(\tau)$ changes sign with each eigenvalue transfer [Fig. 3b (top)]. Two eigenvalues have to transfer to give the same sign. The result is a period *doubling* of the oscillations in $\tilde{P}(\tau)$. This resembles the behavior of the wave vectors of the Bethe-Ansatz solution in Ref. [11].

The parametrization of the $\hat{s}_2^\dagger\hat{s}_1 = \exp(i\phi\sigma_x)$ is not general. However, the eigenvalue transfer arguments help to understand general scattering matrices. Eigenvalue transfer still occurs at frequency $eV/2\pi$ but instead of traveling along the real line, eigenvalues follow a trajectory inside the unit circle in the complex plane. Peculiarities at fractional level splittings $eV/2$ are pronounced if the end point of the trajectory has a negative real part. Numerical results for general scattering matrices are presented in Appendix 4.C.

Results presented so far are for “spinless” electrons. Spin degeneracy is removed by e.g. high magnetic field. If spin is included, but scattering remains spin independent, then two degenerate eigenvalues are transported simultaneously. In this case, the $eV/2$ peculiarities disappear for the parametrization $\exp(i\phi\sigma_x)$ but persists for more general scattering matrices. The results of further numerical work that confirm this are presented in Appendix 4.D.

4.5 Conclusion

We have studied a quantum transport setup that can easily be realized with current technology, namely that of a quantum point contact coupled to a charge qubit. The qubit is operated as a measuring device, its output

signal — the polarization p_2 — is directly seen in the QPC current. When the qubit is weakly coupled to the QPC, the dependence is dominated by processes where a single QPC electron interacts with the qubit. For intermediate couplings, the dependence shows peculiarities at level splittings $\pm eV/2$. These peculiarities are the result of many-body correlations induced in the QPC by qubit switching. Decoherence destroys these peculiarities in the limit where the qubit couples many QPC channels, leading to a pseudo-Boltzmann polarization with effective temperature $\sim eV$.

Appendix 4.A Numerical method

In this section we give a more detailed account of the numerical calculation of the qubit tunneling rates $\Gamma_{12}(\varepsilon)$ and $\Gamma_{21}(\varepsilon)$ than is presented in the main text. Our starting point is Eq. (7) of the main text. In order to discuss qubit transitions from $|1\rangle$ to $|2\rangle$ as well as the reverse transition simultaneously, we change notation slightly. In what follows, indices i and f refer to the initial and final state of the qubit respectively. We consider “forward” transitions $(f, i) = (2, 1)$ and “backward” transitions $(f, i) = (1, 2)$. The central object of numerical work is the operator

$$\hat{Q}_{fi}^{(V)}(\tau) = \begin{cases} 1 + (\hat{s}_i^\dagger \hat{s}_f - 1) \hat{\Pi}(-\tau) \hat{f}^{(V)}(E) & \tau < 0 \\ 1 + (\hat{s}_f^\dagger \hat{s}_i - 1) \hat{\Pi}(\tau) \hat{f}^{(V)}(E) & \tau > 0 \end{cases} . \quad (4.7)$$

We recall that the matrices \hat{s}_i and \hat{s}_f are the scattering matrices of QPC electrons when the qubit is in state i or f . $\hat{\Pi}(\tau)$ is a time-interval operator,

$$\hat{\Pi}(\tau)_{t\mu, t'\mu'} = \delta(t - t') \delta_{\mu, \mu'} \begin{cases} 1 & 0 < t < \tau \\ 0 & \text{otherwise} \end{cases} . \quad (4.8)$$

$\hat{f}^{(V)}(E)$ is diagonal in energy. It contains the filling factors of QPC-electrons in the various channels, including any bias voltage that may be present. Its form in the time-basis (at zero temperature) is given below in Eq. (4.15). The operator $\hat{Q}_{fi}^{(V)}(\tau)$ has an infinite number of eigenvalues outside the neighborhood of 1 in the complex plane. This implies that a regularization of the determinant is needed. Indeed, if one naively assumes the unregularized determinant to be well-defined and possessing the usual properties of determinants, such as $\text{Det}(AB) = \text{Det}(A)\text{Det}(B)$, one may show that $[\text{Det} \hat{Q}_{fi}^{(V)}(\tau)]^* = \text{Det} \hat{Q}_{if}^{(V)}(\tau)$. Were this true, it would have

implied that $\Gamma_{12}(\varepsilon) = \Gamma_{21}(\varepsilon)$. This cannot be correct. At low temperatures, the qubit is far more likely to emit energy than to absorb it, meaning that one of the two rates should dominate the other.

Regularization is achieved by multiplying with the inverse of the equilibrium operator. The operator $\tilde{Q}_{fi}(\tau) = \hat{Q}_{fi}^{(0)}(\tau)^{-1} \hat{Q}_{fi}^{(V)}(\tau)$ only has a finite number of eigenvalues for finite τ that are not in the neighborhood of 1, and so its determinant can be calculated numerically in a straightforward manner. (In this expression, $\hat{Q}_{fi}^{(0)}(\tau)$ is the operator Q when the QPC is initially in equilibrium, i.e. the bias voltage V is zero.) We therefore proceed as follows: We define

$$\tilde{P}(\tau) = \text{Det} \left[\hat{Q}_{21}^{(0)}(\tau)^{-1} \hat{Q}_{21}^{(V)}(\tau) \right], \quad (4.9)$$

and $\tilde{P}(\varepsilon) = \int d\tau e^{i\varepsilon\tau} \tilde{P}(\tau)$ as its Fourier transform. The equilibrium rate $\Gamma_{fi}^{\text{eq}}(\varepsilon)$ is known from the study of the Fermi Edge singularity. It is

$$\Gamma_{fi}^{\text{eq}}(\varepsilon) = |\gamma|^2 \theta(-\varepsilon_{fi}) \frac{1}{|\varepsilon|} \left| \frac{\varepsilon}{E_{\text{c.o.}}} \right|^\alpha, \quad (4.10)$$

where $\varepsilon_{fi} = \varepsilon$ if $(f, i) = (2, 1)$ and $\varepsilon_{fi} = -\varepsilon$ if $(f, i) = (1, 2)$. Furthermore $E_{\text{c.o.}}$ is a cut-off energy of the order of E_F and

$$\alpha = \frac{1}{4\pi^2} \left| \text{Tr} \ln^2(\hat{s}_f^\dagger \hat{s}_i) \right|. \quad (4.11)$$

The logarithm is defined on the branch $(-\pi, \pi]$. With the help of these definitions we have

$$\Gamma_{fi} = \int \frac{d\varepsilon'}{2\pi} \Gamma_{fi}^{\text{eq}}(\varepsilon') \tilde{P}(\varepsilon - \varepsilon'), \quad (4.12)$$

where our task is to calculate $\tilde{P}(\varepsilon)$ numerically.

The operator $\hat{Q}_{21}^{(V)}(\tau)$ will be considered in the time (i.e. Fourier transform of energy) basis. We restrict ourselves to the study of single channel QPC's, in which case the scattering matrices \hat{s}_1 and \hat{s}_2 are 2×2 matrices in QPC-channel space. We work in the standard channel space basis where

$$\hat{s}_k = \begin{pmatrix} r_k & t'_k \\ t_k & r'_k \end{pmatrix}, \quad (4.13)$$

with t, t' the left and right transmission amplitudes and r, r' the left and right reflection amplitudes. Because $\hat{\Pi}(\tau)$ is a projection operator that

commutes with the scattering matrices, we can evaluate the determinant in the space of spinor functions $\psi(t)$ defined on the interval $t \in [0, \tau]$. (We consider $\tau > 0$.) Then

$$\left[\hat{Q}_{21}^{(V)}(\tau) \psi \right](t) = \psi(t) + (\hat{s}_2^\dagger \hat{s}_1 - 1) \int_0^\tau dt' \hat{f}^{(V)}(t-t') \psi(t'), \quad (4.14)$$

where

$$\begin{aligned} \hat{f}^{(V)}(t) &= \int \frac{dE}{2\pi} e^{-iEt} \begin{pmatrix} \theta(-E) & 0 \\ 0 & \theta(eV - E) \end{pmatrix} \\ &= \frac{i}{2\pi(t + i0^+)} + i \left(\frac{1 - \hat{\sigma}_z}{2} \right) \frac{e^{-iteV} - 1}{2\pi t}, \end{aligned} \quad (4.15)$$

is the Fourier transform of the zero-temperature filling factors of the reservoirs connected to the QPC and 0^+ is an infinitesimal positive constant. Discretization of this operator proceeds as follows. We choose a time step $\Delta t \ll \tau$ such that $N = \tau/\Delta t$ is a large integer. We will represent $\hat{Q}_{21}^{(V)}(\tau)$ (and $Q_{21}^{(0)}(\tau)^{-1}$) as $2N \times 2N$ dimensional matrices. We define a dimensionless quantity $\eta = eV\Delta t$. $\tilde{P}(\tau)$ can only depend on τ in the combination τeV because there are no other time- or energy scales in the problem. We will therefore vary τ by keeping N fixed and varying η . Using the identity

$$\frac{1}{t \pm i0^+} = \mathcal{P} \left(\frac{1}{t} \right) \mp i\pi \delta(t), \quad (4.16)$$

we find a discretized operator

$$\begin{aligned} \left[1 + (\hat{s}_2^\dagger \hat{s}_1 - 1) \hat{\Pi} \hat{f} \right]_{kl} &= \delta_{kl} + (\hat{s}_2^\dagger \hat{s}_1 - 1) \left[\frac{1}{2} \delta_{kl} + \frac{1}{2\pi i(l-k)} (1 - \delta_{kl}) \right. \\ &\quad \left. + \frac{1 - \hat{\sigma}_z}{2} \underbrace{\left(\frac{\eta}{2\pi} \delta_{kl} + \frac{e^{i(l-k)\eta} - 1}{2\pi i(l-k)} (1 - \delta_{kl}) \right)}_{\text{nonequilibrium correction}} \right]. \end{aligned} \quad (4.17)$$

To test the quality of the discretization as well as its range of validity we do the following. When $\hat{s}_2^\dagger \hat{s}_1$ is close to identity, we can calculate $\tilde{P}(\tau)$ perturbatively, both for the original continuous operators and for its discretized approximation. If we take $\hat{s}_2^\dagger \hat{s}_1 = e^{i\phi \hat{\sigma}_x}$ then to order ϕ^2 we find

$$\tilde{P}_{\text{cont.}}(\tau) = 1 + 2 \left(\frac{\phi}{2\pi} \right)^2 \int_0^N dz \frac{\cos(z\eta) - 1}{z^2} (N - z), \quad (4.18)$$

where $\tau = N\eta/eV$ for the continuous kernel while for the discretized version we find

$$\tilde{P}_{\text{disc.}}(\eta) = 1 + 2 \left(\frac{\phi}{2\pi} \right)^2 \sum_{\zeta=1}^{N-1} \frac{\cos(\zeta\eta) - 1}{\zeta^2} (N - \zeta), \quad (4.19)$$

which indicates that the range of validity is $\eta \ll 2\pi$.

In practice we take $N = 2^8$. Larger N would demand the diagonalization of matrices that are too large to handle numerically. We find results suitably accurate up to $\eta = \pi/4$, thereby giving us access to $\tilde{P}(\tau)$ for $|\tau| \in [0, 64\pi/eV]$.

To summarize, the procedure for calculating the transition rates Γ_{21} and Γ_{12} is

1. For given scattering matrices \hat{s}_1 and \hat{s}_2 , calculate $\tilde{P}(\tau)$ numerically using the discrete approximations for the operators $\hat{Q}_{21}^{(V)}(\tau)$ and $\hat{Q}_{12}^{(0)}(\tau)$. Use a fixed large matrix size, and work in units $[\tau] = [eV]^{-1}$. Generate data for many positive values of τ .
2. Extend the results to negative τ by exploiting the symmetry $\tilde{P}(\tau) = \tilde{P}(-\tau)^*$, and Fourier transform the data.
3. Form the convolutions of Eq. 4.12 with the known equilibrium rates to obtain the non-equilibrium rates.

Appendix 4.B Many channels

To understand the behavior of the system when the QPC has many channels, the starting point is to consider the transfer of eigenvalues that make up the determinant $\tilde{P}(\tau)$. For an N channel QPC, N eigenvalues are simultaneously transferred to positions inside the unit circle in a time $2\pi/eV$. The initial velocity of each eigenvalue is zero, so that for small times τ , $\tilde{P}(\tau)$ is a Gaussian with peak-width $\sim 1/\sqrt{N}$. For many channels, it is therefore sufficient to consider small times only $\tau < \sim 1/\sqrt{N}eV$, leading to

$$\tilde{P}(\varepsilon) \propto \exp\left(-\frac{\varepsilon^2}{2\beta(eV)^2}\right), \quad (4.20)$$

with β proportional to the number of channels, and thus large. As explained in the main text, this can be understood as the result of quasi-

stationary Gaussian fluctuations of the qubit level splitting, induced by electron fluctuations in the QPC.

The expression for the qubit switching rate then reads

$$\Gamma(-\varepsilon) \propto \int_0^\infty d\varepsilon' \varepsilon'^\alpha \exp\left(-\frac{(\varepsilon - \varepsilon')^2}{2\beta(eV)^2}\right). \quad (4.21)$$

The Fermi-edge Singularity exponent α also scales like the number of channels, and is therefore large. We will now show that it is sufficient to do the integral in the saddle point approximation. First we find the maximal value of the integrand in the interval $\varepsilon' \in [0, \infty)$,

$$\varepsilon_{\text{opt}} = \frac{\varepsilon}{2} + \sqrt{\frac{\varepsilon^2}{4} + \alpha\beta(eV)^2}. \quad (4.22)$$

Then we rewrite

$$\begin{aligned} \varepsilon'^\alpha \exp\left(-\frac{(\varepsilon - \varepsilon')^2}{2\beta(eV)^2}\right) &= \varepsilon_{\text{opt}}^\alpha \exp\left(-\frac{(\varepsilon - \varepsilon_{\text{opt}})^2}{2\beta(eV)^2}\right) \\ &\times \exp\left[\underbrace{\frac{\omega^2}{2\beta(eV)^2} - \alpha \sum_{k=2}^{\infty} \frac{(-)^{k-1}}{k} \left(\frac{\omega}{\varepsilon_{\text{opt}}}\right)}_{\text{neglected}}\right], \end{aligned} \quad (4.23)$$

with $\varepsilon' = \varepsilon_{\text{opt}} + \omega$. The term marked by the underbrace can be neglected. The reason is that ε_{opt} is of the order $\sqrt{\alpha\beta}eV \sim NeV$ while the Gaussian term cuts off the ω integral at $\omega \sim \sqrt{\beta}eV \sim \sqrt{N}eV$. Consequently one finds

$$\Gamma(-\varepsilon) \propto \exp\left[-\frac{(\varepsilon - \varepsilon_{\text{opt}})^2}{2\beta(eV)^2} + \alpha \ln(\varepsilon_{\text{opt}})\right], \quad (4.24)$$

where it should be remembered that ε_{opt} depends on ε . In order to calculate the polarization $p_2(\varepsilon)$ we need to know $\Gamma(\varepsilon)$ and $\Gamma(-\varepsilon)$ for those energies ε where the one rate does not dominate the other. If we set

$$s = \sqrt{\frac{\varepsilon^2}{4} + \alpha\beta(eV)^2}, \quad (4.25)$$

then we find

$$\begin{aligned} \frac{\Gamma(-\varepsilon)}{\Gamma(\varepsilon)} &= \exp\left[\frac{s\varepsilon}{\beta(eV)^2} + \alpha \ln\left(\frac{2s + \varepsilon}{2s - \varepsilon}\right)\right] \\ &\simeq \exp\left[2\sqrt{\frac{\alpha}{\beta}} \frac{\varepsilon}{eV}\right] + \mathcal{O}\left(\frac{1}{N}\right). \end{aligned} \quad (4.26)$$

The last line was obtained by expanding in N^{-1} and recalling that $\alpha, \beta \sim N$. The polarization $p_2(\varepsilon)$ is then given by

$$p_2(\varepsilon) = \frac{1}{1 + \exp(2\sqrt{\alpha/\beta}\varepsilon/eV)}, \quad (4.27)$$

which is identical to the polarization of a qubit coupled to a reservoir at temperature $2\sqrt{\beta/\alpha}eV$.

Appendix 4.C Choice of scattering matrices

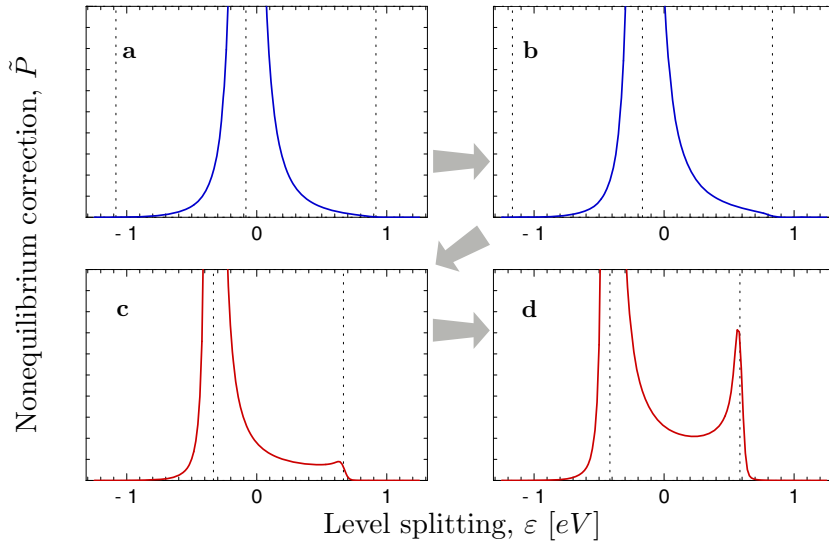


Figure 4.4. The function $\tilde{P}(\varepsilon)$ that contains the effect of the bias voltage V . As explained in the text, $\hat{s}_2^\dagger \hat{s}_1$ was parametrized as in Eq. (4.29). A value $\phi = \frac{\pi}{9}$ is used throughout. The values of θ in (a), (b), (c) and (d) are respectively $\frac{\pi}{6}$, $\frac{\pi}{3}$, $\frac{2\pi}{3}$ and $\frac{5\pi}{6}$. When $\theta < \pi/2$, then $\tilde{P}(\varepsilon)$ has a fairly symmetric peak centered at $-eV\theta/2\pi$. The tails of this peak vanish at $\varepsilon \simeq (-\theta/2\pi \pm 1)eV$. When $\theta > \pi/2$, there are two asymmetric peaks at $-eV\theta/2\pi$ and $(1 - \theta/2\pi)eV$. The value of $\tilde{P}(\varepsilon)$ is significantly larger for $\varepsilon \in [-eV\theta/2\pi, (1 - \theta/2\pi)eV]$ than outside this interval.

In the main text we confined our attention to the one parameter family

of scattering matrices

$$\hat{s}_2^\dagger \hat{s}_1 = \begin{pmatrix} \cos \phi & i \sin \phi \\ i \sin \phi & \cos \phi \end{pmatrix}. \quad (4.28)$$

For this choice, $\tilde{P}(\tau)$ is a real function of time. For $\theta < \pi/2$ its fluctuations are associated with energies $\sim \pm eV$ due to the transfer of eigenvalues from 1 to $\cos \phi$ at a rate of one per \hbar/eV . For $\phi > \pi/2$ however, $\cos \phi$ is negative and two eigenvalues have to be transferred before the sign of $\tilde{P}(\tau)$ returns to its initial value. The period of fluctuations of $\tilde{P}(\tau)$ doubles and becomes associated with energies $\pm eV/2$. Because $\tilde{P}(\tau)$ is real, the fluctuations with positive and negative energies are equal: $\tilde{P}(\varepsilon) = \tilde{P}(-\varepsilon)$. This translates into the following feature of the probability p_2 to find the qubit in state $|2\rangle$. For $\phi < \pi/2$, $p_2(\varepsilon)$ changes from 1 to 0 in an energy interval of length $2eV$. For $\phi > \pi/2$, this interval shrinks to eV . The boundary of the interval is defined more sharply the closer ϕ is to 0 or π , where decoherence happens slowly.

Since the QPC scattering matrices contain parameters that are not under experimental control, it is relevant to ask how the results are altered when a more general choice

$$\hat{s}_2^\dagger \hat{s}_1 = \begin{pmatrix} e^{-i\theta} \cos \phi & i \sin \phi \\ i \sin \phi & e^{i\theta} \cos \phi \end{pmatrix}, \quad (4.29)$$

with $\phi \in [-\frac{\pi}{2}, \frac{\pi}{2}]$ and $\theta \in [0, \pi]$ is made for the scattering matrices. With this choice, eigenvalues travel from 1 to $e^{i\theta} \cos \phi$ at a rate of one per \hbar/eV . This means that the period doubling of $\tilde{P}(\tau)$ no longer takes place. The phase of $\tilde{P}(\tau)$ does not return to its original value after the transfer of two eigenvalues. Rather, one expects fluctuations associated with an energy $(n - \frac{\theta}{2\pi})eV$, $n = 0, \pm 1, \pm 2, \dots$. Because $\tilde{P}(\tau)$ is no longer real, positive and negative frequencies don't contribute equally. However, while the eigenvalue trajectories lie close to the real line, one can expect results similar to those obtained for real $\tilde{P}(\tau)$. We obtained numerical results for four scattering matrices of the form (4.29). We chose $\theta = \frac{1}{6}\pi, \frac{1}{3}\pi, \frac{2}{3}\pi$ and $\frac{5}{6}\pi$. To sharpen abrupt features we chose $\phi = \pi/9$ so that the exponential decay of $\tilde{P}(\tau)$ is associated with a long decoherence time: $\simeq 0.06\hbar/eV$. As depicted in Fig. (4.4), we found $\tilde{P}(\varepsilon)$ to behave as follows. For θ close to zero, $\tilde{P}(\varepsilon)$ consists of one peak situated at $\varepsilon = -\frac{\theta}{2\pi}eV$. The tails of this peak vanish at $\varepsilon = (\pm 1 - \frac{\theta}{2\pi})eV$. The closer to zero that θ is taken, the more abrupt this behavior of the tails become. As θ is increased, a

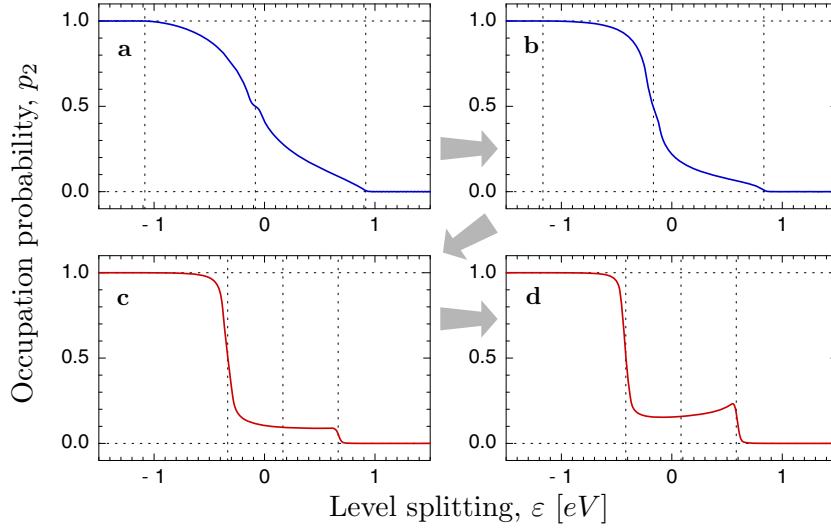


Figure 4.5. The qubit polarization $p_2(\varepsilon)$. $s_2^\dagger s_1$ is chosen as in Fig. (4.4): A value $\phi = \frac{\pi}{9}$ is used throughout. The values of θ in (a), (b), (c) and (d) are respectively $\frac{\pi}{6}$, $\frac{\pi}{3}$, $\frac{2\pi}{3}$ and $\frac{5\pi}{6}$. When $\theta < \pi/2$, the occupation probability p_2 is significantly different from its asymptotic values 0 and 1 in an ε interval of $2eV$. When $\theta > \pi/2$, this interval shrinks to eV . The boundaries of the interval are more sharply defined the closer θ is to $\pi/2$.

second peak starts appearing at $\varepsilon = (1 - \frac{\theta}{2\pi}) eV$. When $\theta = \pi$, the height (and width) of this peak exactly equals that of the peak at $-\frac{\theta}{2\pi} eV$. In the interval $\varepsilon \in [-\frac{\theta}{2\pi} eV, (1 - \frac{\theta}{2\pi}) eV]$ that is bounded by the peaks, $\tilde{P}(\tau)$ is significantly larger than in the region outside the peaks. This behavior of $\tilde{P}(\varepsilon)$ translates into the occupation probabilities $p_2(\varepsilon)$ depicted in Fig. (4.5). For $\theta < \pi/2$, $p_2(\varepsilon)$ still changes from unity to zero in an interval of length $2eV$ while for $\theta > \pi/2$ the interval shrinks to eV . The closer θ moves to 0 or π , the sharper the interval becomes defined. We therefore conclude that the peculiarities reported on in the main text is not confined to the special choice (4.28) of scattering matrices.

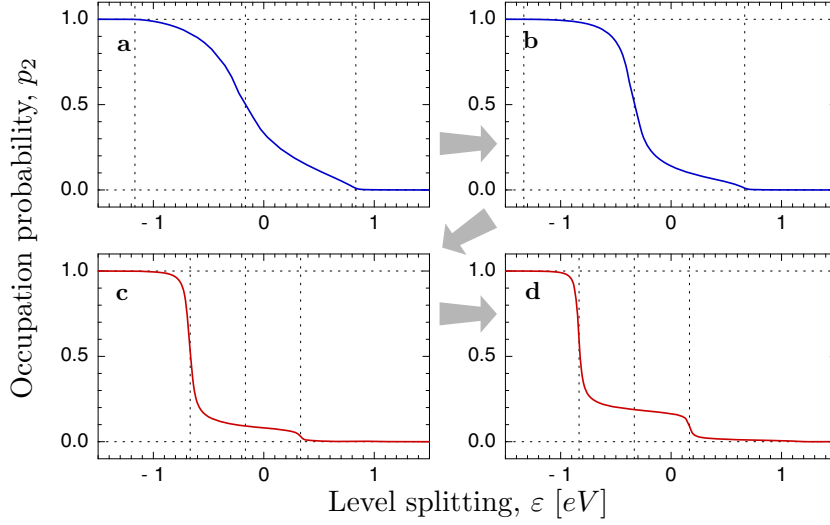


Figure 4.6. The probability $p_2(\varepsilon)$ with spin included. $\hat{s}_2^\dagger \hat{s}_1$ is chosen as in Fig. (4.4) and (4.5): A value $\phi = \frac{\pi}{9}$ is used throughout. The values of θ in (a), (b), (c) and (d) are respectively $\frac{\pi}{6}$, $\frac{\pi}{3}$, $\frac{2\pi}{3}$ and $\frac{5\pi}{6}$. The $eV/2$ peculiarities are still clearly visible for $\theta > \pi/2$.

Appendix 4.D Inclusion of spin

Up to this point we have considered spinless electrons in the QPC. In this section we investigate the effect of including spin. We still take the interaction between the QPC and the qubit to be spin independent. However, the mere existence of a spin degree of freedom for QPC electrons doubles the dimension of channel space. The narrowest QPC now has two channels instead of one and $\tilde{P}_{s=\frac{1}{2}}(\tau) = \tilde{P}_{s=0}(\tau)^2$, i.e. the determinant $\tilde{P}_{s=\frac{1}{2}}(\tau)$ with spin included is the square of the determinant $\tilde{P}_{s=0}(\tau)$ without spin. For real determinants, squaring kills the phase. This means that the observed period doubling for the parametrization of Eq. (4.28) disappears and with it the $\varepsilon = eV/2$ peculiarities of p_2 . However, the peculiarities survive for more general scattering matrices due to the fact that, for $\theta \neq 0$, $\tilde{P}_{s=0}(\varepsilon)$ has two peaks with different heights. Suppose the relative peak heights are A and $1 - A$, i.e.

$$\tilde{P}_{s=0}(\tau) \sim (1 - A)e^{i\frac{\theta}{2\pi}eV\tau} + Ae^{-(1-\frac{\theta}{2\pi})eV\tau}, \quad (4.30)$$

where A is a real number between 0 and $\frac{1}{2}$. ($A = 0$ corresponds to $\theta = 0$ while $A = \frac{1}{2}$ corresponds to $\theta = \pi$.) It follows that $P_{s=\frac{1}{2}}(\varepsilon)$ has three peaks at

1. $\varepsilon = -2\frac{\theta}{2\pi}eV$ with height $(1 - A)^2$,
2. $\varepsilon = (1 - 2\frac{\theta}{2\pi}) eV$ with height $2A(1 - A)$,
3. and $\varepsilon = (2 - 2\frac{\theta}{2\pi}) eV$ with height A^2 .

As long as A is small, i.e. θ is not too close to π , the first two peaks will dominate the third, and the signature $eV/2$ peculiarities may still be observable in $p_2(\varepsilon)$. Fig. (4.6), contains p_2 calculated for the same scattering matrices as in Fig. (4.5), but with spin included. The cases when $\theta = \frac{2}{3}\pi$ and $\theta = \frac{5}{6}\pi$ still contain clear peculiarities. For θ very close to π (not shown) these features disappear.

Bibliography

- [1] B. J. Van Wees, H. van Houten, C. W. J. Beenakker, J. G. Willimson, L. P. Kouwenhoven, D. van der Marel and C. T. Foxon, *Phys. Rev. Lett.* **60**, 848 (1988).
- [2] M. Büttiker, *Phys. Rev. B* **41**, 7906 (1990).
- [3] L. S. Levitov, H. Lee and G. H. Lesovik, *J. Math. Phys.* **37**, 4845 (1996).
- [4] C. W. J. Beenakker, C. Emary and M. Kindermann, *Phys. Rev. Lett.* **91**, 147901 (2003).
- [5] J. M. Elzerman, R. Hanson, J. S. Greidanus, L. H. Willems van Beveren, S. Se Franceschi, L. M. K. Vandersypen, S. Tarucha and L. P. Kouwenhoven, *Phys. Rev. B* **67**, 161308(R) (2003).
- [6] J. R. Petta, A. C \gt Johnson, C. M. Marcus, M. P. Hanson and A. C. Gossard, *Phys. Rev. Lett.* **93**, 186802 (2004).
- [7] I. L. Aleiner, N. S. Wingreen and Y. Meir, *Phys. Rev. Lett.* **79**, 3740 (1997).
- [8] Y. Levinson, *Europhys. Lett.* **39**, 299 (1997)
- [9] E. Onac, F. Balestro, L. H. W. Hertmann, Yu. V. Nazarov and L. P. Kouwenhoven, *Phys. Rev. Lett.* **96**, 176601 (2006).
- [10] J. Tobiska, J. Danon, I. Snyman and Yu. V. Nazarov, *Phys. Rev. Lett.* **96**, 096801 (2006). This thesis, Chapter 3.
- [11] B. Sutherland and B. S. Shastry, *Phys. Rev. Lett.* **65**, 1833 (1990).
- [12] Yu. V. Nazarov and M. Kindermann, *Euro. Phys. J. B* **35**, 413 (2003).

- [13] D. A. Abanin and L. S. Levitov, Phys. Rev. Lett. **93**, 126802 (2004).
- [14] D. A. Abanin and L. S. Levitov, Phys. Rev. Lett. **94**, 186803 (2005).
- [15] P. W. Anderson, Phys. Rev. Lett. **24**, 1049 (1967).
- [16] G. D. Mahan, Phys. Rev. **163**, 612 (1967).
- [17] P. Nozières and C. T. De Dominicis, Phys. Rev. **178**, 1097 (1969).
- [18] K. A. Matveev and A. I. Larkin, Phys. Rev. B **46**, 15337 (1992).
- [19] K. Yamada and K. Yosida, Prog. Th. Phys. **68**, 1504 (1982).

Chapter 5

Ballistic transmission through a graphene bilayer

5.1 Introduction

Undoped graphene has no free electrons, so an infinite sample cannot conduct electricity. A finite sample can conduct, because electrons injected at one end can be transmitted a distance L to the other end via so-called evanescent modes. These are modes that decay $\propto e^{-L/\lambda}$ with a penetration depth λ bounded from above by the width W of the sample. For a wide and narrow sample ($W \gg L$), there are many evanescent modes that contribute appreciably to the conductance. Because the transmission of an electron via an evanescent mode is a stochastic event, the current fluctuates in time — even in the absence of any scattering by impurities or lattice defects. Tworzydło et al. [1] found that the shot noise produced by the evanescent modes in an undoped carbon monolayer (of length $L \ll$ width W) is *pseudo-diffusive*: The Fano factor $F = P/2e\bar{I}$ (ratio of noise power P and time-averaged current \bar{I}) has the same value $F = 1/3$ as in a diffusive metal (while $F = 1$ for independent current pulses) [2].

A carbon bilayer has an additional length scale, not present in the monolayer of Ref. [1], namely the interlayer coupling length l_{\perp} . It is an order of magnitude larger than the interatomic distance d within the layer: [3, 4, 5]

$$l_{\perp} = \frac{\hbar v}{t_{\perp}} = \frac{3t_{\parallel}}{2t_{\perp}} d \approx 11 d \quad (5.1)$$

(with $v \approx 10^6$ m/s, $d \approx 1.4 \text{ \AA}$ and $t_{\parallel} \approx 3 \text{ eV}$, respectively the carrier ve-

locity, interatomic distance and nearest-neighbour hopping energy within a single layer and $t_{\perp} \approx 0.4$ eV the nearest-neighbour hopping energy between two layers [6]). Since L is typically large compared to l_{\perp} , the two layers are strongly coupled. In this chapter we investigate what is the effect of interlayer coupling on the average current and shot noise.

The model and calculation are outlined in Secs. 5.2 and 5.3. Our main conclusion, presented in Sec. 5.4, is that an undoped graphene bilayer has the same current and noise as two monolayers in parallel. The Fano factor, therefore, still equals $1/3$ when the Fermi level coincides with the Dirac point (at which conduction and valence bands touch). However, the interval $\Delta E_F \simeq \hbar v l_{\perp} / L^2$ in Fermi energy around the Dirac point where this pseudo-diffusive result holds is much narrower, by a factor l_{\perp} / L , in a bilayer than it is in a monolayer.

Our results for the mean current \bar{I} , and hence for the conductance in a ballistic system, agree with those of Cserti, [7] but differ from two other recent calculations in a (weakly) disordered system [8, 9]. (The shot noise was not considered in Refs. [7, 8, 9].) A ballistic system like ours was studied recently by Katsnelson, [12] with different results for both conductance and shot noise. We discuss the origin of the difference in Sec. 5.5. We conclude by connecting with experiments [11] in Sec. 5.6.

5.2 Model

We use the same setup as in Refs. [1, 10], shown schematically in Fig. 5.1. A sheet of ballistic bilayer graphene in the $x - y$ plane contains a weakly doped strip of width W and length L and heavily doped contact regions for $x < 0$ and $x > L$. The doping is controlled by gate voltages, which induce a potential profile of the form

$$U(x) = \begin{cases} -U_{\infty} & \text{if } x < 0 \text{ or } x > L, \\ 0 & \text{if } 0 < x < L. \end{cases} \quad (5.2)$$

We use an abrupt potential step for simplicity, justified by the fact that any smoothing of the step over a distance small compared to L becomes irrelevant near the Dirac point, when the Fermi wave length $\gtrsim L$.

While Refs. [1, 10] considered a graphene monolayer, governed by the 2×2 Dirac Hamiltonian, here we take a bilayer with 4×4 Hamiltonian

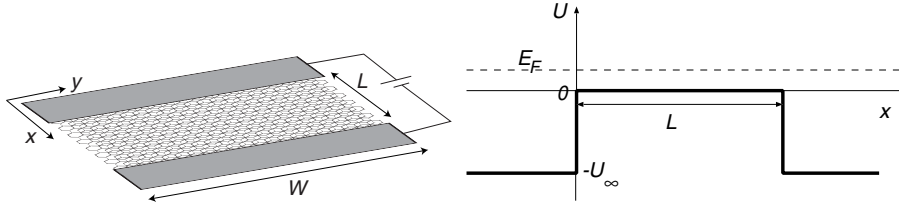


Figure 5.1. Schematic of the graphene bilayer. Left: Two stacked honeycomb lattices of carbon atoms in a strip between metal contacts. Right: Variation of the electrostatic potential across the strip.

[3, 4, 5]

$$H = \begin{pmatrix} U & v(p_x + ip_y) & t_{\perp} & 0 \\ v(p_x - ip_y) & U & 0 & 0 \\ t_{\perp} & 0 & U & v(p_x - ip_y) \\ 0 & 0 & v(p_x + ip_y) & U \end{pmatrix}, \quad (5.3)$$

with $\mathbf{p} = -i\hbar\partial/\partial\mathbf{r}$ the momentum operator. The Hamiltonian acts on a four-component spinor $(\Psi_{A_1}, \Psi_{B_1}, \Psi_{B_2}, \Psi_{A_2})$ with amplitudes on the A and B sublattices of the first and second layer. Only nearest-neighbor hopping is taken into account, either from A to B sites within a layer or between different layers. (Sites from the same sublattice but on different layers are not directly adjacent.) The Hamiltonian (5.3) describes low-energy excitations near one of the two Dirac points in the Brillouin zone, where conduction and valence bands touch. The other Dirac point and the spin degree of freedom contribute a four-fold degeneracy factor to current and noise power.

We have taken the same electrostatic potential U in both layers. In general, the potentials will differ, [13, 14] but to study the special physics of undoped graphene it is necessary that they are both tuned to the Dirac point of each layer. This can be achieved by separate top and bottom gates (not shown in Fig. 5.1).

For free electrons in bilayer graphene, the relation between energy ε and total momentum $k = (k_x^2 + k_y^2)^{1/2}$ as described by this Hamiltonian consists of four hyperbolas, defined by

$$\varepsilon = \pm \frac{1}{2}t_{\perp} \pm \sqrt{\frac{1}{4}t_{\perp}^2 + k^2}, \quad (5.4a)$$

$$\varepsilon = \mp \frac{1}{2}t_{\perp} \pm \sqrt{\frac{1}{4}t_{\perp}^2 + k^2}, \quad (5.4b)$$

plotted in Fig. 5.2. (For notational convenience, we use units such that $\hbar v = 1$ in most equations.)

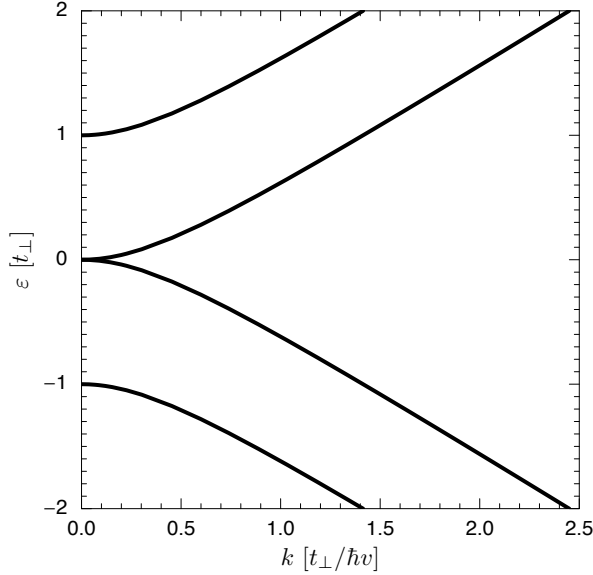


Figure 5.2. Energy spectrum (5.4) of the graphene bilayer, according to the Hamiltonian (5.3).

We calculate the transmission matrix \mathbf{t} through the graphene strip at the Fermi energy, and then obtain the conductance and noise power from the Landauer-Büttiker formulas [2]

$$G = G_0 \text{Tr } \mathbf{t} \mathbf{t}^\dagger, \quad P = P_0 \text{Tr } \mathbf{t} \mathbf{t}^\dagger (1 - \mathbf{t} \mathbf{t}^\dagger), \quad (5.5)$$

$$\rightarrow F = \frac{\text{Tr } \mathbf{t} \mathbf{t}^\dagger (1 - \mathbf{t} \mathbf{t}^\dagger)}{\text{Tr } \mathbf{t} \mathbf{t}^\dagger}, \quad (5.6)$$

with $G_0 = 4e^2/h$, $P_0 = 2e|V|G_0$ and V the voltage applied between the contact regions. The results depend on the degree of doping in the graphene strip (varied by varying E_F), but they become independent of the degree of doping of the contact regions if $U_\infty \gg t_\perp$.

5.3 Transmission probabilities

We calculate the transmission matrix by matching eigenstates of the Hamiltonian (5.3) at the two interfaces $x = 0$ and $x = L$. This procedure is similar to a calculation of non-relativistic scattering by a rectangular barrier in a two-dimensional waveguide. There are two differences. Firstly, the Hamiltonian (5.3) is a first-order differential operator, and hence only the wavefunction and not its derivative is continuous at the interface. Secondly, the spectrum contains both positive and negative energy eigenstates.

The eigenstates of H for $U = 0$ have been given in Ref. [13]. They may be characterized as follows. For given energy ε and transverse momentum k_y , we define two longitudinal momenta

$$k_{x\pm} = \sqrt{(\varepsilon \pm \frac{1}{2}t_{\perp})^2 - \frac{1}{4}t_{\perp}^2 - k_y^2}. \quad (5.7)$$

The square root is taken with argument in the interval $[0, \pi)$. Associated with each real k_{x+} there are two propagating modes, one left-going $\phi_{\varepsilon,+}^L$ and one right-going $\phi_{\varepsilon,+}^R$. Two more propagating modes $\phi_{\varepsilon,-}^L$ and $\phi_{\varepsilon,-}^R$ are associated with each real k_{x-} . The eigenstates of H are

$$\phi_{\varepsilon,\pm}^R(x, y) = N_{\pm} \begin{pmatrix} \mp\varepsilon \\ \mp k_{x\pm} \pm ik_y \\ \varepsilon \\ k_{x\pm} + ik_y \end{pmatrix} e^{i(k_{x\pm}x + k_y y)}, \quad (5.8a)$$

$$\phi_{\varepsilon,\pm}^L(x, y) = N_{\pm} \begin{pmatrix} \mp\varepsilon \\ \pm k_{x\pm} \pm ik_y \\ \varepsilon \\ -k_{x\pm} + ik_y \end{pmatrix} e^{i(-k_{x\pm}x + k_y y)}, \quad (5.8b)$$

with $N_{\pm} = (4W\varepsilon k_{x\pm})^{-\frac{1}{2}}$ a normalization constant such that each state carries unit current

$$I = ev \int_0^W dy \phi^\dagger \begin{pmatrix} \sigma_x & 0 \\ 0 & \sigma_x \end{pmatrix} \phi, \quad (5.9)$$

in the positive or negative x -direction.

For each k_y we have two left-incident scattering states $\psi_{\varepsilon,\pm}$ at energy ε . In the region $x < 0$ to the left of the strip they have the form

$$\psi_{\varepsilon,\pm} = \phi_{\varepsilon+U_{\infty,\pm}}^R + r_{\pm}^{\pm}(\varepsilon, k_y) \phi_{\varepsilon+U_{\infty,+}}^L + r_{\pm}^{\pm}(\varepsilon, k_y) \phi_{\varepsilon+U_{\infty,-}}^L, \quad (5.10)$$

while to the right of the strip ($x > L$) one has

$$\psi_{\varepsilon, \pm} = t_{\pm}^{\pm}(\varepsilon, k_y) \phi_{\varepsilon+U_{\infty}, \pm}^R + t_{\pm}^{\mp}(\varepsilon, k_y) \phi_{\varepsilon+U_{\infty}, \mp}^R. \quad (5.11)$$

For $\varepsilon \neq 0$ the form of the solution in the region $x \in [0, L]$ is self-evidently a linear combination of the four solutions $\phi_{\varepsilon\pm}^L, \phi_{\varepsilon\pm}^R$. Care must however be taken in analytical work to use proper linear combinations of these modes that remain linearly independent exactly at $\varepsilon = 0$ (the Dirac point). (See Appendix 5.A explicit formulas.)

The four transmission amplitudes t_{\pm}^{\pm} for given ε and k_y can be combined in the transmission matrix

$$\mathbf{t}(\varepsilon, k_y) = \begin{pmatrix} t_{+}^{+}(\varepsilon, k_y) & t_{-}^{+}(\varepsilon, k_y) \\ t_{+}^{-}(\varepsilon, k_y) & t_{-}^{-}(\varepsilon, k_y) \end{pmatrix}. \quad (5.12)$$

We consider a short and wide geometry $L \ll W$, in which the boundary conditions in the y -direction become irrelevant. For simplicity, we take periodic boundary conditions, such that k_y is quantized as $k_{y,n} = 2\pi n/W$, $n = 0, \pm 1, \pm 2, \dots$. In the regime $L \ll W$, $|\varepsilon| \ll U_{\infty}$ considered here, both the discreteness of the modes in the contact region can be ignored. As a consequence, the traces in Eqs. (5.5) and (5.6) may be replaced by integrals through the prescription

$$\text{Tr}(\mathbf{t}\mathbf{t}^{\dagger})^p \rightarrow \frac{W}{\pi} \int_0^{\infty} dk_y \sum_{\sigma=\pm} [T_{\sigma}(E_F, k_y)]^p, \quad (5.13)$$

where T_{\pm} are the two eigenvalues of $\mathbf{t}\mathbf{t}^{\dagger}$.

5.4 Results

Fig. 5.3 contains a grey-scale plot of the total transmission probability $\text{Tr}(\mathbf{t}\mathbf{t}^{\dagger})$ as a function of k_y and ε . Darkly shaded regions indicate resonances of high transmission, similar to those found in Ref. [15].

The location ε_{res} of resonances can be estimated by equating $k_x L/\pi$ to an integer n . This yields the curves

$$\varepsilon_{\text{res}}^{(n)}(k_y) = \mp \frac{1}{2} t_{\perp} \pm \sqrt{\frac{1}{4} t_{\perp}^2 + \left(\frac{\pi n}{L}\right)^2 + k_y^2}, \quad (5.14)$$

indicated in the figure by dashed lines. It is seen that good agreement is reached for $|k_y| \ll 1/L$ and again for $|k_y| \gg 1/L$. For $|k_y L| \simeq 1$ there is

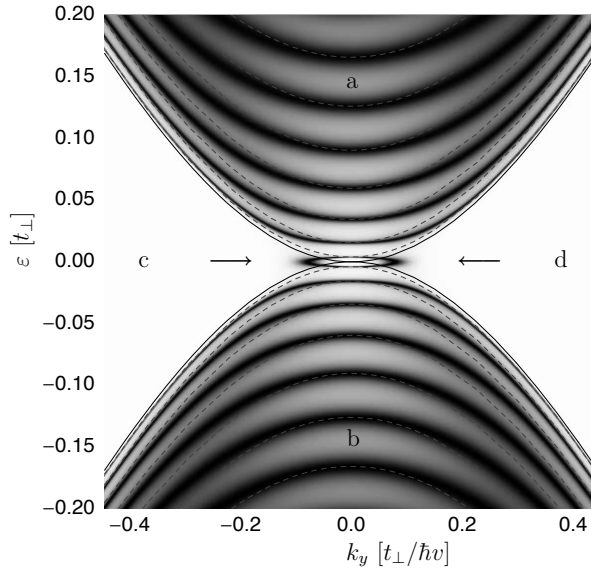


Figure 5.3. Total transmission probability $\text{Tr}(\mathbf{t}\mathbf{t}^\dagger)$ as a function of ε and k_y for $U_\infty = 50 t_\perp$ and $L = 50 l_\perp$. Darkly shaded regions indicate high transmission. Grey dashed lines indicate the estimate (5.14) for the occurrence of resonances in regions (a) and (b), while solid lines indicate the boundary between propagating and evanescent modes. Arrows point to the resonances of evanescent modes close to the Dirac point, responsible for the pseudo-diffusive transport.

a cross over. In regions (c) and (d), demarkated by the curves $\varepsilon_{\text{res}}^{(0)}$, the transmission generally drops to zero, since in these regions the longitudinal momentum k_x is imaginary.

There is however a curious feature close to $\varepsilon, k_y = 0$. The resonance closest to the Dirac point behaves differently from all the other resonances. When $|k_y|$ is increased, it moves closer to the Dirac point rather than away from it, eventually crossing into regions (c) and (d) of evanescent modes. It is this resonance of evanescent modes that is responsible for the pseudo-diffusive transport at the Dirac point.

At $\varepsilon = 0$, the exact formula for the eigenvalues of $\mathbf{t}\mathbf{t}^\dagger$ in the $U_\infty \rightarrow \infty$

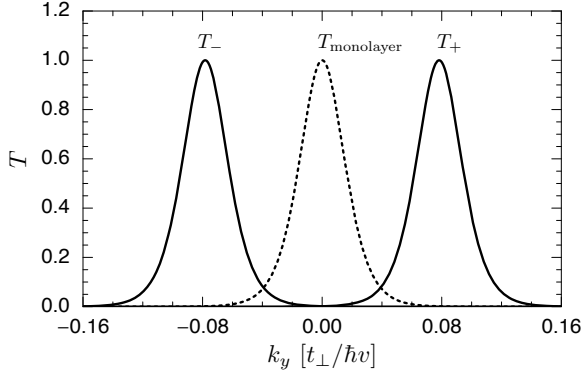


Figure 5.4. Solid curves: Transmission coefficients T_{\pm} of the bilayer according to Eq. (5.15) at $L = 50 l_{\perp}$. These coefficients are displaced copies of the monolayer result (dashed).

limit is

$$T_{\pm}(\varepsilon = 0, k_y) = \frac{1}{\cosh^2(k_y \mp k_c)L}, \quad (5.15)$$

$$k_c = \frac{1}{L} \sinh^{-1} \left(\frac{L}{2l_{\perp}} \right). \quad (5.16)$$

In Fig. 5.4 the two transmission coefficients $T_{\pm}(0, k_y)$ are compared to the single transmission coefficient $T_{\text{monolayer}}(0, k_y) = 1/\cosh^2(k_y L)$ of the monolayer [1, 10]. Details of the calculation may be found in Appendix 5.A.

Since the two bilayer coefficients are displaced copies of the monolayer coefficient, any observable of the form $A = \text{Tr } f(\mathbf{t}\mathbf{t}^{\dagger})$, with f an arbitrary function is twice as large in a bilayer as it is in a monolayer. From Eqs. (5.5) and (5.13) we obtain

$$G_{\text{bilayer}} = 2G_{\text{monolayer}} = \frac{2G_0}{\pi} \frac{W}{L}, \quad (5.17)$$

$$P_{\text{bilayer}} = 2P_{\text{monolayer}} = \frac{4e|V|G_0}{3\pi} \frac{W}{L}, \quad (5.18)$$

$$F_{\text{bilayer}} = F_{\text{monolayer}} = \frac{1}{3}. \quad (5.19)$$

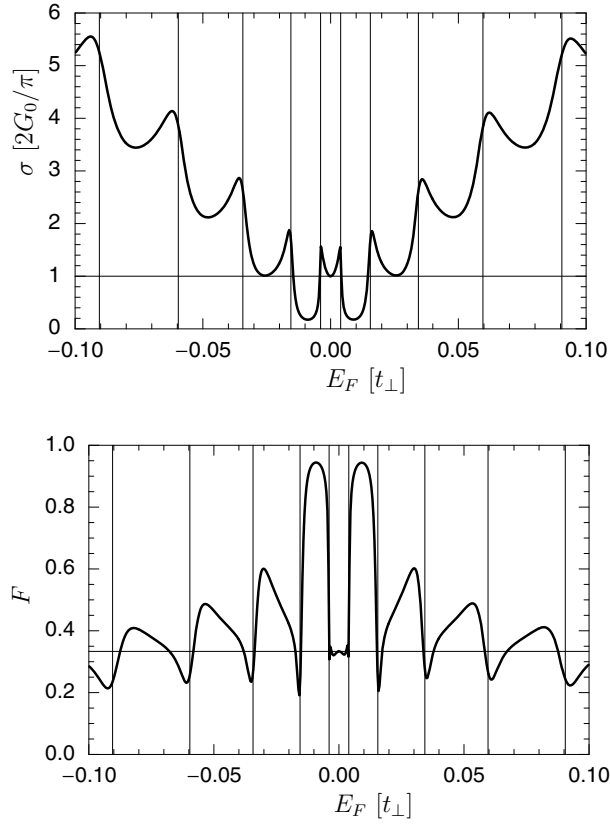


Figure 5.5. Conductivity σ (top) and Fano factor F (bottom) of the bilayer, as a function of the Fermi energy E_F measured from the Dirac point for $U_\infty = 50 t_\perp$ and $L = 50 l_\perp$. Abrupt features occur at $E_F \simeq \varepsilon_{\text{res}}^{(n)}(k_y = 0)$ [vertical lines, given by Eq. (5.20)].

Figure 5.5 contains plots of both the conductivity $\sigma = GL/W$ and Fano factor of the bilayer around the Dirac point. At energies associated with resonances at normal incidence,

$$\varepsilon_{\text{res}}^{(n)}(0) = \pm \frac{\pi^2 \hbar v}{L} \left[\frac{l_{\perp}}{L} n^2 + \mathcal{O}(l_{\perp}/L)^3 \right], \quad (5.20)$$

the conductivity and Fano factor show abrupt features. The width $\Delta E_F = 2\varepsilon_{\text{res}}^{(1)} = 2\pi^2 \hbar v l_{\perp}/L^2$ of the energy window between the resonances that straddle the Dirac point in the bilayer is smaller by a factor l_{\perp}/L than in the monolayer.

5.5 Dependence on the potential in the contact region

So far we have assumed that the potential U_{∞} in the contact region is large compared to the band splitting t_{\perp} near the Dirac point of the graphene bilayer. We believe that this is the appropriate regime to model a normal metal contact to the graphene sheet, which couples equally well to the two sublattices on each layer.

It is of interest to determine how large the ratio U_{∞}/t_{\perp} should be to reach the contact-independent limit of the previous section. Note that for $U_{\infty} > t_{\perp}$ there are two left-incident propagating modes in the leads for each ε and k_y . When U_{∞} becomes smaller than t_{\perp} one of the two modes becomes evanescent, leading to an abrupt change in the conductivity and the Fano factor. This is evident in Fig. 5.6. For $U_{\infty} - t_{\perp} \gtrsim \hbar v/L$, the conductivity and Fano factor have almost reached their $U_{\infty} \rightarrow \infty$ limits. For $U_{\infty} \lesssim t_{\perp}$ the conductivity is smaller and the Fano factor larger than when $U_{\infty} > t_{\perp}$. Both quantities vanish when the Fermi momentum $\sqrt{U_{\infty} t_{\perp}}/v$ in the contact region drops below \hbar/L and the contact region is effectively depleted of carriers.

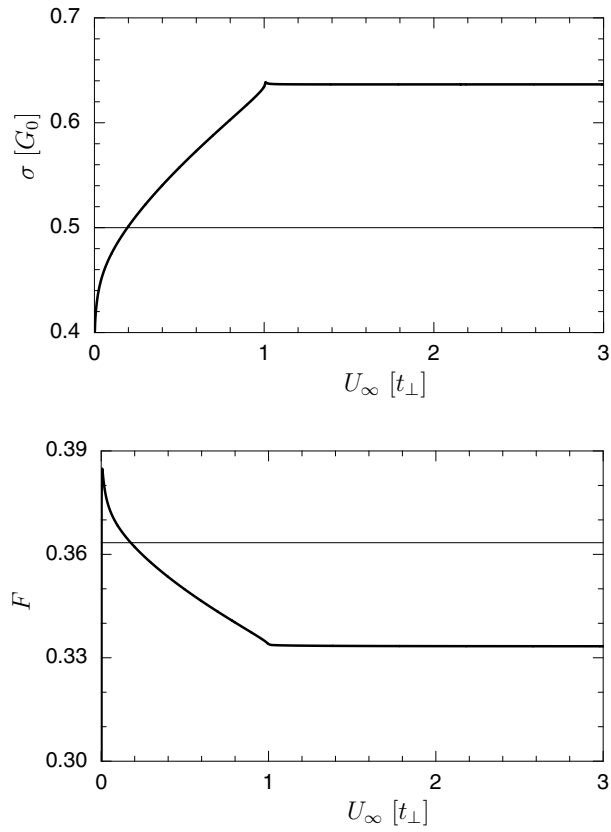


Figure 5.6. Dependence of the conductivity and Fano factor at the Dirac point on the potential U_∞ in the contact region, for $L = 100 l_\perp$. Thin horizontal lines indicate the values of Ref. [12]. The values obtained in this chapter correspond to a plateau reached for $U_\infty/t_\perp \gtrsim 1$.

These finite- U_∞ results can be used to make contact with the previous calculation of Katsnelson [12], who found a conductivity $\sigma = G_0/2$ and a Fano factor $F = 1 - 2/\pi$ at the Dirac point, in the regime $\hbar v/L \ll \sqrt{U_\infty t_\perp} \ll t_\perp$. These values are indicated in Fig. 5.6 by horizontal lines. The intersection point with our curves occurs at nearly the same value of U_∞/t_\perp for both quantities. The intersection point moves closer and closer to $U_\infty = 0$ as the sample length L is increased, but there is no clear plateau around the intersection point. Moreover, as shown in the Appendix, the intersection point does not correspond to a minimum or maximum as a function of the Fermi energy, so that these values would be difficult to extract from a measurement.

We do believe that the results of Ref. [12] describe the asymptotic limit $L/l_\perp \rightarrow \infty$ at $E_F \equiv 0$, however, because in this limit the width $\Delta E_F \simeq \hbar v l_\perp / L^2$ of the resonance at the Dirac point vanishes, it seems unobservable.

5.6 Conclusion

In conclusion, we have demonstrated that the pseudo-diffusive transport at the Dirac point, discovered in Ref. [1] for a carbon monolayer, holds in a bilayer as well. All moments of the current fluctuations have the same relation to the mean current as in a diffusive metal. In particular, the Fano factor has the 1/3 value characteristic of diffusive transport, even though the bilayer is assumed to be free of impurities or lattice defects.

Although we found that an undoped bilayer transmits as two undoped monolayers in parallel, the two systems behave very different away from charge neutrality. The resonance of evanescent modes around the Dirac point of zero Fermi energy has width $\Delta E_F \simeq \hbar v l_\perp / L^2$ in a bilayer, which is smaller than the width in a monolayer by the ratio of the interlayer coupling length l_\perp and the separation L of the metal contacts.

Since $l_\perp \approx 1.5$ nm, one would not be able to resolve this resonance in the μm -size samples of Ref. [11]. These experiments found no qualitative difference in the conductance-versus-gate-voltage dependence of monolayer and bilayer graphene, both showing a minimum conductivity at the Dirac point of G_0 . Smaller junctions in the 10–100 nm range as are now being fabricated should make it possible to resolve the transmission resonance of evanescent modes predicted here, and to observe the unusual pseudo-diffusive dynamics associated with it.

Appendix 5.A Transmission eigenvalues

In this Appendix we give some detail of the calculation that leads to the transmission coefficients $T_{\pm}(\varepsilon = 0, k_y)$ of Eq. (5.15). At the Dirac point and in the limit of large U_{∞} , the left-incident eigenstates of the Hamiltonian (5.3) are of the form

$$\psi_{\pm}(x) = \begin{cases} e^{ik_y y} [\xi_{\pm}^R e^{iU_{\infty} x} + (r_{+}^{\pm} \xi_{+}^L + r_{-}^{\pm} \xi_{-}^L) e^{-iU_{\infty} x}] & x < 0, \\ e^{ik_y y} [(c_1^{\pm} \chi_1 + c_2^{\pm} \chi_2) e^{k_y x} + (c_3^{\pm} \chi_3 + c_4^{\pm} \chi_4) e^{-k_y x}] & 0 < x < L, \\ e^{ik_y y} e^{iU_{\infty}(x-L)} [t_{+}^{\pm} \xi_{+}^R + t_{-}^{\pm} \xi_{-}^R] & x > L, \end{cases} \quad (5.21)$$

with the definitions

$$\xi_{\pm}^R = \begin{pmatrix} \mp 1 \\ \mp 1 \\ 1 \\ 1 \end{pmatrix}, \quad \xi_{\pm}^L = \begin{pmatrix} \mp 1 \\ \pm 1 \\ 1 \\ -1 \end{pmatrix}, \quad (5.22)$$

$$\chi_1 = \begin{pmatrix} 0 \\ 1 \\ 0 \\ 0 \end{pmatrix}, \quad \chi_2 = \begin{pmatrix} 0 \\ -it_{\perp} x \\ 1 \\ 0 \end{pmatrix}, \quad \chi_3 = \begin{pmatrix} 1 \\ 0 \\ 0 \\ -it_{\perp} x \end{pmatrix}, \quad \chi_4 = \begin{pmatrix} 0 \\ 0 \\ 0 \\ 1 \end{pmatrix}. \quad (5.23)$$

These eigenstates must be continuous at $x = 0$ and $x = L$, leading to an 8×8 system of linear equations $M\mathbf{b}_{\pm} = \mathbf{c}_{\pm}$ with

$$M = \begin{pmatrix} 1 & -1 & 0 & 0 & 1 & 0 & 0 & 0 \\ -1 & 1 & 1 & 0 & 0 & 0 & 0 & 0 \\ -1 & -1 & 0 & 0 & 0 & 1 & 0 & 0 \\ 1 & 1 & 0 & 1 & 0 & 0 & 0 & 0 \\ 0 & 0 & 0 & 0 & 1 & 0 & z & -z \\ 0 & 0 & z & -iLt_{\perp} z & 0 & 0 & 1 & -1 \\ 0 & 0 & 0 & z & 0 & 0 & -1 & -1 \\ 0 & 0 & 0 & 0 & -iLt_{\perp} & 1 & -z & -z \end{pmatrix}, \quad (5.24)$$

and

$$\mathbf{b}_{\pm} = (r_{+}^{\pm}, r_{-}^{\pm}, c_1, c_2, c_3, c_4, t_{+}^{\pm}, t_{-}^{\pm})^T, \quad (5.25a)$$

$$\mathbf{c}_{\pm} = (\mp 1, \mp 1, 1, 1, 0, 0, 0, 0)^T. \quad (5.25b)$$

We abbreviated $z = e^{k_y L}$. By solving these equations, one finds the transmission matrix

$$\mathbf{t} = \frac{2i}{2 + (L/l_\perp)^2 + 2 \cosh(2k_y L)} \times \begin{pmatrix} (L/l_\perp - 2i) \cosh(k_y L) & (L/l_\perp) \sinh(k_y L) \\ -(L/l_\perp) \sinh(k_y L) & -(L/l_\perp + 2i) \cosh(k_y L) \end{pmatrix}. \quad (5.26)$$

The eigenvalues of $\mathbf{t}\mathbf{t}^\dagger$ are then given by Eq. (5.15).

Appendix 5.B Four- vs. two-band Hamiltonian

In this Appendix we verify that the difference in the results obtained here and in Ref. [12] is to the different order of limits in the two calculations. In Ref. [12] the limit $t_\perp \rightarrow \infty$ was taken at the beginning of the calculation, i.e. before the potential in the leads U_∞ was sent to infinity. This reduces the 4×4 Hamiltonian (5.3) to the effective 2×2 Hamiltonian [4]

$$H_{\text{eff}} = -\frac{v^2}{t_\perp} \begin{pmatrix} 0 & (p_x - ip_y)^2 \\ (p_x + ip_y)^2 & 0 \end{pmatrix} + U(x) \begin{pmatrix} 1 & 0 \\ 0 & 1 \end{pmatrix}. \quad (5.27)$$

Only the two lowest bands near the Dirac point are retained in H_{eff} , as is appropriate for the regime $U_\infty \ll t_\perp$.

We have repeated the calculation of conductance and Fano factor using both Hamiltonians (5.3) and (5.27), for parameter values corresponding to the intersection point of Fig. 5.6, and find good agreement (see Fig. 5.7). The implication is that the result of Ref. [12] is applicable in the $t_\perp \gg U_\infty$ regime.

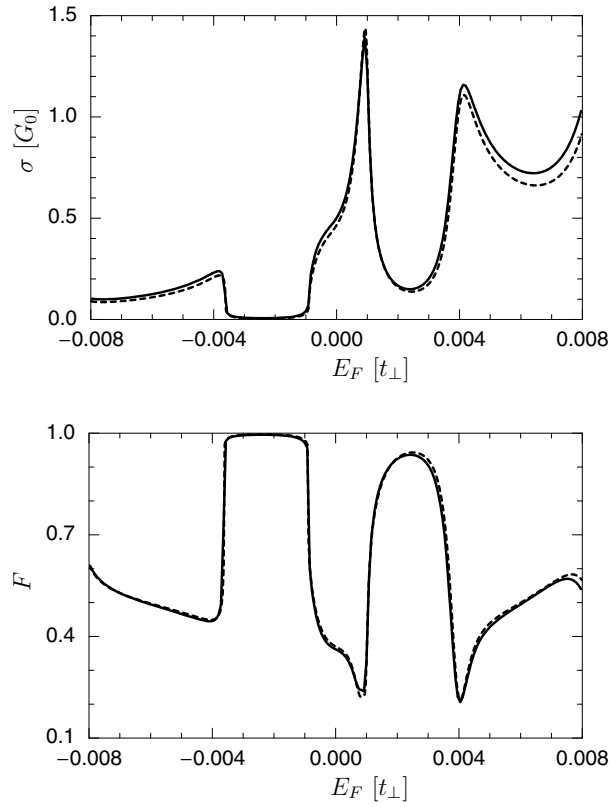


Figure 5.7. Conductivity (top) and Fano factor (bottom) around the Dirac point, for $L = 100 l_{\perp}$ and $U_{\infty} = 0.2 t_{\perp}$. (These parameter values correspond to the intersection point of our curves with the prediction of Ref. [12] in Fig. 5.6.) The solid lines were obtained using the four-band Hamiltonian (5.3), while the dashed lines were obtained from the two-band Hamiltonian (5.27).

Bibliography

- [1] J. Tworzydło, B. Trauzettel, M. Titov, A. Rycerz and C. W. J. Beenakker, Phys. Rev. Lett. **96**, 246802 (2006).
- [2] For a review and a tutorial on shot noise we refer, respectively, to: Ya. M. Blanter and M. Büttiker, Phys. Rep. **336**, 1 (2000); C. W. J. Beenakker and C. Schönberger, Physics Today **56** (5), 37 (2003).
- [3] P. R. Wallace, Phys. Rev. **71**, 622 (1947).
- [4] E. McCann and V. I. Fal'ko, Phys. Rev. Lett. **96**, 086805 (2006).
- [5] J. Nilsson, A. H. Castro Neto, N. M. R. Peres and F. Guinea, Phys. Rev. B **73**, 214418 (2006).
- [6] This value of the interlayer coupling strength γ_1 refers to graphite; the value for a bilayer is not yet known.
- [7] J. Cserti, Phys. Rev. B **75**, 033405 (2007).
- [8] M. Koshino and T. Ando, Phys. Rev. B **73**, 245403 (2006).
- [9] J. Nilsson, A. H. Castro Neto, F. Guinea and N. M. R. Peres, Phys. Rev. Lett. **97**, 266801 (2006).
- [10] M. I. Katsnelson, Euro. Phys. J. B **51**, 157 (2006).
- [11] K. S. Novoselov, E. McCann, S. V. Morozov, V. I. Fal'ko, M. I. Katsnelson, U. Zeitler, D. Jiang, F. Schedin and A. K. Geim, Nature Physics **2**, 177 (2006).
- [12] M. I. Katsnelson, Euro. Phys. J. B **52**, 151 (2006).
- [13] J. Nilsson, A. H. Castro Neto, F. Guinea and N. M. R. Peres, Phys. Rev. B **76** (2007).

- [14] E. McCann, *Phys. Rev. B* **74**, 161403(R) (2006).
- [15] M. I. Katsnelson, K. S. Novoselov and A. K. Geim, *Nature Physics* **2**, 620 (2006).

Chapter 6

Valley-isospin dependence of the quantum Hall effect in a graphene p - n junction

6.1 Introduction

Recent experiments [1, 2, 3] have succeeded in fabricating junctions between p -doped and n -doped graphene, and have begun to investigate the remarkable properties predicted theoretically [4, 5, 6, 7]. The conductance G of a p - n junction measures the coupling of electron-like states from the conduction band to hole-like states from the valence band, which in graphene is unusually strong because of the phenomenon of Klein tunneling [4, 5].

In the zero-magnetic field regime of Huard et al. [1] this coupling depends on the length scales characteristic of the p - n interface. In the high-magnetic field regime of Williams, DiCarlo, and Marcus, [2] the p - n junction has a quantized conductance, which has been explained by Abanin and Levitov [7] as the series conductance $G_{\text{series}} = G_p G_n / (G_p + G_n)$ of the quantum Hall conductances G_p, G_n in the p -doped and n -doped regions (each an odd multiple of the conductance quantum $G_0 = 2e^2/h$). (The p - n - p junction experiments of Özyilmaz et al. [3] are also explained in terms of a series conductance.)

These results apply if the system is sufficiently large that mesoscopic fluctuations in the conductance can be ignored, either as a consequence of self-averaging by time dependent electric fields or as a consequence of

suppression of phase coherence by inelastic scattering [7]. In a sufficiently small system mesoscopic conductance fluctuations as a function of Fermi energy are expected to appear. In particular, in the quantum Hall effect regime, the conductance of a p - n junction is expected to fluctuate around the series conductance G_{series} in a small conductor (nanoribbon) at low temperatures.

In this chapter we show that a plateau in the conductance versus Fermi energy survives in the case of fully phase coherent conduction without intervalley scattering. When both p -doped and n -doped regions are on the lowest Hall plateau ($G_p = G_n = G_0$), we find a plateau at

$$G = \frac{1}{2}G_0(1 - \cos \Phi), \quad (6.1)$$

with Φ the angle between the valley isospins at the two edges of the nanoribbon. A random electrostatic potential is not effective at producing mesoscopic conductance fluctuations, provided that it varies slowly on the scale of the lattice constant — so that it does not induce intervalley scattering. The dispersionless edge state that may exist at a zigzag edge (and connects the two valleys at opposite edges) is an intrinsic source of intervalley scattering when the edge crosses the p - n interface. The angle Φ that determines the conductance plateau can be varied by straining the carbon lattice, either systematically to shift the plateau up or down, or randomly to produce a bimodal statistical distribution of the conductance in an armchair nanoribbon.

Our analysis was inspired by an analogy between edge channel transport of Dirac fermions along a p - n interface [7] and along a normal-superconducting (NS) interface [8]. The analogy, explained in Fig. 6.1, is instructive, but it is only a partial analogy — as we will see. We present analytical results, obtained from the Dirac equation, as well as numerical results, obtained from a tight-binding model on a honeycomb lattice. We start with the former.

6.2 Analytical theory

The Dirac equation for massless two-dimensional fermions reads

$$\tau_0 \otimes [v(\mathbf{p} + e\mathbf{A}) \cdot \boldsymbol{\sigma} + U]\Psi = E\Psi, \quad (6.2)$$

where E is the energy, v the Fermi velocity, $\mathbf{p} = (\hbar/i)(\partial/\partial x, \partial/\partial y)$ the canonical momentum operator in the x - y plane of the graphene layer, $U(x)$

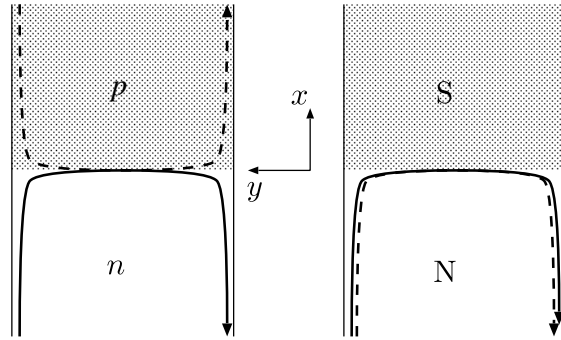


Figure 6.1. Schematic top view of a graphene nanoribbon containing an interface between an n -doped and p -doped region (left panel) and between a normal (N) and superconducting (S) region (right panel). Electron-like and hole-like edge states in the lowest Landau level are indicated by solid and dashed lines, respectively, with arrows pointing in the direction of propagation. The electron-like and hole-like valley-polarized edge states hybridize along the p - n or NS interface to form a valley-degenerate electron-hole state. The two-terminal conductance $G = G_0 T_{eh}$ is determined by the probability T_{eh} that an electron-like state is converted into a hole-like state at the opposite edge (with $G_0 = 2e^2/h$ in the p - n junction and $G_0 = 4e^2/h$ in the NS junction). In the absence of intervalley scattering, $T_{eh} = \frac{1}{2}(1 - \cos \Phi)$, with Φ the angle between the valley isospins of the electron-like state at the two edges [8].

the electrostatic potential step at the p - n interface (shown in Fig. 6.2), and \mathbf{A} the vector potential corresponding to a perpendicular magnetic field B . The Pauli matrices σ_i and τ_i act on the sublattice and valley degree of freedom, respectively (with σ_0 and τ_0 representing the 2×2 unit matrix).

The Dirac equation (6.2) is written in the valley-isotropic representation, in which the boundary condition for the wave function Ψ at the edges of the nanoribbon (taken at $y = 0, W$) has the form [8]

$$\Psi = (\boldsymbol{\nu} \cdot \boldsymbol{\tau}) \otimes (\sin \theta \sigma_x + \cos \theta \sigma_z) \Psi, \quad (6.3)$$

parameterized by an angle θ and by the three-dimensional unit vector $\boldsymbol{\nu}$ on the Bloch sphere. The vector $\boldsymbol{\nu}$ is called the valley isospin because it represents the two-component spinor of the valley degree of freedom [9].

An armchair edge has $\boldsymbol{\nu} \cdot \hat{\mathbf{z}} = 0$, $\theta = \pi/2$ (modulo π), while a zigzag edge has $|\boldsymbol{\nu} \cdot \hat{\mathbf{z}}| = 1$, $\theta = 0$ (modulo π). Confinement by an infinite mass has $|\boldsymbol{\nu} \cdot \hat{\mathbf{z}}| = 1$, $\theta = \pi/2$ (modulo π). Intermediate values of $\boldsymbol{\nu} \cdot \hat{\mathbf{z}}$ and θ are

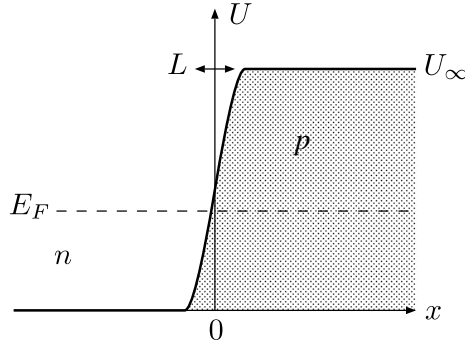


Figure 6.2. Potential step at the p - n interface (with the shaded area indicating the energy range in the valence band). The electrostatic potential $U(x)$ increases from 0 to U_∞ over a distance L around $x = 0$. The Fermi level at $E_F \in (0, U_\infty)$ lies in the conduction band for negative x (n -doped region) and in the valence band for positive x (p -doped region).

produced, for example, by a staggered edge potential (having a different value on the two sublattices) [10, 11]. If the edge is inhomogeneous, it is the value of ν and θ in the vicinity of the p - n interface (within a magnetic length $l_m = \sqrt{\hbar/eB}$ from $x = 0$) that matters for the conductance.

The boundary condition (6.3) breaks the valley degeneracy of quantum Hall edge states [12, 13, 14], with different dispersion relations $E^\pm(q)$ for the two eigenstates $|\pm\nu\rangle$ of $\nu \cdot \tau$. (We use the Landau gauge in which \mathbf{A} is parallel to the boundary and vanishes at the boundary. In this gauge the canonical momentum $\hbar q$ parallel to the boundary is a good quantum number.) In the n region (where $U = 0$) the dispersion relation is determined by the equations [8]

$$f_{E^+}(q) = \tan(\theta/2), \quad f_{E^-}(q) = -\cotan(\theta/2), \quad (6.4a)$$

$$f_E(q) \equiv \frac{H_{\varepsilon^2/2}(ql_m)}{\varepsilon H_{\varepsilon^2/2-1}(ql_m)}, \quad \varepsilon \equiv E l_m / \hbar v, \quad (6.4b)$$

with $H_\alpha(x)$ the Hermite function. The dispersion relation in the p region is obtained by $E^\pm(q) \rightarrow E^\pm(q) + U_\infty$.

The dispersion relation near the Dirac point ($E = 0$) is plotted in Fig. 6.3 for three values of θ . (It does not depend on ν .) For any $\theta \neq 0$ (modulo π) there is a nonzero interval ΔE_F of Fermi energies in which just two edge channels of *opposite* valley isospin cross the Fermi level (dotted

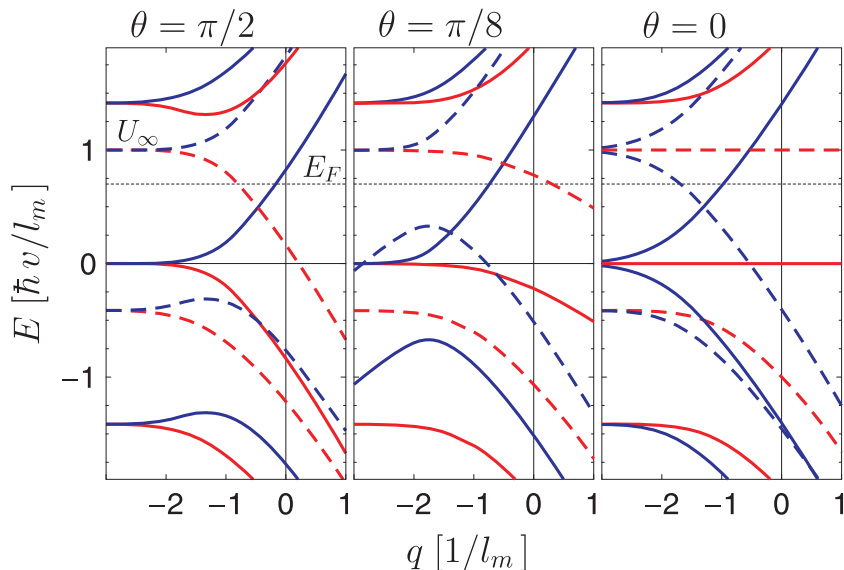


Figure 6.3. Dispersion relation $E^\pm(q)$ according to Eq. (6.4) of edge states near the Dirac point in the n region (solid curves) and in the p region (dashed curves). The color of the curves indicates the valley polarization (blue: $+\nu$, red; $-\nu$). The three panels correspond to three different boundary conditions, and illustrate the transition from an armchair edge (leftmost panel) to a zigzag edge (rightmost panel).

line), one electron-like edge channel from the n region (blue solid curve) and one hole-like edge channel from the p region (red dashed curve). The case $\theta = 0$ is special because of the dispersionless edge state which extends along a zigzag boundary [15]. As $\theta \rightarrow 0$ the interval ΔE_F shrinks to zero, and at $\theta = 0$ (modulo π) the electron-like and hole-like edge channels in the lowest Landau level have *identical* valley isospins. It is here that the analogy with the problem of the NS junction [8] stops, because in that problem the electron and hole edge channels at the Fermi level have opposite valley isospins irrespective of θ .

The two valley-polarized edge channels from the n and p regions are coupled by the potential step at the p - n interface. Edge states along a potential step which is smooth on the scale of the lattice constant a are valley degenerate [16, 17], because an electrostatic potential in the Dirac equation does not couple the valleys. The dispersion relation, for the case

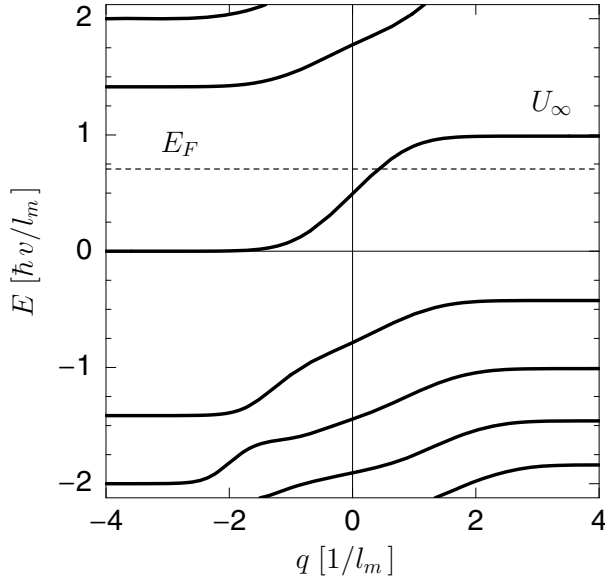


Figure 6.4. Dispersion relation at the p - n interface, calculated numerically from the Dirac equation for a step function potential profile. Each Landau level has a twofold valley degeneracy.

of an abrupt potential step ($a \ll L \ll l_m$), is plotted in Fig. 6.4. (It is qualitatively similar for $L \gg l_m$.) The Fermi level now intersects with a two-fold valley degenerate edge channel of mixed electron-hole character.

The two-terminal conductance of the p - n junction is given by [7] $G = G_0 T_{eh}$, in terms of the probability T_{eh} that an electron incident in an electron-like edge channel along the left edge is transmitted to a hole-like edge channel along the right edge. We now show that this probability takes on a universal form, dependent only on the valley isospins at the edge, in the absence of intervalley scattering. The argument is analogous to that in the NS junction [8], and requires that the electron-like and hole-like edge channels at the same edge have opposite valley isospins ($\pm\nu_L$ for the left edge and $\pm\nu_R$ for the right edge) [18].

Since the unidirectional motion of the edge states prevents reflections, the total transmission matrix $t_{\text{total}} = t_R t_{pn} t_L$ from one edge to the other edge is the product of three 2×2 unitary matrices: the transmission matrix t_L from the left edge to the p - n interface, the transmission matrix t_{pn}

along the interface, and the transmission matrix t_R from the p - n interface to the right edge. In the absence of intervalley scattering $t_{pn} = e^{i\phi_{pn}}\tau_0$ is proportional to the unit matrix, while

$$t_X = e^{i\phi_X} |+\nu_X\rangle\langle+\nu_X| + e^{i\phi'_X} |-\nu_X\rangle\langle-\nu_X| \quad (6.5)$$

(with $X = L, R$) is diagonal in the basis $|\pm\nu_X\rangle$ of eigenstates of $\nu_X \cdot \boldsymbol{\tau}$. The phase shifts $\phi_{pn}, \phi_X, \phi'_X$ need not be determined. Evaluation of the transmission probability

$$T_{eh} = |\langle+\nu_L|t_{\text{total}}|-\nu_R\rangle|^2 \quad (6.6)$$

leads to the conductance (6.1) with $\cos\Phi = \nu_L \cdot \nu_R$.

6.3 Numerical theory

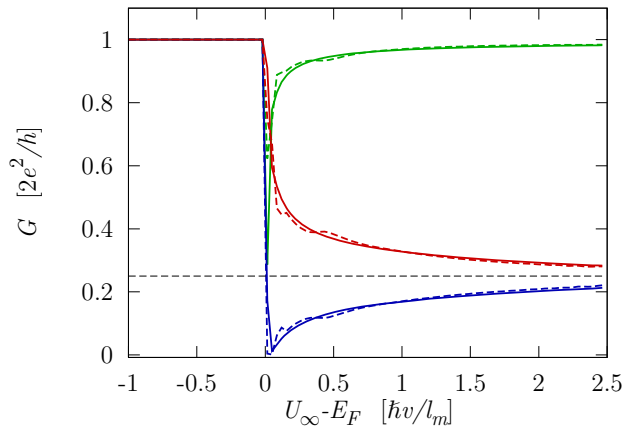


Figure 6.5. Conductance of an armchair nanoribbon containing the potential step $U(x) = \frac{1}{2}[\tanh(2x/L) + 1]U_\infty$, calculated numerically from the tight-binding model in a perpendicular magnetic field ($l_m = 5a$). The step height U_∞ is varied from below E_F (unipolar regime) to above E_F (bipolar regime), at fixed $E_F = \hbar v/l_m$ and $L = 50a$. The solid curves are without disorder, while the dashed curves are for a random electrostatic potential landscape ($K_0 = 1$, $\xi = 10a$). The number \mathcal{N} of hexagons across the ribbon is 97 (red curves), 98 (blue), and 99 (green). The dashed horizontal line marks the plateau at $G = \frac{1}{4} \times 2e^2/h$.

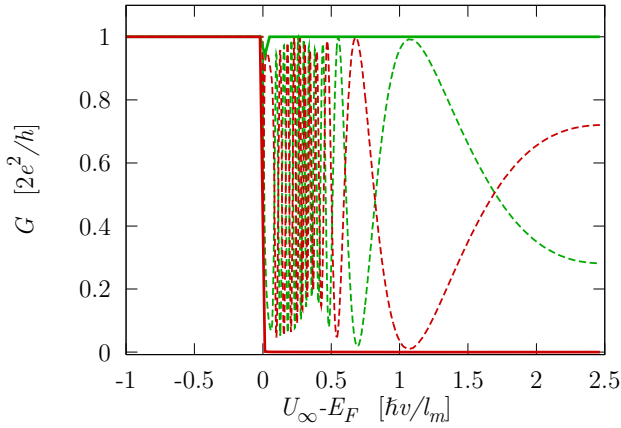


Figure 6.6. Same as Fig. 6.5, for the case of a zigzag nanoribbon ($\mathcal{N} = 114$ for the green curves and 115 for the red curves).

To test the robustness of the conductance plateau to a random electrostatic potential, we have performed numerical simulations. A random potential landscape is introduced in the same way as in Ref. [19], by randomly placing impurities at N_{imp} sites \mathbf{R}_i on a honeycomb lattice. Each impurity has a Gaussian potential profile $U_i \exp(-|\mathbf{r} - \mathbf{R}_i|^2/2\xi^2)$ of range ξ and random height $U_i \in (-\delta, \delta)$. We take ξ equal to the mean separation d of the impurities and large compared to the lattice constant a . The strength of the resulting potential fluctuations $\delta U(\mathbf{r})$ is quantified by the dimensionless correlator

$$K_0 = \frac{\mathcal{A}}{(\hbar v)^2} \frac{1}{N_{\text{tot}}^2} \sum_{i,j=1}^{N_{\text{tot}}} \langle \delta U(\mathbf{r}_i) \delta U(\mathbf{r}_j) \rangle, \quad (6.7)$$

where the sum runs over all N_{tot} lattice sites \mathbf{r}_i in a nanoribbon of area \mathcal{A} .

Results are shown in Figs. 6.5 and 6.6 for an armchair and zigzag nanoribbon, respectively. The angle Φ between the valley isospins at two opposite armchair edges depends on the number \mathcal{N} of hexagons across the ribbon: $\Phi = \pi$ if \mathcal{N} is a multiple of 3, $|\Phi| = \pi/3$ if it is not [20]. Fig. 6.5 indeed shows that the conductance as a function of $U_\infty - E_F$ switches from a plateau at the Φ -independent Hall conductance G_0 in the

unipolar regime ($U_\infty < E_F$) to a Φ -dependent value given by Eq. (6.1) in the bipolar regime ($U_\infty > E_F$). The plateau persists in the presence of a smooth random potential (compare solid and dashed curves in Fig. 6.5). By reducing the potential range we found that the plateaus did not disappear until $\xi \lesssim 3a$ (not shown).

As expected in view of the intervalley scattering produced by the dispersionless edge state in a zigzag nanoribbon, no such robust conductance plateau exists in this case (Fig. 6.6). In the presence of disorder the conductance oscillates around its ensemble average $G_0/2$, in a sample specific manner. The numerics for any given realization of the disorder potential satisfies approximately the sum rule $G(\mathcal{N}) + G(\mathcal{N} + 1) \approx G_0$, for which we have not yet found an analytical derivation.

The valley-isospin dependence of the quantum Hall effect in a p - n junction makes it possible to use *strain* as a means of variation of the height of the conductance plateaus. Strain introduces a vector potential term $ev\tau_z \otimes (\delta\mathbf{A} \cdot \boldsymbol{\sigma})\Psi$ in the Dirac equation (6.2), corresponding to a fictitious magnetic field of opposite sign in the two valleys [21, 22, 23, 24]. This term rotates the Bloch vector of the valley isospin around the z -axis, which in the case of an armchair nanoribbon corresponds to a rotation of the valley isospin in the x - y plane. Strain may appear locally at an armchair edge by passivation of the carbon bonds [10]. (The resulting change $\delta\tau$ of the hopping energy τ changes Φ by an amount [25] $\delta\Phi = 2\sqrt{3}\delta\tau/\tau$.) Random strain along the p - n interface, resulting from mesoscopic corrugation of the carbon monolayer [24], corresponds to a random value of the angle Φ in the conductance formula (6.1). A uniform distribution of Φ implies a bimodal statistical distribution of the conductance,

$$\begin{aligned} P(G) &= \frac{1}{\pi} \int_0^\pi d\Phi \delta[G - \frac{1}{2}G_0(1 - \cos\Phi)] \\ &= [\pi^2 G(G_0 - G)]^{-1/2}, \quad 0 < G < G_0, \end{aligned} \quad (6.8)$$

distinct from the uniform distribution expected for random edge channel mixing [7].

6.4 Conclusion

In summary, we have presented analytical and numerical evidence for the existence of a valley-isospin dependent conductance plateau in a p - n junction in the quantum Hall effect regime. In recent experiments [2, 3] the

conductance was simply the series conductance of the p -doped and n -doped regions, presumably because of local equilibration. We have shown that the mesoscopic fluctuations, expected to appear in the phase coherent regime [7], are suppressed in the absence of intervalley scattering. The conductance plateau is then not given by the series conductance, but by Eq. (6.1). The same formula applies to the conductance of a normal-superconducting junction in graphene [8], revealing an intriguing analogy between Klein tunneling in p - n junctions and Andreev reflection at NS interfaces [26, 27].

Bibliography

- [1] B. Huard, J. A. Sulpizio, N. Stander, K. Todd, B. Yang and D. Goldhaber-Gordon, *Phys. Rev. Lett.* **98**, 236803 (2007).
- [2] J. R. Williams, L. DiCarlo and C. M. Marcus, *Science* **317**, 638 (2007).
- [3] B. Özyilmaz, P. Jarillo-Herrero, D. Efetov, D. A. Abanin, L. S. Levitov and P. Kim, *Phys. Rev. Lett.* **99**, 166804 (2007).
- [4] V. V. Cheianov and V. I. Fal'ko, *Phys. Rev. B* **74**, 041403(R) (2006).
- [5] M. I. Katsnelson, K. S. Novoselov and A. K. Geim, *Nature Phys.* **2**, 620 (2006).
- [6] V. V. Cheianov, V. I. Fal'ko and B. L. Altshuler, *Science* **315**, 1252 (2007).
- [7] D. A. Abanin and L. S. Levitov, *Science* **317**, 641 (2007).
- [8] A. R. Akhmerov and C. W. J. Beenakker, *Phys. Rev. Lett.* **98**, 157003 (2007).
- [9] The two eigenstates $|+\nu\rangle$ and $|-\nu\rangle$ of $\nu \cdot \tau$ (defined by $\nu \cdot \tau |\pm\nu\rangle = \pm |\pm\nu\rangle$) are states of definite valley polarization (parallel or antiparallel to the unit vector ν). When the valley isospin ν points to the north pole or south pole on the Bloch sphere, the polarization is such that the eigenstate lies entirely within one single valley. This is the case for the zigzag edge or for the infinite mass confinement (for which $|\nu \cdot \hat{z}| = 1$). When the valley isospin points to the equator, the eigenstate is a coherent equal-weight superposition of the two valleys. This is the case for the armchair edge (for which $\nu \cdot \hat{z} = 0$).
- [10] Y.-W. Son, M. L. Cohen and S. G. Louie, *Phys. Rev. Lett.* **97**, 216803 (2006).

-
- [11] A. R. Akhmerov and C. W. J. Beenakker, *Phys. Rev. B* **77**, 085423 (2008).
- [12] N. M. R. Peres, F. Guinea and A. H. Castro Neto, *Phys. Rev. B* **73**, 125411 (2006).
- [13] L. Brey and H. A. Fertig, *Phys. Rev. B* **73**, 195408 (2006).
- [14] D. A. Abanin, P. A. Lee and L. S. Levitov, *Phys. Rev. Lett.* **96**, 176803 (2006).
- [15] M. Fujita, K. Wakabayashi, K. Nakada and K. Kusakabe, *J. Phys. Soc. Japan* **65**, 1920 (1996).
- [16] V. Lukose, R. Shankar and G. Baskaran, *Phys. Rev. Lett.* **98**, 116802 (2007).
- [17] J. Milton Pereira, Jr., F. M. Peeters and P. Vasilopoulos, *Phys. Rev. B* **75**, 125433 (2007).
- [18] Eq. (6.3) is invariant under the transformation $\nu \rightarrow -\nu$, $\theta \rightarrow \theta + \pi$. This freedom is used to choose the sign of ν such that the electron-like edge channel has isospin $+\nu$.
- [19] A. Rycerz, J. Tworzydło and C. W. J. Beenakker, *Europhys. Lett.* **79**, 57003 (2007).
- [20] L. Brey and H. A. Fertig, *Phys. Rev. B* **73**, 235411 (2006).
- [21] C. L. Kane and E. J. Mele, *Phys. Rev. Lett.* **78**, 1932 (1997).
- [22] H. Suzuura and T. Ando, *Phys. Rev. B* **65**, 235412 (2002).
- [23] A. F. Morpurgo and F. Guinea, *Phys. Rev. Lett.* **97**, 196804 (2006).
- [24] S. V. Morozov, K. S. Novoselov, M. I. Katsnelson, F. Schedin, L. A. Ponomarenko, D. Jiang and A. K. Geim, *Phys. Rev. Lett.* **97**, 016801 (2006).
- [25] D. S. Novikov, *Phys. Rev. Lett.* **99**, 056802 (2007).
- [26] C. W. J. Beenakker, *Phys. Rev. Lett.* **97**, 067007 (2006).
- [27] With hindsight, the same analogy can be noted between the phenomena of negative refraction of Ref. [6] and Andreev retroreflection of Ref. [26].

Chapter 7

Calculation of the conductance of a graphene sheet using the Chalker-Coddington network model

7.1 Introduction

The low-energy and long-wave-length properties of conduction electrons in a carbon monolayer (graphene) are described by the two-dimensional Dirac equation [1]. In one-dimensional geometries this partial differential equation can be solved analytically, but fully two-dimensional problems typically require a discretization to permit a numerical solution. The tight-binding model on the honeycomb lattice of carbon atoms provides the most obvious and physically motivated discretization [2]. The band structure of a honeycomb lattice has two valleys, coupled by potential variations on the scale of the lattice constant. Smooth potentials are needed if one seeks to avoid inter-valley scattering and obtain the properties of a single valley.

Discrete representations of the Dirac equation that eliminate from the outset the coupling to a second valley may provide a more efficient way to isolate the single-valley properties. Alternative tight-binding models [3, 4, 5, 6] have been introduced for that purpose. One method of dis-

cretization which has received much attention is the network model, originally introduced by Chalker and Coddington as a model for percolation in the quantum Hall effect [7]. Ho and Chalker [8] showed how a solution of this model can be mapped onto an eigenstate of the Dirac equation, and this mapping has proven to be an efficient way to study the localization of Dirac fermions [9].

The recently developed capability to do transport measurements in graphene [10] has renewed the interest in the network model [11] and also raises some questions which have not been considered before. The specific issue that we address in this chapter is how to introduce metallic contacts in the network model of graphene. Metallic contacts are introduced in the Dirac equation by means of a downward potential step of magnitude U_∞ . The limit $U_\infty \rightarrow \infty$ is taken at the end of the calculation. (It is an essential difference with the Schrödinger equation that an infinite potential step produces a *finite* contact resistance in the Dirac equation.) This phenomenological model of metallic leads, introduced in Ref. [12], is now commonly used because 1) it is analytically tractable, 2) it introduces no free parameter, and 3) it agrees well with more microscopic models [13, 14]. A direct implementation of such a metallic contact in the network model is problematic because the mapping onto the Dirac equation breaks down in the limit $U_\infty \rightarrow \infty$. Here we show how this difficulty can be circumvented.

To summarize then, there is a need to develop numerical methods for Dirac fermions in graphene when the potential landscape does not allow analytical solutions. If one implements a method based on the honeycomb lattice of graphene, intervalley scattering is present, unless the potential is smooth on the scale of the lattice. Smooth potential landscapes are experimentally relevant, but computationally expensive, because they require discretization with a large mesh. It is therefore preferable to develop a numerical method that eliminates intervalley scattering from the outset. The known correspondence between the Chalker-Coddington network model and the Dirac equation provides such a method, as we show in this chapter. The key technical result of our work is an analytical method to include heavily doped reservoirs. (Including these reservoirs numerically would have been prohibitively expensive, computationally.)

In Secs. 7.2 and 7.3 we summarize the basic equations that we will need, first regarding the Dirac equation and then regarding the network model. Our key technical result in Sec. 7.4 is a relationship between the scattering problems for the Dirac equation in the limit $U_\infty \rightarrow \infty$ and for the network

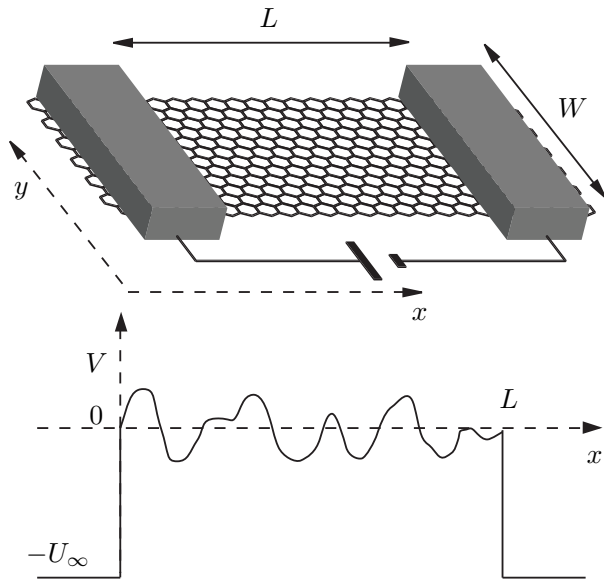


Figure 7.1. Top panel: Schematic of a graphene sheet contacted by two electrodes. A voltage source drives a current through the sheet. The bottom panel shows the potential profile $V(x, y)$ for fixed y .

model at $U_\infty \equiv 0$. We test the method in Sec. 7.5 by calculating the conductance of an electrostatically defined constriction (quantum point contact) in a graphene sheet. We also study the effect of disorder on conductance. We confirm the results of previous studies [15, 16, 17, 18] that smooth disorder (that does not cause intervalley scattering) enhances the conductivity of undoped graphene. We conclude in Sec. 7.6.

7.2 Formulation of the scattering problem

7.2.1 Scattering Matrix

A scattering formulation of electrical conduction through a graphene sheet was given in Ref. [12]. We summarize the basic equations. The geometry, shown in Fig. 7.1, consists of a weakly doped graphene sheet (length L and width W) connected to heavily doped graphene leads. A single valley

has the Dirac Hamiltonian

$$H = v\boldsymbol{\sigma} \cdot [\mathbf{p} - e\mathbf{A}(\mathbf{r})] + V(\mathbf{r}) + \sigma_z \mu(\mathbf{r}), \quad (7.1)$$

where $\mathbf{A}(\mathbf{r})$ is the magnetic vector potential, $V(\mathbf{r})$ is the electrostatic potential, and $\mu(\mathbf{r})$ is a substrate-induced mass term. The vector $\boldsymbol{\sigma} = (\sigma_x, \sigma_y)$ contains the standard Pauli matrices

$$\sigma_x = \begin{pmatrix} 0 & 1 \\ 1 & 0 \end{pmatrix}, \quad \sigma_y = \begin{pmatrix} 0 & -i \\ i & 0 \end{pmatrix}. \quad (7.2)$$

We assume that the fields \mathbf{A} , V , and μ are smooth on the scale of the lattice constant, so that the valleys are uncoupled.

In the heavily doped leads (for $x < 0$ and $x > L$) we set $V(\mathbf{r}) = -U_\infty$ and take the limit $U_\infty \rightarrow \infty$. For simplicity we set $\mu = 0$ in the leads and we also assume that the magnetic field is zero in the leads (so \mathbf{A} is constant there). The Dirac equation

$$H\Psi = E\Psi \quad (7.3)$$

has to be solved subject to boundary conditions on the wave function $\Psi(\mathbf{r})$ at $y = 0$ and $y = W$. We will consider two types of boundary conditions which mix neither valleys nor transverse modes. The first is the periodic boundary condition $\Psi|_{y=0} = \Psi|_{y=W}$. The second is the infinite-mass boundary condition¹

$$\Psi|_{y=0} = \sigma_x \Psi|_{y=0}, \quad \Psi|_{y=W} = -\sigma_x \Psi|_{y=W}. \quad (7.4)$$

We consider a scattering state Ψ_n that has unit incident current from the left in mode n and zero incident current from the right. (The quantum number n labels transverse modes.) In the leads Ψ_n has the form

$$\Psi_n(\mathbf{r}) = \chi_n^+(y) e^{ik_n x} + \sum_m r_{mn} \chi_m^-(y) e^{-ik_m x}, \quad x < 0, \quad (7.5a)$$

$$\Psi_n(\mathbf{r}) = \sum_m t_{mn} \chi_m^+(y) e^{ik_m(x-L)}, \quad x > L. \quad (7.5b)$$

¹Infinite mass boundary conditions are obtained by sending the mass to infinity for $y < 0$ and $y > W$. Particles are thus excluded from this region, much as an infinite potential excludes Schrödinger particles. As a result the boundary condition of Eq. (7.4) is imposed at the boundaries $y = 0$ and $y = W$ between the finite (or zero) mass and the infinite mass regions. For more details, see Ref. [19].

We have introduced transmission and reflection amplitudes t_{mn} and r_{mn} and the longitudinal component k_n of the wave vector of mode n . The right-propagating component in mode n has a spinor χ_n^+ and the left-propagating component has a spinor χ_n^- .

In the limit $U_\infty \rightarrow \infty$, the form of the scattering state in the leads can be simplified considerably. The n -dependence of k_n can be neglected, since $k_n \simeq U_\infty/\hbar v \rightarrow \infty$ as $U_\infty \rightarrow \infty$. The number $N_\infty \simeq U_\infty W/\hbar v$ of propagating modes in the leads can be taken infinitely large. When $N_\infty \rightarrow \infty$, the choice of boundary condition in the leads (not in the sample) becomes irrelevant and we choose periodic boundary conditions in the leads for simplicity. Modes that are responsible for transport through the weakly doped sample have transverse momenta $|q_n| \ll U_\infty$. The corresponding spinors χ_n^\pm are

$$\chi_n^\pm(y) = \frac{1}{\sqrt{2W}} e^{iq_n y} \begin{pmatrix} 1 \\ \pm 1 \end{pmatrix}, \quad q_n = \frac{2\pi n}{W}, \quad (7.6)$$

with $n = 0, \pm 1, \pm 2, \dots$. While it is important not to neglect the finiteness of q_n in the phase factor $\exp(iq_n y)$ of these modes, the spinor structure is proportional to $(1, \pm 1)$ independent of n , because $q_n/U_\infty \rightarrow 0$. We note the orthogonality relation

$$\int_0^W dy \chi_m^\sigma(y)^\dagger \chi_n^{\sigma'}(y) = \delta_{m,n} \delta_{\sigma,\sigma'}. \quad (7.7)$$

We also note that the definition of $\chi_n^\pm(y)$ ensures that each scattering state Ψ_n carries unit incident current.

In a similar way, we can define a scattering state incident from the right in mode n with transmission and reflection amplitudes t'_{mn} and r'_{mn} . The transmission and reflection amplitudes constitute the scattering matrix

$$S = \begin{pmatrix} r & t' \\ t & r' \end{pmatrix}, \quad (7.8)$$

which is a unitary matrix that determines transport properties. For example, the conductance G follows from the Landauer formula

$$G = \frac{4e^2}{h} \text{Tr } tt^\dagger = \frac{4e^2}{h} \text{Tr } t't'^\dagger, \quad (7.9)$$

where the factor of 4 accounts for spin and valley degeneracies.

7.2.2 Transfer matrix

The information contained in the scattering matrix S can equivalently be represented by the transfer matrix T . While the scattering matrix relates outgoing waves to incoming waves, the transfer matrix relates waves at the right,

$$\Psi_R(\mathbf{r}) = \sum_{n,\sigma} b_n^\sigma \chi_n^\sigma(y) e^{i\sigma k_n(x-L)}, \quad x > L, \quad (7.10)$$

to waves at the left,

$$\Psi_L(\mathbf{r}) = \sum_{n,\sigma} a_n^\sigma \chi_n^\sigma(y) e^{i\sigma k_n x}, \quad x < 0. \quad (7.11)$$

The relation takes the form

$$b_m^\sigma = \sum_{n,\sigma'} T_{m,n}^{\sigma,\sigma'} a_n^{\sigma'}. \quad (7.12)$$

The four blocks $T^{\sigma,\sigma'}$ of the transfer matrix are related to the transmission and reflection matrices by

$$r = -(T^{--})^{-1} T^{-+}, \quad (7.13a)$$

$$t = T^{++} - T^{+-} (T^{--})^{-1} T^{-+}, \quad (7.13b)$$

$$t' = (T^{--})^{-1}, \quad (7.13c)$$

$$r' = T^{+-} (T^{--})^{-1}. \quad (7.13d)$$

Unitarity of S implies for T the current conservation relation

$$T^{-1} = \Sigma_z T^\dagger \Sigma_z, \quad (7.14)$$

where Σ_z is a matrix in the space of modes with entries $(\Sigma_z)_{m,n} = \delta_{m,n} \sigma_z$ that are themselves 2×2 matrices. In terms of the transfer matrix the Landauer formula (7.9) can be written as

$$G = \frac{4e^2}{h} \text{Tr} \left[\left(T^{--\dagger} T^{--} \right)^{-1} \right]. \quad (7.15)$$

7.2.3 Real-space formulation

In order to make contact with the network model, it is convenient to change from the basis of transverse modes (labeled by the quantum number n) to a real space basis (labeled by the transverse coordinate y). The real space transfer matrix $X_{y,y'}$ is defined by

$$\Psi(L, y) = \int_0^W dy' X_{y,y'} \Psi(0, y'), \quad (7.16)$$

where $\Psi(x, y)$ is any solution of the Dirac equation (7.3) at a given energy E . The kernel $X_{y,y'}$ is a 2×2 matrix, acting on the spinor Ψ . Because the integral (7.16) extends only over the weakly doped region, X does not depend on the potential U_∞ in the leads.

In view of the orthogonality relation (7.7) the real-space transfer matrix X is related to the transfer matrix T defined in the basis of modes in the leads by a projection onto χ_m^\pm ,

$$T_{m,n}^{\sigma,\sigma'} = \int_0^W dy \int_0^W dy' \chi_m^\sigma(y)^\dagger X_{y,y'} \chi_n^{\sigma'}(y'). \quad (7.17)$$

We now substitute the explicit form of χ_n^σ from Eq. (7.6). The integrals over y and y' in Eq. (7.17) amount to a Fourier transform,

$$X_{m,n} = \frac{1}{W} \int_0^W dy \int_0^W dy' e^{-iq_m y} X_{y,y'} e^{iq_n y'}. \quad (7.18)$$

From Eq. (7.17) we conclude that the 2×2 matrix structure of the transfer matrix,

$$T_{m,n} = \begin{pmatrix} T_{m,n}^{++} & T_{m,n}^{+-} \\ T_{m,n}^{-+} & T_{m,n}^{--} \end{pmatrix}, \quad (7.19)$$

is related to the 2×2 matrix structure of the real-space transfer matrix by a Hadamard transformation:

$$T_{m,n} = \mathcal{H} X_{m,n} \mathcal{H}, \quad \mathcal{H} = \frac{1}{\sqrt{2}} \begin{pmatrix} 1 & 1 \\ 1 & -1 \end{pmatrix}. \quad (7.20)$$

(The unitary and Hermitian matrix \mathcal{H} is called the Hadamard matrix.) In view of Eq. (7.14), the current conservation relation for X reads

$$X^{-1} = \Sigma_x X^\dagger \Sigma_x, \quad (\Sigma_x)_{m,n} = \delta_{m,n} \sigma_x, \quad (7.21)$$

where we used $\mathcal{H} \sigma_z \mathcal{H} = \sigma_x$.

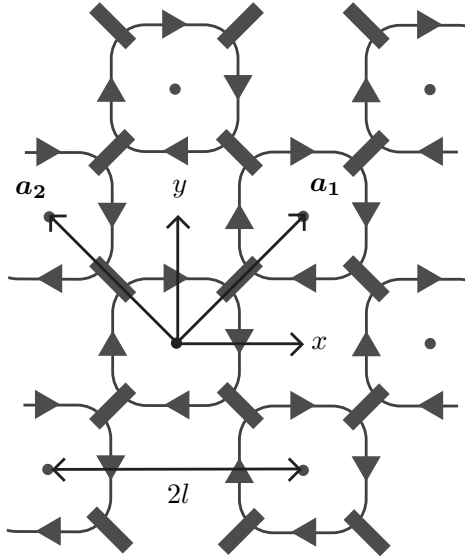


Figure 7.2. Square lattice (dots), with circulating current loops that form the network model. The loops are coupled to nearest neighbors at the black rectangles. The lattice vectors \mathbf{a}_1 and \mathbf{a}_2 (each of length $\sqrt{2}l$) are indicated.

7.3 Formulation of the network model

The Chalker-Coddington network model [7, 9] was originally introduced in order to analyze the localization transition in the quantum Hall effect. Our interest in this model stems from the fact that it is known to map onto the two-dimensional Dirac equation [8]. We briefly recall how the network model is defined and how the mapping to the Dirac equation works. We consider the square lattice shown in Fig. 7.2, with lattice constant $\sqrt{2}l$ and lattice vectors

$$\mathbf{a}_1 = l(\hat{x} + \hat{y}), \quad \mathbf{a}_2 = l(\hat{y} - \hat{x}). \quad (7.22)$$

The integers (m, n) label the lattice site $\mathbf{r}_{m,n} = m\mathbf{a}_1 + n\mathbf{a}_2$. With each site is associated a single current loop circling the site without enclosing any neighboring sites, say clockwise if viewed from the positive z axis. The radii of these loops are expanded until states associated with nearest neighboring sites overlap. At these points of overlap, states on adjacent loops can scatter into each other.

As illustrated in Fig. 7.3, four current amplitudes $Z_{m,n}^{(k)}$, $k = 1, \dots, 4$ are associated with each site (m, n) . These are amplitudes incident upon points of overlap, ordered clockwise, starting from the point of overlap with site $(m + 1, n)$. Each incident wave amplitude $Z_{m,n}^{(k)}$ has picked up a phase $\phi_{m,n}^{(n)}$ since the previous point of overlap. With the point of overlap between loop (m, n) and $(m + 1, n)$ is associated a 2×2 scattering matrix $s_{m,n}^+$, while $s_{m,n}^-$ is associated with the point of overlap between (m, n) and $(m, n - 1)$.

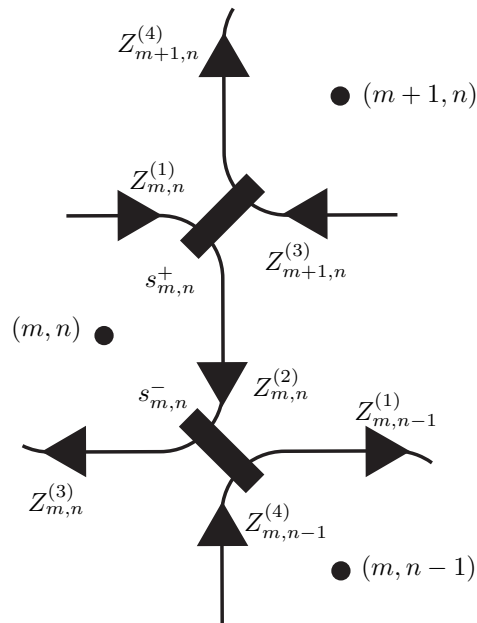


Figure 7.3. Segment of the network of Fig. 7.2 with the wave amplitudes $Z_{m,n}^{(n)}$ and scattering matrices $s_{m,n}^\pm$ indicated.

The matrix elements of $s_{m,n}^+$ and $s_{m,n}^-$ are arranged such that

$$\begin{pmatrix} Z_{m,n}^{(2)} \\ Z_{m+1,n}^{(4)} \end{pmatrix} = \begin{pmatrix} e^{i\phi_{m,n}^{(2)}} & 0 \\ 0 & e^{i\phi_{m+1,n}^{(4)}} \end{pmatrix} s_{m,n}^+ \begin{pmatrix} Z_{m,n}^{(1)} \\ Z_{m+1,n}^{(3)} \end{pmatrix}, \quad (7.23a)$$

$$\begin{pmatrix} Z_{m,n-1}^{(1)} \\ Z_{m,n}^{(3)} \end{pmatrix} = \begin{pmatrix} e^{i\phi_{m,n-1}^{(1)}} & 0 \\ 0 & e^{i\phi_{m,n}^{(3)}} \end{pmatrix} s_{m,n}^- \begin{pmatrix} Z_{m,n}^{(2)} \\ Z_{m,n-1}^{(4)} \end{pmatrix}. \quad (7.23b)$$

Ho and Chalker [8] showed how this model can be mapped onto the Dirac equation for two-dimensional fermions. Firstly, one parametrizes the scattering matrices $s_{m,n}^\pm$ in terms of Pauli matrices σ_i ,

$$s_{m,n}^- = \sin\left(\frac{\pi}{4} + \beta_{m,n}\right) \sigma_z + \cos\left(\frac{\pi}{4} + \beta_{m,n}\right) \sigma_x, \quad (7.24a)$$

$$s_{m,n}^+ = \cos\left(\frac{\pi}{4} + \beta_{m,n}\right) \sigma_z + \sin\left(\frac{\pi}{4} + \beta_{m,n}\right) \sigma_x. \quad (7.24b)$$

(The same matrix of coefficients $\beta_{m,n}$ is used for $s_{m,n}^+$ and $s_{m,n}^-$.) For given fields $V(\mathbf{r})$, $\mathbf{A}(\mathbf{r})$, and $\mu(\mathbf{r})$ in the Dirac equation, the mapping then dictates a corresponding choice of parameters in the network model, namely $\phi_{m,n}^{(k)}$ and $\beta_{m,n}$ have to satisfy [8]

$$\frac{1}{2} \sum_{k=1}^4 \phi_{m,n}^{(k)} = [E - V(\mathbf{r}_{m,n})] \frac{l}{\hbar v}, \quad (7.25a)$$

$$\frac{\phi_{m,n}^{(1)} - \phi_{m,n}^{(3)}}{2} = A_x(\mathbf{r}_{m,n}) \frac{el}{\hbar v}, \quad (7.25b)$$

$$\frac{\phi_{m,n}^{(4)} - \phi_{m,n}^{(2)}}{2} = A_y(\mathbf{r}_{m,n}) \frac{el}{\hbar v}, \quad (7.25c)$$

$$2\beta_{m,n} = \mu(\mathbf{r}_{m,n}) \frac{l}{\hbar v}. \quad (7.25d)$$

With this choice of parameters there is an approximate equality between a solution $\Psi(\mathbf{r})$ of the Dirac equation and the current amplitudes of the network model,

$$\Psi(\mathbf{r}_{m,n}) \approx \mathcal{G} \begin{pmatrix} Z_{m,n}^{(1)} \\ Z_{m,n}^{(3)} \end{pmatrix}, \quad \mathcal{G} = \frac{1}{\sqrt{2}} \begin{pmatrix} 1 & i \\ 1 & -i \end{pmatrix}. \quad (7.26)$$

The accuracy of the approximation is improved by making the lattice constant $\sqrt{2}l$ smaller and smaller.

As mentioned in Sec. 7.2, we will be considering two types of boundary conditions at $y = 0$ and $y = W$ in the sample region $0 < x < L$. The periodic boundary condition is realized in the network model by putting the square lattice on a cylinder of circumference $W = 2Nl$ oriented along the x -axis. The infinite-mass boundary condition is realized [8] by terminating the square lattice at $y = 0$ and $y = W$ and adjusting the scattering phases along the edge. The edge $y = 0$ lies at sites $(n, -n)$ and the edge $y = W$ lies at sites $(N - 1 + n, N - 1 - n)$. As shown in App. 7.A, for sites $(n, -n)$ Eq. (7.23) must be replaced with

$$Z_{n,-n}^{(4)} = -Z_{n,-n}^{(3)}, \quad Z_{n,-n}^{(3)} = Z_{n,-n}^{(2)}, \quad (7.27)$$

while for sites $(N + n, N - n)$ it must be replaced with

$$Z_{N+n,N-n}^{(2)} = Z_{N+n,N-n}^{(1)}, \quad Z_{N+n,N-n}^{(4)} = Z_{N+n,N-n}^{(1)}. \quad (7.28)$$

7.4 Correspondence between scattering matrices of Dirac equation and network model

In this section we combine the known results summarized in the previous two sections to construct the scattering matrix S of a graphene strip with heavily doped leads from a solution of the network model. This construction does not immediately follow from the correspondence (7.26) because the limit $U_\infty \rightarrow \infty$ of heavily doped leads still needs to be taken. At first glance it would seem that, in order to preserve the correspondence between the network model and the Dirac equation, we must simultaneously take the limit $l \rightarrow 0$ so that $U_\infty l / \hbar v$ remains small. (The correspondence between the network model and the Dirac equation is correct only to first order in this quantity.) This would imply that very large networks are required for an accurate representation of the graphene strip.

It turns out, however, that it is not necessary to model the heavily doped leads explicitly in the network model, as we now demonstrate. We define the real-space transfer matrix Y as the matrix that relates $Z^{(1)}$ and $Z^{(3)}$ at the right edge of the network to $Z^{(1)}$ and $Z^{(3)}$ at the left edge of the network. The left edge ($x = 0$) lies at sites (n, n) with $n = 0, 1, 2, \dots, N -$

1. The right edge at $x = L = 2Ml$ lies at sites $(n + M, n - M)$. The real-space transfer matrix Y relates

$$\begin{pmatrix} Z_{n+M, n-M}^{(1)} \\ Z_{n+M, n-M}^{(3)} \end{pmatrix} = \sum_{n'=0}^{N-1} Y_{n, n'} \begin{pmatrix} Z_{n', n'}^{(1)} \\ Z_{n', n'}^{(3)} \end{pmatrix}. \quad (7.29)$$

We define the Fourier transform

$$Y_{q_m, q_n} = \frac{1}{N} \sum_{m'=0}^{N-1} \sum_{n'=0}^{N-1} e^{-2ilq_m m'} Y_{m', n'} e^{2ilq_n n'}, \quad (7.30)$$

with $q_n = 2\pi n/W$.

In view of the relation (7.26) between the Dirac wave function Ψ and the network amplitudes $Z^{(1)}$, $Z^{(3)}$, the real space transfer matrix X of the Dirac equation is related to Y by a unitary transformation,

$$X_{y=2ln, y'=2ln'} = \frac{1}{2l} \mathcal{G} Y_{n, n'} \mathcal{G}^\dagger. \quad (7.31)$$

We can now use the relation (7.20) between X and the transfer matrix T to obtain

$$T_{m, n} = \begin{pmatrix} 1 & 0 \\ 0 & i \end{pmatrix} Y_{q_m, q_n} \begin{pmatrix} 1 & 0 \\ 0 & -i \end{pmatrix}, \quad (7.32)$$

where we have used

$$\mathcal{H}\mathcal{G} = \begin{pmatrix} 1 & 0 \\ 0 & i \end{pmatrix}. \quad (7.33)$$

From Eq. (7.32) it follows that the lower right blocks of T and Y are equal: $T_{m, n}^{--} = Y_{q_m, q_n}^{--}$. Substitution into the Landauer formula (7.15) gives

$$G = \frac{4e^2}{h} \text{Tr} \left[\left(Y^{--\dagger} Y^{--} \right)^{-1} \right]. \quad (7.34)$$

The Landauer formula applied to the network model thus gives the conductance of the corresponding graphene sheet connected to heavily doped leads. For later use, we note the current conservation relation for Y , which follows from Eqs. (7.14) and (7.32)

$$Y^{-1} = \Sigma_z Y^\dagger \Sigma_z. \quad (7.35)$$

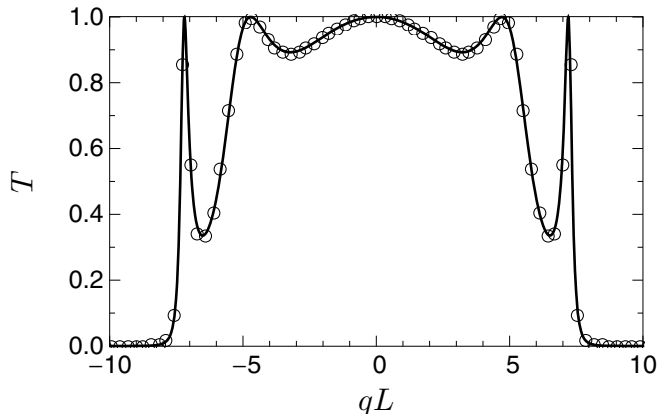


Figure 7.4. Transmission probability of a clean graphene sheet, at energy $E = 7.85 \hbar v/L$ as a function of transverse wave number q . The solid line is the result (7.38) from the Dirac equation, while the open circles were numerically calculated using the network model with periodic boundary conditions (when $q = 2\pi n/W$). The discretization parameter of the network was $\epsilon = El/\hbar v = 0.28$.

7.5 Numerical Solution

In this section we test the accuracy and efficiency of the solution of a scattering problem in graphene by means of the network model. As explained in Sec. 7.4 we need to calculate the real space transfer matrix Y through the weakly doped region. The conductance of the corresponding graphene sample then follows from Eq. (7.34).

We calculate the real-space transfer matrix recursively by adding slices to the network and multiplying the transfer matrices of individual slices. Since a multiplication of transfer matrices is numerically unstable we stabilize the algorithm as explained in App. 7.B. We limit the numerical investigation in this section to the case $A(\mathbf{r}) = 0$, $\mu(\mathbf{r}) = 0$ where only the electrostatic potential $V(\mathbf{r})$ is non-zero.

We have found that the efficiency of the algorithm can be improved by using the fact that, according to Eq. (7.25), there is some arbitrariness in the choice of the phases $\phi^{(1)}, \dots, \phi^{(4)}$. For $A(\mathbf{r}) = 0$ and $\mu(\mathbf{r}) = 0$, one choice of the phases could be

$$\phi_{m,n}^{(k)} = [E - V(m\mathbf{a}_1 + n\mathbf{a}_2)]l/2, \quad k = 1, \dots, 4. \quad (7.36)$$

Another choice is

$$\phi_{m,n}^{(1)} = \phi_{m,n}^{(3)} = [E - V(\mathbf{r}_{m,n})]l, \quad \phi^{(2)} = \phi^{(4)} = 0. \quad (7.37)$$

The correspondence (7.26) between the network model and the Dirac equation holds for both choices of the phases, however the corrections for finite l are smaller for choice (7.37). More precisely, as shown in App. 7.C, if $\phi^{(2)}$ and $\phi^{(4)}$ are zero, the network model does not contain corrections to the Dirac equation of order $\partial_{\mathbf{r}} V l$.

Let us first consider the analytically solvable case of a clean graphene sheet that is obtained by setting $V = 0$ in the weakly doped region. The Dirac equation gives transmission probabilities [12]

$$T(E, q) = \left| \cos \xi L + i \frac{E \sin \xi L}{\hbar v \xi} \right|^{-2}, \quad (7.38a)$$

$$\xi = \sqrt{\left(\frac{E}{\hbar v}\right)^2 - q^2}. \quad (7.38b)$$

For periodic boundary conditions the transverse wave vector is discretized as $q_n = 2\pi n/W$, with $n = 0, \pm 1, \pm 2, \dots$

In Fig. 7.4 we compare Eq. (7.38) to the results from the network model for periodic boundary conditions in the weakly doped region. The small parameter that controls the accuracy of the correspondence is $\epsilon = El/\hbar v$. We find excellent agreement for a relatively large $\epsilon \simeq 0.3$.

Fig. 7.5 shows the conductivity

$$\sigma = \frac{L}{W} \frac{4e^2}{h} \sum_n T(E, q_n) \quad (7.39)$$

at the Dirac point ($E = 0$) as a function of the aspect ratio W/L . We do the calculation both for periodic and infinite mass boundary conditions in the weakly doped region. (In the latter case $q_n = (n + \frac{1}{2})\pi/W$ with $n = 0, 1, 2, \dots$) Again we see excellent agreement with the analytical results from the Dirac equation [12].

We now apply the network model to a case that cannot be solved analytically, because it involves inter-mode scattering. We take the electrostatic potential landscape shown in Fig. 7.6, which produces a narrow constriction or quantum point contact of width D and length L_c . In the weakly doped region, of length L , electrons have an energy E_F measured

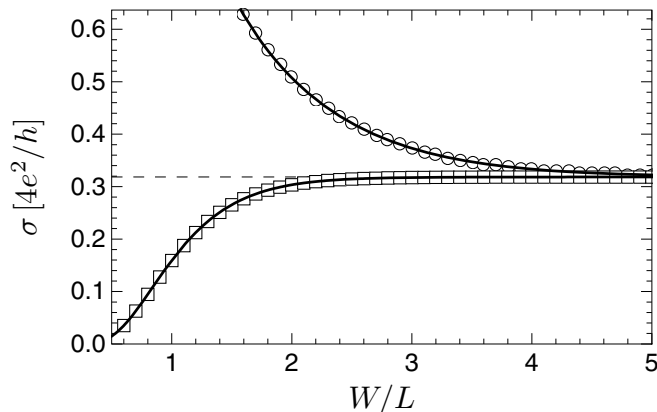


Figure 7.5. Conductivity $\sigma = G \times L/W$ at $E = 0$ for a clean graphene sheet as a function of the aspect ratio. The data points were calculated from the network model for fixed $L = 40l$ with periodic boundary conditions (circles) and infinite mass boundary conditions (squares) in the weakly doped region. The solid lines are the result [12] from the Dirac equation. The dashed line indicates the limiting value $\sigma h/4e^2 = 1/\pi$ for short wide samples.

from the Dirac point. The barrier potential is tuned so that electron transport through the barrier takes place at the Dirac point, where all waves are evanescent. As the constriction is widened, the number of modes at a given energy that propagates through the opening increases. For fixed E_F , this should lead to steps in the conductance as a function of opening width, at intervals of roughly π/E_F . The steps are smooth because the current can also tunnel through the barrier.

We have calculated the conductance with the network model (solid curve in Fig. 7.7) and using the tight-binding model of graphene (dashed curve). In the tight-binding calculation we did not connect heavily doped leads to the weakly doped region. This does not affect the results, as long as $L \gg L_c$.

Both calculations show a smooth sequence of steps in the conductance. The agreement is reasonably good, but not as good as in the previous cases. This can be understood since the tight-binding model of graphene is only equivalent to the Dirac equation on long length-scales.

The final numerical study that we report on in this chapter involves transport at the Dirac point through a disordered potential landscape. Re-

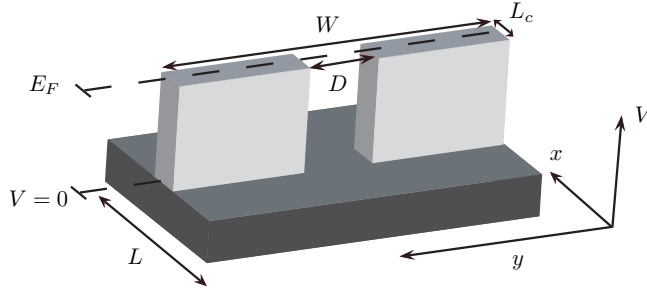


Figure 7.6. Potential landscape $V(x, y)$ that produces a quantum point contact. The Fermi energy E_F is indicated.

cent experimental studies [23] have observed electron and hole puddles in undoped graphene. The correlation length of the potential is larger than the lattice constant, hence intervalley scattering is weak. We are therefore in the regime of applicability of the network model (which eliminates intervalley scattering from the outset).

To model the electron and hole puddles, we divide the sample into an array of square tiles (Fig 7.8), where each tile has size $10l \times 10l$, $\sqrt{2}l$ being the lattice constant of the network model. The electrostatic potential is constant on a single tile, but uncorrelated with the potential on the other tiles. We take the values of the potential on any given tile to be a random variable uniformly distributed between $-V_{\max}$ and V_{\max} . To make contact with previous studies [15, 16], we quantify the disorder strength by the dimensionless number

$$K_0 = \frac{1}{(\hbar v)^2} \int d\mathbf{r}' \langle V(\mathbf{r})V(\mathbf{r}') \rangle. \quad (7.40)$$

(The average $\langle V(\mathbf{r}) \rangle$ is zero.) With tiles of dimension $10l \times 10l$, the relation between K_0 and V_{\max} is $K_0 = 100(V_{\max}l/\hbar v)^2/3$ and the network model faithfully represents the Dirac equation for values up to $K_0 \simeq 10$. We use a sample with aspect ratio $W/L = 5$ and average over 100 disorder realizations. We repeat the calculation for two different sample sizes namely $W = 5L = 300l$ and $W = 5L = 450l$. The calculation is performed for transport at energy $E = 0$, i.e. the Dirac point of a clean, undoped sample. In Fig. 7.9 we show the average conductance. Remarkably enough the conductance increases with increasing disorder strength.

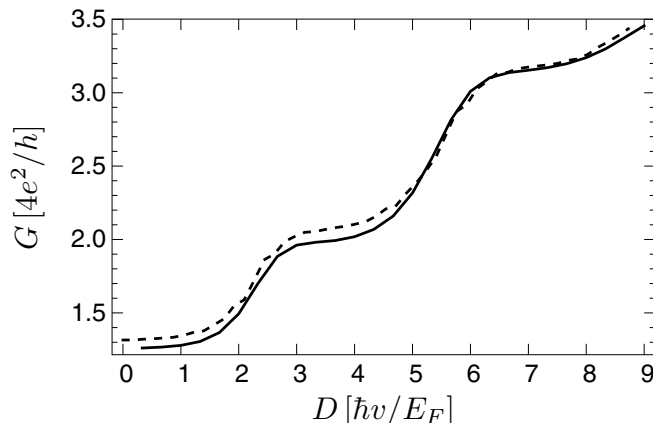


Figure 7.7. Conductance through the constriction of Fig. 7.6 as a function of the width of the opening in the constriction. The solid line was obtained using the network model, while the dashed line was obtained using the tight-binding model of graphene. We used parameters $W = 35 \hbar v/E_F$, $L_c = 8.7 \hbar v/E_F$. For the network model we set the length of the weakly doped region to $L = 49 \hbar v/E_F$ and used a lattice constant $\sqrt{2}l = 0.24 \hbar v/E_F$, while in the tight-binding calculation we used a lattice constant $0.17 \hbar v/E_F$.

This is consistent with the results obtained in Refs. [15, 16, 17, 18]. The effect should not depend on the shape of the tiles in our model for the disorder. We have therefore repeated the calculation with rhombic instead of square tiles. We find deviations of less than 5%.

The increase in conductance is explained by the non-zero density of states at the Dirac point that is induced by the disorder, together with the absence of back-scattering for Dirac electrons. While we do not make a detailed study of the dependence of conductance on sample size (at fixed aspect ratio), we note that the conductance of larger samples (squares in Fig. 7.9) is larger than the conductance of the smaller samples (circles in Fig. 7.9). This is consistent with the scaling behavior found in Refs. [16, 17, 18].

7.6 Conclusion

In conclusion, we have shown how the Chalker-Coddington network model can be used to solve a scattering problem in a weakly doped graphene

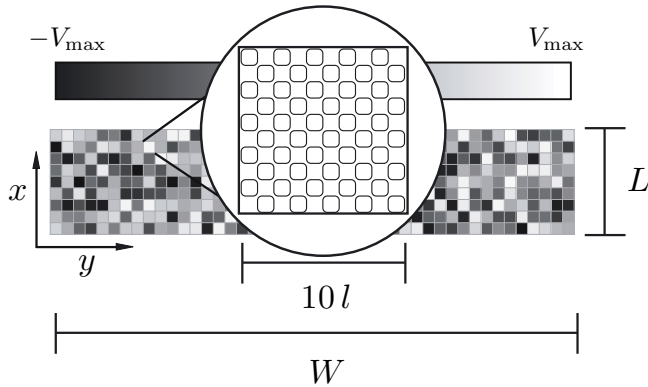


Figure 7.8. Illustration of the model of electron and hole puddles in a graphene strip that we have studied. The sample is divided into tiles. The value of the potential on a tile is a constant, here indicated in gray-scale, uniformly distributed between $-V_{\max}$ and V_{\max} . The potential on different tiles is uncorrelated. We choose a mesh for the network such that each tile has size $10l \times 10l$, where the network lattice constant is $\sqrt{2}l$.

sheet between heavily doped electron reservoirs (which model the metallic contacts). The method is particularly useful when the scattering problem does not allow an analytical solution, so that a numerical solution is required. The network model eliminates intervalley scattering from the outset. Thus, with a given mesh size, a larger graphene sample can be modeled with the network model than with methods based on the honeycomb lattice. The key technical result of our work is that an infinitely high potential step at the contacts can be implemented analytically by a unitary transformation of the real-space transfer matrix, without having to adjust the lattice constant of the network model to the small values needed to accommodate the small wave length in the contacts. We have demonstrated that the algorithm provides an accuracy and efficiency comparable to the tight-binding model on a honeycomb lattice. In agreement with the existing literature [15, 16, 17, 18] we have found that disorder that is smooth on the scale of the graphene lattice constant enhances conductivity at the Dirac point. The absence of intervalley scattering in the network model may prove useful for the study of these and other single-valley properties.

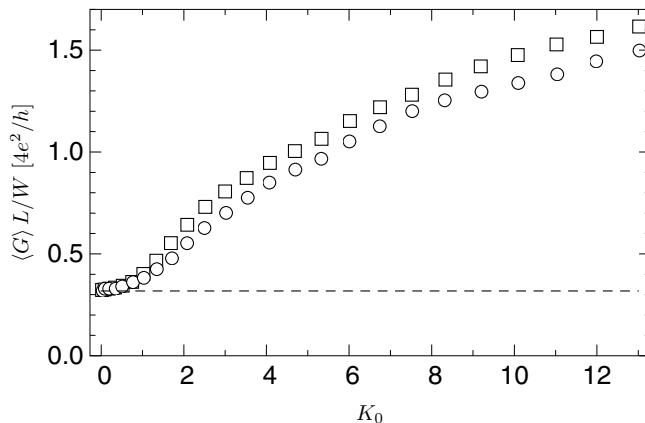


Figure 7.9. Conductivity $\sigma = G L/W$ averaged over 100 disorder realizations versus disorder strength K_0 at the Dirac point $E = 0$. The circles are for samples of size $60l \times 300l$ while squares are for samples of size $90l \times 450l$. The statistical error is of the order of the size of the data points. The dotted line indicates the ballistic limit $G L/W = 4e^2/\pi h$.

Appendix 7.A Infinite-mass boundary condition for the network model

In this appendix we consider the boundary condition imposed on the Dirac equation by termination of the network along a straight edge. We consider the eight orientations shown in Fig. 7.10 which have the shortest periodicity along the edge. Since we want to discuss the long wave-length limit, each edge needs to be much longer than the lattice constant $\sqrt{2}l$. (In this respect the figure with its relatively short edges is only schematic.) The orientations are defined by the vector $\hat{\mathbf{n}}(\alpha) = -\hat{\mathbf{x}} \sin \alpha + \hat{\mathbf{y}} \cos \alpha$, $\alpha = j\pi/4$, $j = 1, \dots, 8$ which is perpendicular to the edge and points outwards.

We wish to impose the infinite mass boundary condition [19]

$$\begin{aligned} \Psi_{\text{edge}} &= [\hat{\mathbf{n}}(\alpha) \times \hat{\mathbf{z}}] \cdot \boldsymbol{\sigma} \Psi_{\text{edge}} \\ &= (\sigma_x \cos \alpha + \sigma_y \sin \alpha) \Psi_{\text{edge}} \end{aligned} \quad (7.41)$$

on the Dirac wavefunction at the edge. In view of the correspondence (7.26) between the Dirac equation and the network model, Eq. (7.41) im-

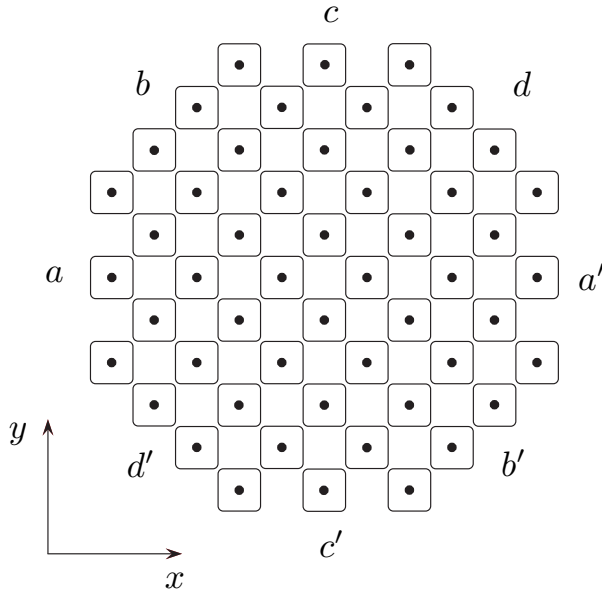


Figure 7.10. Network of circulating current loops, as in Fig. 7.2, but now terminated with straight edges. The letters a, b, \dots label the orientation of the edge.

plies the boundary condition

$$\begin{pmatrix} Z^{(1)} \\ Z^{(3)} \end{pmatrix}_{\text{edge}} = (-\sigma_x \sin \alpha + \sigma_z \cos \alpha) \begin{pmatrix} Z^{(1)} \\ Z^{(3)} \end{pmatrix}_{\text{edge}} \quad (7.42)$$

on the network amplitudes.

Away from the edge, the network amplitudes obey the equations (7.23). For $\mu, \mathbf{A}, V,$ and E all equal to zero (Dirac point) these reduce to

$$\begin{pmatrix} Z_{m,n}^{(2)} \\ Z_{m+1,n}^{(4)} \end{pmatrix} = \mathcal{H} \begin{pmatrix} Z_{m,n}^{(1)} \\ Z_{m+1,n}^{(3)} \end{pmatrix}, \quad (7.43a)$$

$$\begin{pmatrix} Z_{m,n-1}^{(1)} \\ Z_{m,n}^{(3)} \end{pmatrix} = \mathcal{H} \begin{pmatrix} Z_{m,n}^{(2)} \\ Z_{m,n-1}^{(4)} \end{pmatrix}. \quad (7.43b)$$

from scattering into the non-existent amplitudes $Z_{m-1,m}^{(2)}$ belonging to the removed sites $(m-1, m)$. Similarly, the amplitudes $Z_{m,m}^{(4)}$ are prevented from scattering into the non-existent amplitudes $Z_{m,m+1}^{(3)}$. To do this one must modify the scattering matrices $s_{m-1,m}^+$ so that $Z_{m,m}^{(3)}$ can only scatter into $Z_{m,m}^{(4)}$ and $s_{m,m+1}^-$ so that $Z_{m,m}^{(4)}$ can only scatter into $Z_{m,m}^{(1)}$. As a consequence, for $n = m + 1$ Eq. (7.43) is replaced by

$$Z_{m,m}^{(4)} = -Z_{m,m}^{(3)}, \quad Z_{m,m}^{(1)} = Z_{m,m}^{(4)}. \quad (7.45)$$

We eliminate $Z^{(2)}$ and $Z^{(4)}$ to arrive at Eq. (7.44) for $n < m$ and Eq. (7.44b) for $n = m$. Eq. (7.44a) for $n = m$ is replaced by

$$Z_{m,m}^{(1)} = -Z_{m,m}^{(3)}. \quad (7.46)$$

The solution $(Z_{m,n}^{(1)}, Z_{m,n}^{(3)}) \propto (1, -1)$ indeed satisfies the infinite mass boundary condition (7.42) with $\alpha = \pi/2$.

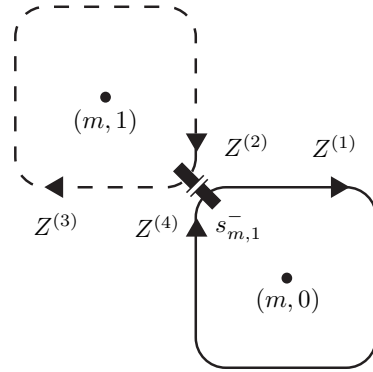


Figure 7.12. Edge with orientation b .

Edge b is constructed by removing all sites (m, n) with $n > 0$. (See Fig. 7.12.) This means that the network amplitudes $Z_{m,0}^{(4)}$ are prevented from scattering into the non-existent amplitudes $Z_{m,1}^{(3)}$ belonging to the removed sites $(m, 1)$. For $n = 1$, we replace Eq. (7.43b) by

$$Z_{m,0}^{(1)} = Z_{m,0}^{(4)}. \quad (7.47)$$

If we now eliminate the amplitudes $Z^{(2)}$ and $Z^{(4)}$ we find that Eq. (7.44) is still valid for all $n < 0$. For $n = 0$, Eq. (7.44b) still holds, while Eq. (7.44a) is changed to

$$Z_{m,0}^{(1)} = \frac{1}{\sqrt{2}} \left(Z_{m-1,0}^{(1)} - Z_{m,0}^{(3)} \right). \quad (7.48)$$

The solution $(Z_{m,n}^{(1)}, Z_{m,n}^{(3)})^T \propto (1, 1 - \sqrt{2})$ satisfies the infinite mass boundary condition (7.42) with $\alpha = \pi/4$.

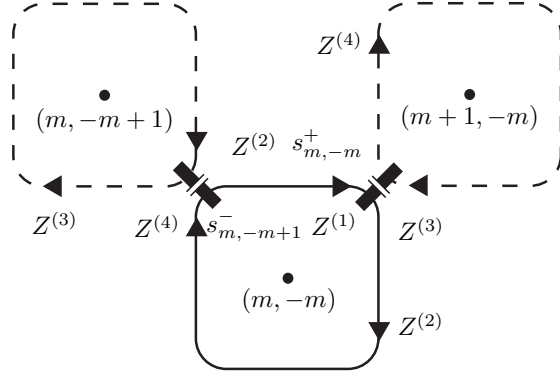


Figure 7.13. Edge with orientation c .

Next, we consider edge c , which results from the removal of all sites (m, n) with $m > -n$. (See Fig. 7.13.) In this case, $s_{m, -m+1}^-$ must be modified to prevent $Z_{m, -m}^{(4)}$ from scattering into $Z_{m, -m+1}^{(3)}$. Furthermore, $s_{m, -m}^+$ must be modified to prevent $Z_{m, -m}^{(1)}$ from scattering into $Z_{m+1, -m}^{(4)}$. For $n = -m + 1$ we replace Eq. (7.43) by

$$Z_{m, -m}^{(2)} = Z_{m, -m}^{(1)}, \quad Z_{m, -m}^{(1)} = Z_{m, -m}^{(4)}, \quad (7.49)$$

and eliminate $Z^{(2)}$ and $Z^{(4)}$ to verify that the boundary condition holds.

The condition (7.49) modifies three of the equations (7.44):

$$Z_{m, -m}^{(1)} = \frac{1}{\sqrt{2}} \left(Z_{m-1, -m}^{(1)} - Z_{m, -m}^{(3)} \right), \quad (7.50a)$$

$$Z_{m, -m}^{(3)} = \frac{1}{2} \left(Z_{m, -m-1}^{(3)} - Z_{m-1, -m-1}^{(1)} + \sqrt{2} Z_{m, -m}^{(1)} \right), \quad (7.50b)$$

$$Z_{m, -m-1}^{(1)} = \frac{1}{2} \left(-Z_{m, -m-1}^{(3)} + Z_{m-1, -m-1}^{(1)} + \sqrt{2} Z_{m, -m}^{(1)} \right). \quad (7.50c)$$

For $m < -n - 1$ Eq. (7.44) holds without modification and Eq. (7.44b) also holds for $m = -n - 1$. The solution

$$Z_{m,n < -m}^{(1)} = \sqrt{2}Z_{m,-m}^{(1)} = \text{constant}, \quad Z_{m,n}^{(3)} = 0 \quad (7.51)$$

implies $(Z_{m,n}^{(1)}, Z_{m,n}^{(3)}) \propto (1, 0)$ for $m < -n$, which satisfies the infinite mass boundary condition (7.42) with $\alpha = 0$.

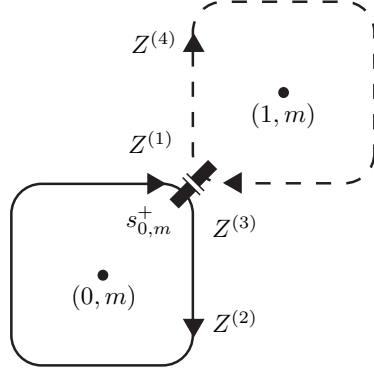


Figure 7.14. Edge with orientation d .

Edge d results from the removal of all sites (n, m) with $m > 0$. (See Fig. 7.14.) We must modify $s_{0,m}^+$ such that $Z_{0,m}^{(1)}$ does not scatter into $Z_{1,m}^{(4)}$. To do this we replace Eq. (7.43a) for sites $(0, m)$ by

$$Z_{0,m}^{(2)} = Z_{0,m}^{(1)}. \quad (7.52)$$

We again eliminate $Z^{(2)}$ and $Z^{(4)}$ to arrive at

$$Z_{0,m}^{(1)} = \frac{1}{\sqrt{2}} \left(\sqrt{2}Z_{0,m+1}^{(1)} + Z_{-1,m}^{(1)} - Z_{0,m}^{(3)} \right), \quad (7.53a)$$

$$Z_{0,m}^{(3)} = \frac{1}{\sqrt{2}} \left(\sqrt{2}Z_{0,m}^{(1)} - Z_{-1,m-1}^{(1)} + Z_{0,m-1}^{(3)} \right), \quad (7.53b)$$

while for $m < 0$ Eq. (7.44) still holds. The solution $(Z_{m,n}^{(1)}, Z_{m,n}^{(3)}) \propto (1, \sqrt{2} - 1)$ obeys the infinite mass boundary condition (7.42) with $\alpha = -\pi/4$, as required.

This completes the boundary conditions for the four orientations a , b , c , and d . The orientations a' , b' , c' , and d' are obtained by the following symmetry: The network model is left invariant by a π rotation in coordinate space (which takes \mathbf{r} to $-\mathbf{r}$) together with the application of σ_y in spinor space (which takes $Z^{(1)}$ to $-iZ^{(3)}$ and $Z^{(3)}$ to $iZ^{(1)}$).

Appendix 7.B Stable multiplication of transfer matrices

To construct the transfer matrix of a conductor one can divide it into slices, compute the transfer matrix of each slice, and multiply the individual transfer matrices. This recursive construction is numerically unstable, because products of transfer matrices contain exponentially growing eigenvalues which overwhelm the small eigenvalues relevant for transport properties. Chalker and Coddington [7] used an orthogonalisation method [20, 21] to calculate the small eigenvalues in a numerically stable way. To obtain both eigenvalues and eigenfunctions we employ an alternative method [22, 16]: Using the condition of current conservation, the product of transfer matrices can be converted into a composition of unitary matrices, involving only eigenvalues of unit absolute value.

We briefly outline how the method works for the real space transfer matrices Y of the network model, defined by Eq. (7.29). For the recursive construction it is convenient to rewrite this definition as

$$\begin{pmatrix} Z_{m+L, m-L}^{(1)} \\ Z_{m+L, m-L}^{(3)} \end{pmatrix} = \sum_{n=0}^{N-1} Y(L, L')_{m,n} \begin{pmatrix} Z_{n+L', n-L'}^{(1)} \\ Z_{n+L', n-L'}^{(3)} \end{pmatrix}. \quad (7.54)$$

The numbers L, L' are integers, so that $Y(L, L')$ is the transfer matrix from $x' = 2L'l$ to $x = 2Ll$. The composition law for transfer matrices is matrix multiplication,

$$Y(L, 0) = Y(L, L-1)Y(L-1, 0), \quad (7.55)$$

with initial condition $Y(0, 0) = \text{identity matrix}$.

The unstable matrix multiplication may be stabilized with the help of the condition $Y^{-1} = \Sigma_z Y^\dagger \Sigma_z$ of current conservation (see Sec. 7.4). Because of this condition, the matrix U constructed from Y by

$$Y = \begin{pmatrix} a & b \\ c & d \end{pmatrix} \Leftrightarrow U = \begin{pmatrix} -d^{-1}c & d^{-1} \\ a - bd^{-1}c & bd^{-1} \end{pmatrix} \quad (7.56)$$

is a unitary matrix ($U^{-1} = U^\dagger$). Matrix multiplication of Y 's induces a nonlinear composition of U 's,

$$Y_1 Y_2 \Leftrightarrow U_1 \otimes U_2, \quad (7.57)$$

defined by

$$\begin{pmatrix} a_1 & b_1 \\ c_1 & d_1 \end{pmatrix} \otimes \begin{pmatrix} a_2 & b_2 \\ c_2 & d_2 \end{pmatrix} = \begin{pmatrix} a_3 & b_3 \\ c_3 & d_3 \end{pmatrix}, \quad (7.58)$$

$$a_3 = a_1 + b_1(1 - a_2 d_1)^{-1} a_2 c_1, \quad (7.59a)$$

$$b_3 = b_1(1 - a_2 d_1)^{-1} b_2, \quad (7.59b)$$

$$c_3 = c_2(1 - d_1 a_2)^{-1} c_1, \quad (7.59c)$$

$$d_3 = d_2 + c_2(1 - d_1 a_2)^{-1} d_1 b_2. \quad (7.59d)$$

The algorithm now works as follows: Multiply a number of transfer matrices and stop well before numerical overflow would occur. Transform this transfer matrix into a unitary matrix according to Eq. (7.56). Continue with the next sequence of transfer matrices, convert to a unitary matrix and convolute with the previous unitary matrix. At the end, we may transform back from U to Y by the inverse of relation (7.56)

$$U = \begin{pmatrix} A & B \\ C & D \end{pmatrix} \Leftrightarrow Y = \begin{pmatrix} C - DB^{-1}A & DB^{-1} \\ -B^{-1}A & B^{-1} \end{pmatrix}. \quad (7.60)$$

In practice this final transformation is unnecessary. According to Eq. (7.56) the upper-right block of U is $d^{-1} \equiv (Y^{--})^{-1}$, which is all we need to calculate the conductance using the Landauer formula (7.34).

Appendix 7.C Optimal choice of phases in the network model

In Sec. 7.5 we noted that the same long-wavelength correspondence between the Dirac equation and the network model can be obtained for different choices of the phases $\phi_{m,n}^{(k)}$. Among these choices, the choice (7.37) avoids corrections of order $\partial_r V l$ to the Dirac equation. Here we show why.

For $\mu = \mathbf{A} = 0$ Eq. (7.25) reduces to

$$\beta_{m,n} = 0, \quad (7.61a)$$

$$\phi_{m,n}^{(1)} = \phi_{m,n}^{(3)} = (1 - \alpha)\varepsilon_{m,n}, \quad (7.61b)$$

$$\phi_{m,n}^{(2)} = \phi_{m,n}^{(4)} = \alpha\varepsilon_{m,n}, \quad (7.61c)$$

where we have defined the dimensionless quantity

$$\varepsilon_{m,n} \equiv [E - V(\mathbf{r}_{m,n})]l/\hbar v. \quad (7.62)$$

The parameter α can be chosen arbitrarily. We wish to show that the choice $\alpha = 0$ is optimal. We substitute Eq. (7.23a) into Eq. (7.23b) of Sec. 7.3, with this parametrization, and obtain

$$Z_{m,n}^{(1)} = \frac{e^{i\varepsilon_{m,n}}}{2} \left[e^{-i\alpha(\varepsilon_{m,n+1} - \varepsilon_{m,n})} (Z_{m,n+1}^{(1)} + Z_{m+1,n+1}^{(3)}) + Z_{m-1,n}^{(1)} - Z_{m,n}^{(3)} \right], \quad (7.63a)$$

$$Z_{m,n}^{(3)} = \frac{e^{i\varepsilon_{m,n}}}{2} \left[Z_{m,n}^{(1)} + Z_{m+1,n}^{(3)} - e^{-i\alpha(\varepsilon_{m,n-1} - \varepsilon_{m,n})} (Z_{m-1,n-1}^{(1)} - Z_{m,n-1}^{(3)}) \right]. \quad (7.63b)$$

Now we expand in $\varepsilon_{m,n}$, keeping terms to first order, and take $Z^{(1)}$ and $Z^{(3)}$ to be functions defined for all \mathbf{r} and smooth on the scale of the lattice. From Eq. (7.63) we then obtain

$$0 = [E + \sigma_z p_x + \sigma_x p_y - V(\mathbf{r})] \begin{pmatrix} Z^{(1)} \\ Z^{(3)} \end{pmatrix} - \frac{\alpha}{2} \begin{pmatrix} V(\mathbf{r} + \mathbf{a}_2) - V(\mathbf{r}) & V(\mathbf{r} + \mathbf{a}_2) - V(\mathbf{r}) \\ V(\mathbf{r}) - V(\mathbf{r} - \mathbf{a}_2) & V(\mathbf{r} - \mathbf{a}_2) - V(\mathbf{r}) \end{pmatrix} \begin{pmatrix} Z^{(1)} \\ Z^{(3)} \end{pmatrix}. \quad (7.64)$$

After transforming to $\Psi = \mathcal{G}(Z^{(1)}, Z^{(3)})^T$, with \mathcal{G} as in Eq. (7.26), the first term on the r.h.s. of Eq. (7.64) becomes the desired Dirac equation. If we choose $\alpha \neq 0$ then the potential V has to be smooth on the scale of the lattice, for the second term to be negligible in comparison with the first. We conclude that $\alpha = 0$ is the optimal choice.

Bibliography

- [1] A. H. Castro Neto, F. Guinea, N. M. R. Peres, K. S. Novoselov and A. K. Geim, arXiv:0709.1163.
- [2] J. W. McClure, Phys. Rev. **104**, 666 (1956).
- [3] M. P. A. Fisher and E. Fradkin, Nucl. Phys. B **251**, 457 (1985).
- [4] A. W. W. Ludwig, M. P. A. Fisher, R. Shankar and G. Grinstein, Phys. Rev. B **50**, 7526 (1994).
- [5] D.-H. Lee, Phys. Rev. B **50**, 10788 (1994).
- [6] K. Ziegler, Europhys. Lett. **31**, 549 (1995).
- [7] J. T. Chalker and P. D. Coddington, J. Phys. C **21**, 2665 (1988).
- [8] C.-M. Ho and J. T. Chalker, Phys. Rev. B **54**, 8708 (1996).
- [9] B. Kramer, T. Ohtsuki and S. Kettemann, Phys. Rep. **417**, 211 (2005).
- [10] A. K. Geim and K. S. Novoselov, Nature Mat. **6**, 183 (2007).
- [11] K. Hirose, T. Ohtsuki and K. Slevin, Physica E **40**, 1677 (2008).
- [12] J. Tworzydło, B. Trauzettel, M. Titov, A. Rycerz and C. W. J. Beenakker, Phys. Rev. Lett **96**, 246802 (2006).
- [13] H. Schomerus, Phys. Rev. B **76**, 045433 (2007).
- [14] Ya. M. Blanter and I. Martin, Phys. Rev. B **76**, 155433 (2007).
- [15] A. Rycerz, J. Tworzydło and C. W. J. Beenakker, Europhys. Lett. **79**, 57003 (2007).

- [16] J. H. Bardarson, J. Tworzydło, P. W. Brouwer and C. W. J. Beenakker, *Phys. Rev. Lett.* **99** 106801 (2007).
- [17] K. Nomura, M. Koshino and S. Ryu, *Phys. Rev. Lett.* **99**, 146806 (2007).
- [18] P. San-Jose, E. Prada and D. Golubev, *Phys. Rev. B* **76**, 195445 (2007).
- [19] M. V. Berry and R. J. Mondragon, *Proc. R. Soc. Lond. A* **412**, 53 (1987).
- [20] J. L. Pichard and G. Sarma, *J. Phys. C* **14**, L127 (1981).
- [21] A. MacKinnon and B. Kramer, *Z. Phys. B* **53**, 1 (1983).
- [22] H. Tamura and T. Ando, *Phys. Rev. B* **44**, 1792 (1991).
- [23] J. Martin, N. Akerman, G. Ulbricht, T. Lohmann, K. von Klitzing and A. Yacoby, *Nature Physics* **4**, 144 (2008).

Samenvatting

Verstrooiingstheorie is een breed veld met een lange geschiedenis. Nog voor de geboorte van quantummechanica hebben natuurkundigen reeds de verstrooiing van klassieke golven en van klassieke deeltjes bestudeerd. Een groot deel van onze huidige kennis van de bouwstenen van materie is verworven met verstrooiingsexperimenten. Eén van de eerste was het bekogelen met heliumionen van een goudfilm door Rutherford in 1909, waaruit hij het bestaan van positief geladen atoomkernen kon afleiden. Verstrooiingsverschijnselen zien we ook in het dagelijks leven: vleermuizen, dolfinnen en piloten zouden blind zijn zonder radar. Tegenwoordig worden verstrooiingsexperimenten dagelijks uitgevoerd, in uiteenlopende opstellingen als de reusachtige versneller bij CERN (typische energieschaal $\sim 10^9$ eV) en in nanometer-brede geleiders (typische energieschaal $\sim 10^{-3}$ eV).

De overeenkomst tussen al deze experimenten is een bron die deeltjes of golven uitzendt. De deeltjes of golven bewegen dan onverstoord door totdat ze in contact komen met een obstructie, die de *verstrooier* wordt genoemd. De verstrooier beïnvloedt de deeltjes of golven. Hun bewegingsrichting of hun energie kan bijvoorbeeld veranderd worden. Ver van de verstrooier worden de deeltjes of golven weer opgevangen. Door de eigenschappen van de deeltjes of golven voor en na de verstrooiing te vergelijken, kunnen we informatie verkrijgen over de verstrooier. Andersom, wanneer de aard van de verstrooier bekend is, kunnen we de verandering in de eigenschappen van de deeltjes of golven voorspellen.

In dit proefschrift wordt de verstrooiing van electronen in geleiders onderzocht. De geleiders zijn klein: typische groottes variëren van micrometers (honderdmaal dunner dan een menselijke haar) tot nanometers (honderdduizend maal dunner dan een haar). De geleider treedt op als verbinding tussen electronenreservoirs. Deze verbinding laat transport van electronen tussen de reservoirs toe, maar verstrooit ook de electronen die tussen de twee reservoirs proberen te bewegen. De weerstand van de ge-

leider duidt aan hoe moeilijk het voor de electronen is van het ene naar het andere reservoir te bewegen. De weerstand wordt gedefinieerd door de verhouding tussen het potentiaalverschil tussen de reservoirs en de (electronen)stroom door de geleider. Wanneer de geleider zo klein is dat electronen geen energie verliezen tijdens de periode dat ze zich in de geleider bevinden, wordt de weerstand bepaald door de elastische verstrooiingseigenschappen van de geleider. (Elastisch verwijst hier naar het behoud van energie.) Hoe groter de kans dat electronen in de geleider teruggekaatst worden naar het reservoir waar ze vandaan kwamen, hoe groter de weerstand. Dit nu vormt de basis voor Landauer–Büttiker verstrooiingstheorie van electrongeleiding, als ook van dit proefschrift.

De natuurwetten die de verstrooiing van electronen in bovengenoemde systemen bepalen is reeds tachtig jaar bekend. Het is dus een gegronde vraag waarom er vandaag de dag een proefschrift over dit onderwerp verschijnt. Het antwoord hierop ligt in de doorbraken die de laatste twee decennia plaatsgevonden hebben in de experimentele nanowetenschap. Dikwijls zijn de verschijnselen die door de quantummechanica voorspeld worden zo subtiel, dat ze gemakkelijk door ongewenste wisselwerking met de omgeving teniet gedaan worden, en die verder moeilijk waar te nemen zijn. Tegenwoordig zijn experimentele natuurkundigen echter in staat om geleiders en halfgeleiders op nanometerschaal te beheersen, en om electronen beter en beter van hun omgeving af te schermen. Nieuwe materialen en methodes worden regelmatig ontdekt. Zodoende worden gebieden die voorheen uitsluitend het domein van theoretici waren, voor experimentatoren ontsloten.

Twee voorbeelden uit dit proefschrift kunnen genoemd worden:

1. Het systeem dat in Hoofdstuk 4 onderzocht wordt, is gebaseerd op een model dat reeds in de zestiger jaren van de vorige eeuw theoretisch bestudeerd is. In die tijd waren voorstelbare realisaties van dit model echter beperkt tot halfgeleiders van macroscopische afmetingen. Dit gegeven heeft er ongetwijfeld aan bijgedragen dat de aanvankelijke onderzoeken beperkt bleven tot systemen in evenwicht. De studie van niet-evenwichts verschijnselen zou kunstmatig en zonder toepassing geweest zijn. In dit proefschrift wordt een realisatie in een kleine, één-dimensionale geleider onderzocht. Dit geeft ons een mogelijkheid die in 1960 nog ontbrak, namelijk om niet-evenwichts verschijnselen te bekijken die meetbaar zijn met de huidige technologie.

2. In Hoofdstukken 5, 6 en 7 beschouwen we de verstrooiing van Dirac-fermionen. Deze deeltjes zijn massaloos en onderhevig aan het Pauli uitsluitingsbeginsel. Ze komen voor in relativistische quantumtheorieën en leveren bijvoorbeeld in goede benadering een beschrijving van de dynamica van neutrino's. De opstellingen die wij bekijken (bijvoorbeeld een quantum-Hall systeem) hebben binnen die context echter geen enkele kans op experimentele realisatie. Wederom is het de experimentele nanowetenschap die de theoretische onderzoeken in dit proefschrift relevant maakt. Ditmaal is het te danken aan experimenten aan een vorm van koolstof, grafeen genaamd, die in 2004 ontdekt is, en waarin Dirac-fermionen voorkomen.

Hier volgt een opsomming van de inhoud van de verschillende hoofdstukken in dit proefschrift. Na een inleidend hoofdstuk, en Hoofdstuk 2 waarin het nodige gereedschap ontwikkeld wordt, komen niet-elastische processen, waar electronen tijdens de geleiding energie uitwisselen met hun omgeving, aan de orde. In Hoofdstuk 3 onderzoeken we welke metingen een fotondetector zal doen in de nabijheid van een kleine geleider waarover een potentiaalverschil V is aangelegd. Als gevolg van stroomfluctuaties in de geleider zijn er ook fluctuaties in de electromagnetische velden in de omgeving van de geleider. De detector neemt deze fluctuaties waar als discrete quanta genaamd fotonen. We laten zien dat er tot op laagste orde twee processen (één-foton en twee-foton) zijn die bijdragen aan detector-metingen in het energie-interval tussen $1 eV$ en $2 eV$ (waar e de lading van het electron is), en berekenen de grootte van deze bijdrages.

In Hoofdstuk 4 onderzoeken we wat er gebeurt wanneer electronen en hun verstrooier energie kunnen uitwisselen en de uitwisseling de eigenschappen van de verstrooier veranderen. Er wordt weer een potentiaalverschil V over de geleiders aangelegd. We bestuderen de stroom die door de geleider vloeit, en vinden dat er een regime met sterke wisselwerking is, van welk het gedrag noemenswaardig verschilt van het zwakke-wisselwerkingregime. In het laatste is de waarschijnlijkheid dat de toestand van de verstrooier verandert groter naar mate de energie voor de overgang kleiner is. In het sterke-wisselwerkingregime zijn er minstens twee resonante energieën waarbij de verstrooier gemakkelijk van toestand verandert. Het verschil tussen die energieën bedraagt eV .

In Hoofdstuk 5 onderzoeken we de geleiding van electronen door een dubbellaag grafeen, en vergelijken de resultaten met die voor een enkele laag grafeen.

In Hoofdstuk 6 onderzoek we de randtransporteigenschappen van een strook grafeen in gekruiste elektrische en magnetische velden. Het elektrisch veld wordt over de lengte van de strook aangelegd, en geconcentreerd in een klein gebied. Het magneetveld is constant en loodrecht op het grafeenoppervlak. In een parametergebied waar een conventioneel tweedimensionaal electronensysteem geen stroom parallel aan het elektrisch veld kan geleiden en waar het geleidingsvermogen in grafeen in de richting loodrecht op het elektrisch veld $G_0 = 2e^2/h$ bedraagt, vinden wij een geleidingsvermogen van $G_0(1 - \cos \Phi)/2$ parallel aan het elektrisch veld. De fase Φ wordt bepaald door het aantal eenheidscellen van het atoomrooster over de breedte van de strook. Wanneer dit aantal een veelvoud van drie is dan geldt $\Phi = \pi$, anders geldt $|\Phi| = \pi/3$.

In Hoofdstuk 7 bespreken we het probleem van numerieke berekening van de verstrooiingsmatrix van een grafeenvel gekoppeld aan reservoirs. We kijken specifiek naar het geval waar de geleidingselectronen in de reservoirs een veel kortere golflengte hebben dan in het grafeen. Onze numerieke methode maakt gebruik van een equivalentie tussen de Diracvergelijking die electronen in grafeen beschrijft, en een netwerkmodel uit de quantum-Hall literatuur. We gebruiken de methode om een electrostatisch gedefinieerd puntcontact in grafeen te bestuderen. (Een electrostatisch puntcontact is een nauwe ‘poort’ van lage potentiële energie, tussen twee ‘heuvels’ van hoge potentiële energie). We vinden plateaus in het geleidingsvermogen als functie van de breedte van de contactopening. In een andere onderzoek bevestigen we dat het geleidingsvermogen van een grafeenvel toeneemt in de aanwezigheid van wanorde die langzaam varieert op schaal van het atoomrooster.

Samevatting

Verstrooiingsteorie is 'n breë veld met 'n lang geskiedenis. Nog voor die geboorte van kwantummekanika het fisici reeds die verstrooiing van klassieke golwe en van klassieke deeltjies soos kanonkoeëls bestudeer. 'n Groot deel van ons huidige kennis van die boustene van materie is verwerf in verstrooiingseksperimente. Een van die eerste hiervan is Rutherford se bombardering van 'n goudfilm met helium ione in 1909 waaruit die bestaan van die positief-gelaaide atoomkern afgelei is. Verstrooiingseksperimente is ook van praktiese nut in die alledaagse lewe. Vlermuise, dolfyne en vlieëniers sou blind gewees het sonder radar. Vandag word verstrooiingseksperimente steeds daagliks uitgevoer en dan in sulke uiteenlopende omgewings soos die reusagtige versnellersentrum by CERN (tipiese energieë $\sim 10^9$ eV) en in nanometer breë geleiers (tipiese energieë $\sim 10^{-3}$ eV).

Wat hierdie eksperimente in gemeen het is dat 'n bron deeltjies of golwe uitstraal. Die deeltjies of golwe beweeg dan ongehinderd voort totdat hulle in kontak kom met 'n obstruksie waarna verwys word as die verstrooier. Die verstrooier beïnvloed die deeltjies of golwe. Hul rigting van beweging of hul energie kan byvoorbeeld verander. Ver van die verstrooier word die verstrooide deeltjies of golwe opgevang. Deur die eienskappe van die deeltjies of golwe voor en na verstrooiing te vergelyk, bekom ons inligting oor die verstrooier. Omgekeerd, as die aard van die verstrooier bekend is, kan ons die verandering in die eienskappe van die deeltjies of golwe voorspel.

In hierdie tesis word die verstrooiing van elektrone in geleiers ondersoek. Die geleiers is klein. Tipiese groottes wissel van mikrometers ('n honderd maal dunner as 'n menslike haar) tot nanometers ('n honderdduisend maal dunner as 'n menslike haar). Die geleier tree op as 'n verbinding tussen elektronreservoirs. Die verbinding laat transport van elektrone tussen die reservoirs toe, maar verstrooi ook elektrone wat tussen die reservoirs probeer beweeg. Die geleier se weerstand dui aan hoe moeilik dit vir elektrone is om deur die geleier te beweeg. Dit word gedefinieer as die ver-

houding van die potensiaalverskil tussen die reservoirs tot die stroom deur die geleier. As die geleier klein genoeg is dat elektrone nie energie verloor terwyl hulle binne die geleier is nie, word die weerstand bepaal deur die geleier se elastiese verstrooiingseienskappe. (Elasties verwys hier na die behoud van energie.) Hoe groter die kans dat elektrone binne die geleier teruggereflekteer word na die reservoir waaruit hulle gekom het, hoe groter is die weerstand. Hierdie insig vorm die basis van die Landauer-Büttiker verstrooiingsteorie van elektronegeleiding as ook van hierdie tesis.

Die natuurwette wat die verstrooiing van elektrone in bogenoemde sisteme bepaal is reeds vir tagtig jaar bekend. Dit is dus redelik om te vra hoekom daar vandag juis 'n tesis oor hierdie onderwerp verskyn. Die antwoord is te vind in die deurbrake wat in die afgelope twee dekades gemaak is in die veld van eksperimentele nano-wetenskap. Dikwels is die verskynsels wat deur kwantummeganika voorspel word so delikaat dat hulle maklik deur ongewenste wisselwerkings met die omgewing vernietig word en verder moeilik is om te meet. Huidiglik is eksperimentele fisici egter in staat om geleiers en halfgeleiers op die nanometer skaal te beheer en elektrone beter en beter van hul omgewing te beskerm. Nuwe materiale en metodes word gereeld ontdek. Sodoende word gebiede wat voorheen die uitsluitlike domein van teoretici was vir eksperimentaliste ontsluit.

Twee voorbeelde uit hierdie tesis kan genoem word.

1. Die sisteem wat in Hoofstuk 4 ondersoek word is gebaseer op 'n model wat reeds in die 1960's teoreties bestudeer is. In daardie jare was denkbare realisasies van die model egter beperk tot halfgeleiers van makroskopiese dimensies. Hierdie feit het ongetwyfeld daartoe bygedra dat die aanvanklike studies beperk was tot ekwilibrium sisteme. Die studie van nie-ekwilibrium verskynsels sou kunsmatig en sonder toepassing gewees het. In hierdie tesis word 'n realisasie in 'n klein een-dimensionele geleier ondersoek. Dit gee ons 'n geleentheid wat in die 1960's ontbreek het, naamlik om nie-ekwilibrium verskynsels te ondersoek wat meetbaar is met huidige tegnologie.
2. In Hoofstukke 5, 6 en 7 beskou ons die verstrooiing van Dirac fermione. Hierdie deeltjies is massaloos en gehoorsaam Fermi se uitsluitingsbeginsel. Hulle kom voor in relativistiese kwantumteorieë en verskaf byvoorbeeld tot 'n goeie benadering 'n beskrywing van die dinamika van neutrino's. Die opstellings wat ons ondersoek (byvoorbeeld 'n kwantum Hall sisteem) is egter binne hierdie konteks

sonder enige kans op eksperimentele realisasie. Weereens is dit eksperimentele nano-wetenskaplikes wat die teoretiese studies in hierdie tesis relevant maak. Hierdie keer is dit te danke aan eksperimente op 'n vorm van koolstof genaamd grafeen wat in 2004 ontdek is, en waarin Dirac fermione voorkom.

Hier volg 'n kort opsomming van die inhoud van die onderskeie hoofstukke van die tesis. Na 'n inleidende hoofstuk en Hoofstuk 2 waarin die nodige gereedskap ontwikkel word, kom nie-elastiese prosesse, waar elektrone gedurende geleiding energie uitruil met hul omgewing, aan die beurt. In Hoofstuk 3 ondersoek ons die metings wat 'n fotondetektor sal maak in die nabyheid van 'n klein geleier waaroor 'n potensiaalverskil V aangelê is. As gevolg van stroomfluktuasies in die geleier is daar fluktuasies in die elektromagnetiese velde in die omgewing van die geleier. Die detektor gewaar hierdie fluktuasies as diskrete kwanta, genaamd fotone. Ons wys dat daar in leidende orde twee prosesse (een-foton en twee-foton) is wat bydra tot detektormetings in die energie-interval vanaf eV tot $2eV$ (waar e die lading van 'n elektron is), en bereken die groottes van beide bydra's.

In Hoofstuk 4 ondersoek ons wat gebeur as elektrone en hul verstrooier energie kan uitruil en hierdie uitruiling die eienskappe van die verstrooier verander. Daar word 'n potensiaalverskil V oor die geleier aangelê. Ons bestudeer die stroom wat deur die geleier vloei en vind dat daar 'n sterk-wisselwerkingsregime is waar die sisteem se gedrag noemenswaardig verskil van die swak-wisselwerkingsregime. In laasgenoemde is die waarskynlikheid dat die verstrooier se toestand verander groter hoe kleiner die nodige energie vir die oorgang. Verder is geen verandering in die verstrooier se toestand moontlik as die benodigde energie groter is as eV nie. In die sterk-wisselwerkingsregime is daar minstens twee resonante energieë waarby die verstrooier maklik van toestand verander. Die verskil tussen die twee energieë is eV .

In Hoofstuk 5 ondersoek ons die geleiding van elektrone deur 'n dubbellaag grafeen en vergelyk met die resultate van 'n studie van 'n enkele grafeenlaag.

In Hoofstuk 6 ondersoek ons die randtransport eienskappe van 'n grafeenstrook in gekruisde elektriese en magneetvelde. Die elektriese veld word oor die lengte van die strook aangelê en gekonsentreer in 'n kort interval. Die magneetveld is konstant en loodreg op die grafeenvlak. In 'n parametergebied waar 'n konvensionele tweedimensionele elektronsisteem geen stroom parallel aan die elektriese veld kan gelei nie en waar die geleidings-

vermoë in grafeen in die rigting loodreg op die elektriese veld $G_0 = 2e^2/h$ bedra, vind ons 'n geleidingsvermoë van $G_0(1 - \cos \Phi)/2$ parallel aan die elektriese veld. Die fase Φ word bepaal deur die aantal eenheidselle van die atoomrooster oor die breedte van die strook. As hierdie aantal 'n veelvoud van drie is dan geld $\Phi = \pi$ anders geld $|\Phi| = \pi/3$.

In Hoofstuk 7 spreek ons die probleem aan van hoe om die verstrooiingsmatriks numeries te bereken van 'n grafeen vel gekoppel aan reservoirs. Ons kyk spesifiek na die geval waar die geleidingsselektrode in die reservoirs 'n veel korter golflengte het as binne die grafeen vel. Ons numeriese metode maak gebruik van 'n ekwivalensie tussen die Dirac vergelyking wat elektrone in grafeen beskryf en 'n netwerkmodel uit die kwantum-Hall literatuur. Ons gebruik die metode om 'n elektrostaties gedefinieerde puntkontak in grafeen te bestudeer. ('n Elektrostatiese puntkontak is 'n nou poort van lae potensieële energie, tussen twee heuwels van hoë potensieële energie.) Ons vind plato's in die geleidingsvermoë as 'n funksie van die kontakopening se wydte. In 'n aparte studie bevestig ons dat die geleidingsvermoë van 'n grafeen vel toeneem in die teenwoordigheid van wanorde wat stadig varieer op die skaal van die atoomrooster.

List of publications

- *A non-unitary mapping from Cooper pairs to bosons*, I. Snyman and H. B. Geyer, Czech. J. Phys. **54**, 1133 (2004).
- *Quasi-hermiticity and the role of a metric in some boson Hamiltonians*, H. B. Geyer, F. G. Scholtz and I. Snyman, Czech. J. Phys. **54**, 1069 (2004).
- *The Richardson Hamiltonian in the strong coupling limit: new results from an application of the non-unitary Dyson mapping*, H. B. Geyer and I. Snyman, Czech. J. Phys. **55**, 1091 (2005).
- *Quantum tunneling detection of two-photon and two-electron processes*, J. Tobiska, J. Danon, I. Snyman and Yu. V. Nazarov, Phys. Rev. Lett. **96**, 096801 (2006) [Chapter 3].
- *Strong-coupling limit of the Richardson Hamiltonian analyzed using the Dyson mapping*, I. Snyman and H. B. Geyer, Phys. Rev. B **73**, 144516 (2006).
- *Ballistic transmission through a graphene bilayer*, I. Snyman and C. W. J. Beenakker, Phys. Rev. B **75**, 045322 (2007) [Chapter 5].
- *Valley-isospin dependence of the quantum Hall effect in a graphene p - n junction*, J. Tworzydło, I. Snyman, A. R. Akhmerov and C. W. J. Beenakker, Phys. Rev. B **76**, 035411 (2007) [Chapter 6].
- *Polarization of a charge qubit strongly coupled to a voltage-driven quantum point contact*, I. Snyman and Yu. V. Nazarov, Phys. Rev. Lett. **99**, 096802 (2007) [Chapter 4].
- *Advancing science in Africa*, J. van den Brink and I. Snyman. Nature Materials **6**, 792 (2007).

- *The Keldysh action of a general time-dependent scatterer*, I. Snyman and Yu. V. Nazarov, Phys. Rev. B **77**, 165118 (2008) [Chapter 2].
- *Calculation of the conductance of a graphene sheet using the Chalker-Coddington network model*, I. Snyman, J. Tworzydło and C. W. J. Beenakker, Phys. Rev. B **78**, (2008) [Chapter 7].

Curriculum vitæ

I was born on the 23rd of July 1980 in Johannesburg, South Africa. I received my primary and secondary school education in the city of my birth. In 1998 I graduated from Hoërskool Florida. In 1999 I enrolled at the Rand Afrikaans University in Johannesburg, for a Bachelors degree in Physics. With a view to becoming a theoretical physicist I moved to the Western Cape after a year, and continued my Bachelor studies from the second year onward at the University of Stellenbosch. After obtaining my Bachelors degree at the end of 2002, I started working under Prof. H. B. Geyer on my Masters thesis at the Institute of Theoretical Physics at the University of Stellenbosch. This work is entitled *Analysis and applications of the generalised Dyson mapping*. I obtained my Masters degree at the end of 2004. At the start of the next year I joined the group of Prof. C. W. J. Beenakker at the Institute Lorentz for Theoretical Physics in Leiden. I was jointly supervised by Prof. Beenakker and by Prof. Yu. V. Nazarov from Delft University of Technology. The main results of the work I did under their guidance are contained in this thesis.

During my Masters studies I was a teaching assistant for a course in quantum mechanics and one in thermodynamics. In Leiden I supervised students during exercise classes for the course Electromagnetism II from 2005 until 2007. In the course of my studies I attended several summer schools and conferences in the Czech Republic, England, Italy, the Netherlands and South Africa. I have given talks about my work at meetings in Prague, Delft and Catania.

As of the southern spring (fall in the northern hemisphere) of 2008, I will be employed as a researcher at the newly formed National Institute for Theoretical Physics in Stellenbosch, South Africa.

Stellingen

behorend bij het proefschrift

Scattering problems involving electrons, photons, and Dirac fermions

1. An electrical conductor biased by a voltage V and held at a temperature $T \ll eV/k_B$ can emit photons with energy larger than eV .

Chapter 3.

2. A many-channel point contact, biased by a voltage $V \gg k_B T/e$ and placed in the vicinity of a charge qubit, serves as thermal bath with effective temperature of the order eV/k_B for the qubit.

Chapter 4.

3. In the quantum Hall regime, the conductance of a $p - n$ junction in a graphene ribbon with armchair edges is quantized at a value that can be varied by straining the lattice.

Chapter 6.

4. The conductance of an electrostatically defined quantum point contact in graphene increases stepwise as a function of the Fermi energy.

Chapter 7.

5. A small superconducting island connected by tunnel barriers to normal metal leads has a hysteretic current-voltage characteristic.

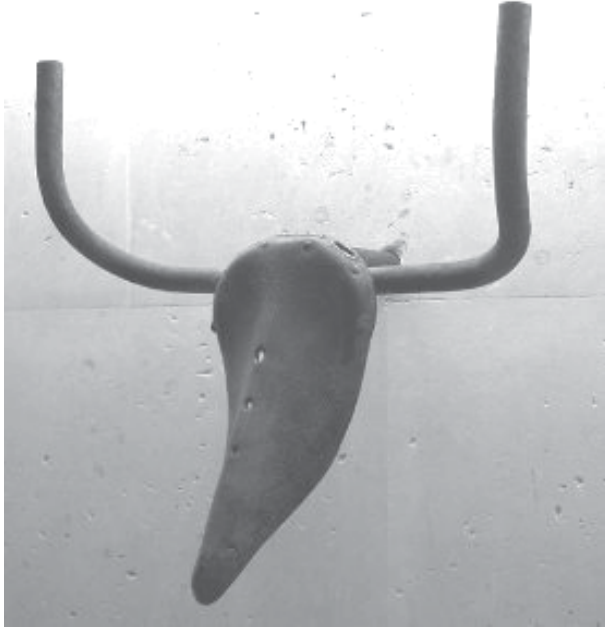
I. Snyman and Yu. V. Nazarov, *manuscript in preparation*.

6. The two states of an Andreev level qubit in a Josephson junction containing a topological insulator as weak link are eigenstates of current.

7. Coherent backscattering of light from a triangular lattice photonic crystal is suppressed near the corners of the Brillouin zone.

8. Phase averaging without mode mixing does not mimic the effect of dephasing in a quasi-one-dimensional conductor.

9. Picasso's sculpture *Tête de taureau* is an example of the whole being greater than the sum of its parts.



Tête de taureau. Pablo Picasso. 1942.
Bicycle saddle and handlebars.
(Musée Picasso, Paris)

Izak Snyman
Leiden, 23 September 2008